Dynamics of the wake behind an oscillating and rotating sphere in uniform flow

THESIS

submitted in

partial fulfillment of the requirements

for the award of the degree

of

DOCTOR OF PHILOSOPHY

in

Mechanical Engineering

on

Simon Peter
Roll No. 09610312

under the guidance of

Dr. Arnab Kumar De

Department of Mechanical Engineering,
Indian Institute of Technology Guwahati,
Guwahati - 781039, Assam, India.

October 2016

Certificate

This is to certify that Mr. Simon Peter, Roll No. 09610312, a Ph.D student in the Department of Mechanical Engineering at Indian Institute of Technology Guwahati has completed the thesis entitled "**Dynamics of the wake behind an oscillating and rotating sphere in uniform flow**" under my supervision. To the best of my knowledge the work carried out has not been submitted elsewhere for the award of a Ph.D degree. I wish him all the best for his future endeavours.

Dr. Arnab Kumar De,
Assistant Professor,
Department of Mechanical Engineering,
Indian Institute of Technology Guwahati,
Guwahati - 781039, Assam, India.

Date: 06/10/16
Place: Guwahati

Acknowledgements

First of all thanks to Jesus Christ my Lord, God, Saviour, Redeemer, Deliverer, Protector, Helper and Healer; for his mercies and grace in my life.

The work contained in this thesis is owed to my loving and caring supervisor Dr. Arnab Kumar De. I must say that at my joining I knew nothing in computational fluid dynamics, but through his perseverance, patience, enthusiasm and interest I am at least not an empty vessel at the end of the course. All the ideas and work right from the very beginning are due to him.

After my supervisor, the next person to be highly honoured is my loving wife. She was always with me in times of sadness, poverty, toughness along with happiness and joy. She used to give me tiffins, so that I can work for more time in the Laboratory. She likes to visit different places, but for my work she sacrificed all her pleasures. Also, my son has to be appreciated. He never liked my absence at home, he used to cry when I delayed coming to home.

I am highly grateful to my Doctoral Committee members: 1) Dr. Anoop K. Dass, 2) Dr. Vinayak N. Kulkarni and 3) Dr. Jiten C. Kalita for all their kindness, favours and important suggestions in completing this project.

I am highly thankful to my parents, for whatever I am today is because of their training with love. I pray to God that I may serve them in their old age and not be away from them.

I am very much thankful to Dr. Agile Mathew, Mr. Ravi Bolledu and Mr. Rohit Singh; for continually encouraging me to submit to my supervisor, and work with sincerity as unto the Lord through the BIBLE (The word of God). Though I accept

my inability to be much loyal.

I am highly indebted to the institute for providing: conducive environment, journal papers, reference materials, Library, Internet facility along with the parallel computing facility to carry out the research.

I am also thankful to my colleagues, office staff, Lab Superintendents of the Department of Mechanical Engineering; for their direct and indirect valuable helps in completing the work.

Name: Simon Peter,
Roll No.: 09610312,
Ph.D Student,
Department of Mechanical Engineering,
Indian Institute of Technology Guwahati,
Guwahati - 781039, Assam, India.

Date: 06/10/16
Place: Guwahati

Abstract

Vortex-induced vibration (VIV) is a class of flow-induced vibration (FIV), where the vortices interact with the structure and cause its oscillation. A structure can acquire motion along any of the six degrees of freedom (*dof*). If these motions are not included in design considerations they can cause structural failure. The primary objective of the current research is to reveal the wake dynamics of a simultaneously oscillating and rotating sphere in uniform incompressible flow.

Forced vibration of a structure has proved to be an easy alternative to predict the inter-play between the fluid and structure. The present work prescribes a sinusoidal motion to the sphere in the transverse direction (y) with a range of frequency ratio ($0.16 \leq f_R \leq 1.3$) at a fixed normalized amplitude ($A = 0.5$) and Reynolds number ($Re = 300$) are considered. The sphere is also allowed to rotate about the three primary axes: stream-wise (x), transverse (y) and vertical (z) and a generalized orientation with equal components which enables it to couple four degrees of freedom. This configuration considers a constant normalized angular velocity ($\alpha = 1.2$) at $f_R = 0.8$ and 1.3.

Three-dimensional parallel numerical simulations are performed in a non-inertial frame of reference by employing finite volume method on non-staggered and non uniform cartesian grid. A modified immersed boundary method (IBM) is adopted to enforce the boundary conditions on the surface of the sphere. Time evolution of the force coefficients, vorticity and wake structure are examined to reveal the underlying physics.

For the oscillating sphere negative coefficient of energy (C_E) is obtained. To

explain the sign of C_E a forcing mechanism is proposed where the fluid force (F_F) measured by C_{vortex} and the external force (F_E) measured by $C_{potential}$ compete with each other. A synchronization regime where the forcing frequency (f_e) is in agreement with the wake (f_s) oscillation is found in the range $0.45 \leq f_R \leq 1.3$. Within this range two different flow behaviours characterised by ϕ_{vortex} (phase angle between C_{vortex} and sphere motion) are identified as Modes I and II for $1.1 \leq f_R \leq 1.3$ and $0.45 \leq f_R \leq 1.05$, respectively. On the other hand, an asynchronous state is observed at $f_R = 0.16$ and 0.2. For all cases a planar-symmetry in the flow about the mid horizontal plane is observed which causes the coefficient of vertical force (C_H) to be zero. The observed modes revealed have strong correlation with the earlier reported VIV modes of a sphere.

When the oscillating sphere is allowed to rotate also, the previously observed planar-symmetry sustains only for rotation about z axis. The wake demonstrates a synchronized state for all the orientations of the rotational axis at $f_R = 1.3$. On the other hand, at $f_R = 0.8$, the synchronization is lost except for rotation about x axis. In the absence of synchronization, nature of the flow is found to be either quasi-periodic (z rotation) or chaotic (y and xyz rotations). The rotational tendency of the wake is found to be maximum and minimum for rotations about x and y, respectively. Except the rotations about x axis, a deflection in the wake is seen towards the advancing side of the sphere where the surface velocity opposes the flow.

Modifications proposed on the previously reported IBM enhances its capabilities with respect to stability and wider applicability. Larger hydrodynamic forces for an oscillating sphere compared to a stationary one implies that oscillation and rotation must be considered in predicting fluid forces on a structure, else they can have catastrophic effects. Different tendencies of the wake to rotate suggests that a sphere will first rotate about x then z and lastly about y axis. Rotations about y and z axes revealed different flow features, so both cannot be considered same as is usually done for a purely rotating sphere.

Contents

Abbreviations

ABCN:	Adams Bashforth Crank-Nicolson
BiCGSTAB:	Bi-Conjugate Gradient Stabilized
CN:	Crank-Nicolson
CV:	Control volume
SOR:	Gauss-Seidel successive over-relaxation
ILU:	Incomplete lower and upper factorization
SIP:	Strongly implicit procedure
SIP-BiCGSTAB:	SIP preconditioned Bi-Conjugate Gradient Stabilized

Symbols

x_i	i-th ($i = x, y, z$) spatial direction
t	Time
u_i	i-th component ($i = x, y, z$) of velocity
p	Pressure
D	Diameter of circular cylinder or sphere
U	Free-stream velocity
ρ	Density of fluid
ν	Kinematic viscosity of fluid
Re	Reynolds number
C_i	Coefficient of drag ($i = D$), lift ($i = L$) and vertical force ($i = H$)
$< C_i >$	Average values of the Coefficients
C_i'	Root-mean-square (rms) values of the Coefficients
St	Strouhal number
Δt	Time increment
ω_i	i-th component ($i = x, y, z$) of vorticity
Q	Wake or vortical structure

List of Figures

List of Tables

Chapter 1

Introduction

Fluid is in abundance on earth, so any engineering structure such as building, bridge, chimney, heat-exchanger tube, electric power pole, riser tube bringing oil from the seabed to the surface, offshore platform etc. has to withstand forces exerted by the fluid. Neglecting fluid forces during design considerations can be catastrophic to these structures. Interaction of fluid flow with such structures is termed as flow-induced vibrations (FIV). Blevins [1] has classified it by the nature

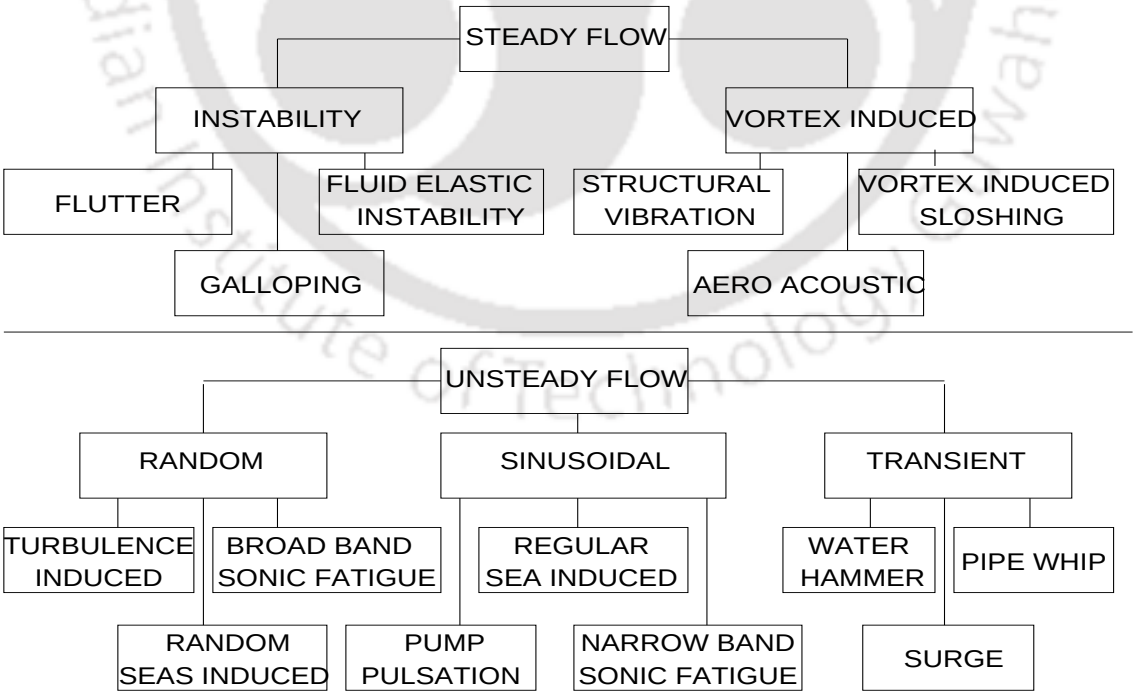

Figure 1.1: Classification of flow-induced vibrations

of the flow and structure as shown in Fig. 1.1. Most of the structures in use are

bluff (obstructing the flow) as streamlines cannot follow their surfaces or contours. Bluff structures are designed to bear loads (bridges or buildings), contain flow (nuclear reactors or riser tubes) or provide heat transfer surface (heat exchanger tubes or electronic cooling systems).

1.1 Uniform flow past bluff structures

Uniform flow past a bluff structure undergoes a sequence of transitions as the inertia of the approaching flow measured by Reynolds number (Re) increases. A fluid particle approaching a structure experiences increased pressure. At critical Reynolds number (which depends upon the shape of the structure) flow separates and wake is formed. The wake is a region behind the structure where velocity is still lower than the free stream value.

Due to the flow separation free shear layers generate in the wake. A shear layer is influenced both by the structure and the approaching flow. Variation in the speed of these shear layers causes them to roll. Consequently, a recirculation region of attached discrete swirling vortices (or eddies) in the wake is formed. At some higher Re, these vortices begin to detach (or shed) from the structure rendering an unsteady wake.

Unsteady nature of the wake exerts oscillating forces on a structure. These forces are referred as Drag (F_x), Lift (F_y) and Vertical force (F_z) along the Stream-wise (x), Transverse (y) and Vertical (z) directions, respectively. Customarily, these are non-dimensionalized to give Coefficients of forces (C_i) where subscript i stands for the directions x, y and z. Frequency of oscillation (f) is determined from the lift force, and is non-dimensionalized as Strouhal number (St).

Consider a structure having characteristic length D in uniform flow with velocity U, density and kinematic viscosity represented by ρ and ν, respectively. Respective expressions for the Reynolds number, Coefficients of forces and Strouhal

number are

$$Re = \frac{UD}{\nu}, C_i = \frac{F_i}{\frac{1}{2}\rho U^2 A_i}, St = \frac{fD}{U} \tag{1.1}$$

where A_i is the projected area in the i-th direction. Each coefficient of force has contributions coming from pressure and friction.

Flow past a bluff structure (or wake flow) is characterized by a dominant coefficient of pressure drag than the friction drag. Circular cylinder and sphere are the two most popular form of bluff objects, which exhibit almost all physical phenomena associated with bluff structures. Table 1.1 describes the main flow regimes for uniform flow past a stationary sphere.

1.2 Vortex-induced vibration

Shedding of vortices induces oscillating or fluctuating forces on the structures. If the structure is not stiff enough, it may acquire complex motion or vibration. Such acquired motion is called Vortex-induced vibration (VIV). Studies on VIV are purposed to estimate fluid forces (under operating conditions additional to weight of the structure) and motion of the structure caused by them. This estimation help design engineers in enhancing stability, reliability and durability of a structure.

In general, structures in a flow can acquire motions along any of the six degrees of freedom (*dof*). For a ship shown in Fig. 1.2 three-translational *dof* along x, y and z are referred as surging, swaying and heaving motion, respectively. On the other hand, rotation about x, y and z are referred as rolling, pitching and yawing, respectively. Practically, a structure can undergo motions along all the six *dof* at the same time, but inclusion all of them only complicates the VIV analysis. Moreover, it has been observed that motion along the transverse direction is significantly important than the rest. Therefore, most of the VIV studies consider motion along y-direction only.

According to the law of inertia, a structure resists the motion induced by the flow. Source of this resistance can be either the weight including other mechanical

Reynolds number	Flow regime	Flow form	Flow characteristic
$Re \rightarrow 0$	Creeping	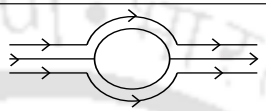	One-dimensional, Streamlines follow sphere's surface
20<Re<210	Steady axisymmetric		Two-dimensional, Flow separation and a vortex-ring attached at rear surface of the sphere
210<Re<270	Steady planar-symmetric		Three-dimensional, Two parallel counter-rotating vortices in the wake
300<Re<450	Unsteady planar-symmetric	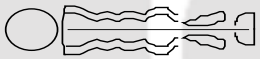	Highly organized periodic flow, Shedding of hairpin vortices
450<Re<800	Unsteady asymmetric		Slow rotation of the separation point, Orientation of shed vortices changes
800<Re<3×10^5	Subcritical		Laminar boundary layer, Turbulent wake, Small scales appear because of Kelvin-Helmholtz instability
3.7×10^5<Re<1.5×10^6	Supercritical	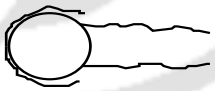	Turbulent boundary layer, Turbulent wake, Separating vortex sheets$-\Omega$ shape, Wake flow offset from stream-wise axis

Table 1.1: Different flow regimes for uniform flow past a stationary sphere

properties of the structure (stiffness) or the viscosity of the fluid (damping). There-

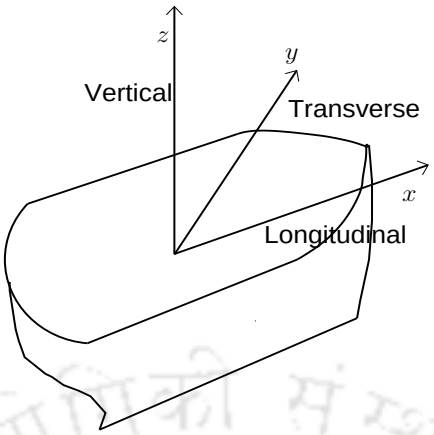

Figure 1.2: Movement of a ship

fore, the transverse motion is generally expressed as

$$m\ddot{y} + c\dot{y} + ky = F_y \tag{1.2}$$

where m is mass of the structure, c is the structural damping and k is the spring constant. Incorporation of Eq. (1.2) in VIV analysis brings new parameters additional to those given by Eq. (1.1). Table 1.2 tabulates these additional parameters where m_d, $m_A(C_A m_d)$, f_N are the mass of displaced fluid, added mass and natural frequency, respectively. Moving object induces motion in fluid, so energy is expended for both object and fluid accelerations, and accounted by added mass, a function of fluid's density. It's significant for ships, but negligible in aircrafts. Coefficient of potential flow added mass is represented by C_A and is equal to 1 and 0.5 for a circular cylinder and sphere, respectively. The transverse motion of the structure is characterised by the transverse amplitude (A_y) and frequency (f_y).

1.2.1 Vortex-induced vibration of a circular cylinder

VIV studies mainly focus on the motion of the structure or what is termed as response. After fixing the structural parameters (m^* and ζ), the flow speed characterized by U^* is varied and corresponding response characterized by A_y^* and f^* is observed. Sarpkaya [2, 3], Bearman [4], Williamson & Govardhan [5] have

Parameters	Symbol	Expression
Mass ratio	m^*	$\frac{m}{m_d}$
Damping ratio	ζ	$\frac{c}{2\sqrt{k(m+m_A)}}$
Normalized velocity/ Reduced velocity/ Velocity ratio	U^*	$\frac{U}{f_N D}$
Normalized transverse amplitude/ Transverse amplitude ratio	A_y^*	$\frac{A_y}{D}$
Transverse frequency ratio	f^*	$\frac{f_y}{f_N}$

Table 1.2: Additional non-dimensional parameters in VIV

carried out intensive reviews on VIV of a circular cylinder. In these studies m^* and ζ are combined into a single variable $(m^* + C_A)\zeta$, known as mass-damping parameter, is found to be very useful. Compilation of peak response amplitude data as a function of this mass-damping parameter is referred to as 'Griffin plot'.

Depending on the magnitude (high or low) of mass-damping parameter different types of responses have been recorded. For high mass-damping parameter, experiments conducted by Feng [6] in air at $m^* = 100$, two branches of response namely 'initial' and 'lower' were observed. On the other hand, Khalak & Williamson [7] for a low mass-damping system in water at $m^* \approx 10$ found three branches: 'initial', 'upper' and 'lower' as the normalized velocity was increased.

VIV studies involve a number of parameters associated with both the dynamics of the structure (response) and fluid (forces). Control of all the parameters puts a heavy burden on the overall analysis. In this context Blevins [8] remarked that "accurate prediction of vortex-induced vibration has proved difficult, owing to nonlinear fluid forces and feedback between the cylinder and the fluid flow".

1.2.2 Forced vibration of a circular cylinder

In simple words, VIV is an inter-play between the flow and the structure i.e., the flow influences the structure and in reaction flow is modified. An alternative route to understand this inter-play is observing the wake after giving the structure a prescribed sinusoidal motion. This procedure is called forced vibration in contrast to free vibration (VIV). Forced vibration studies simplify the task as motion of the structure is predefined (known) and only the flow behaviour needs to be monitored.

One of the earliest study on a mechanically oscillating circular cylinder in uniform flow was carried out by Den Hartog [9]. Flow patterns in the wake was photographed at the start of an oscillation cycle and repeated at the end of the cycle. This repetition indicates same periodicity of the cylinder motion and the flow. When the period or frequency of the flow synchronized with that of cylinder oscillation, the state of the wake was termed [9] as 'lock-in'.

Within the synchronization regime, Bishop & Hassan [10] found amplification in the hydrodynamic forces (lift and drag), and a jump in the phase between the lift and the cylinder motion. Later, this jump was associated with a change in timing of vortex shedding by Zdravkovich [11], and different wake modes by Williamson & Roshko [12]. The two wake modes were designated [12] as '2S' and '2P' meaning two single vortices and two pair of vortices, respectively formed in an oscillation cycle.

1.2.3 Similarity between free and forced vibration

Number of forced vibration studies exceed that of VIV for a circular cylinder. First studies on forced and free vibrations of a circular cylinder were reported by Den Hartog [9] in 1934 and Meier-Windhorst [13] in 1939, respectively. Thereafter, many studies have been undertaken to establish the similarity between these two routes. Notably Morse & Williamson [14–16] have established that VIV of a circu-

lar cylinder can be predicted using the forced vibration studies, if the experimental conditions are exactly matched.

The wake modes revealed for the forced vibration of a circular cylinder by Williamson & Roshko [12] in 1988 were later confirmed by the free vibration study of Govardhan & Williamson [17] in 2000. Phenomena such as harmonic oscillation of the structure, synchronization, change in timing of vortex shedding, amplification of the hydrodynamic forces and jumps in the phases have been found common to both free and forced vibrations. Observation of same phenomena and modes suggest a strong correlation between these two modes of study for a circular cylinder.

1.3 Numerical simulations

Numerical simulations of flow around three-dimensional geometries is quite challenging, especially at high Re where small scale structures appear due to flow instabilities. Enormous increase in computer power and significant development in numerical methods have led to a number of numerical studies on the simpler three-dimensional case of uniform flow past a stationary sphere since 1999. It is worth noting that most of the numerical studies on a stationary [18–22], vibrating [23–25] and rotating [26–33] sphere have been performed at a lower Re owing to limitations in computing power and grid resolution.

Conventionally, complex geometries are handled using body-fitted structured or unstructured grids. Structured grid with finite difference discretization requires coordinate transformation leading to computation of extra geometric coefficients. Unstructured grid has an advantage of more controlled local mesh refinement than the structured grid. Grid generation, data structure and formulations are highly involved in these conventional routes. Difficulties of handling spatial terms in the body-conformal grids and simplicity of the cartesian grids have motivated to adopt non-body conformal cartesian grids for simulating complex flows.

1.3.1 Immersed Boundary Method

Immersed Boundary Method (IBM) refers to all the techniques which simulate flows around complex geometries on non-body conformal grids. These techniques are named as IBM as primarily they were devised for completely immersed boundaries that interact with the surrounding fluid. Peskin [34] was the first to propose IBM and simulate flow through the natural mitral heart valve on uniform cartesian grid. There are numerous advantages of IBM, such as ease of grid generation, incorporating body motions and ease of implementing fast and stable iterative linear solvers. However, the most difficult task for such a method is to enforce boundary conditions on a non-body conformal grid.

Originally the fluid and the immersed boundary were treated in Eulerian and Lagrangian forms [34], respectively. A forcing function was incorporated in the Navier-Stokes equation to link the immersed boundary and the flow. Numerically this treatment is suitable for flexible elastic boundaries, but its implementation on rigid bodies can lead to stiffness issues. Goldstein *et al.* [35] proposed a feedback forcing approach that required two ad-hoc user specified parameters for imposing boundary conditions on rigid bodies. Both these approaches spread the forcing around the immersed boundary which is difficult to justify at high Re flows.

Mohd-Yosuf [36] proposed a discrete time forcing approach that does not require spreading of the forcing. Moreover, for unsteady flows this approach does not severely limit the time step as in the previous approaches. Kim *et al.* [37] demonstrated that inclusion of mass source/sink in this approach alleviates non-physical solutions.

A ghost-cell immersed boundary method (GCIBM) was proposed by Majumdar *et al.* [38] for which a typical computational layout is shown in Fig. 1.3. Computational cells are tagged as fluid (○) or solid (●) if they are located outside or inside the complex body, respectively. Solid cells having at least one fluid cell in their immediate neighbourhood are tagged as ghost-cells (▲). To each ghost-cell a body point (**x**) is identified on the body which usually lies on the normal

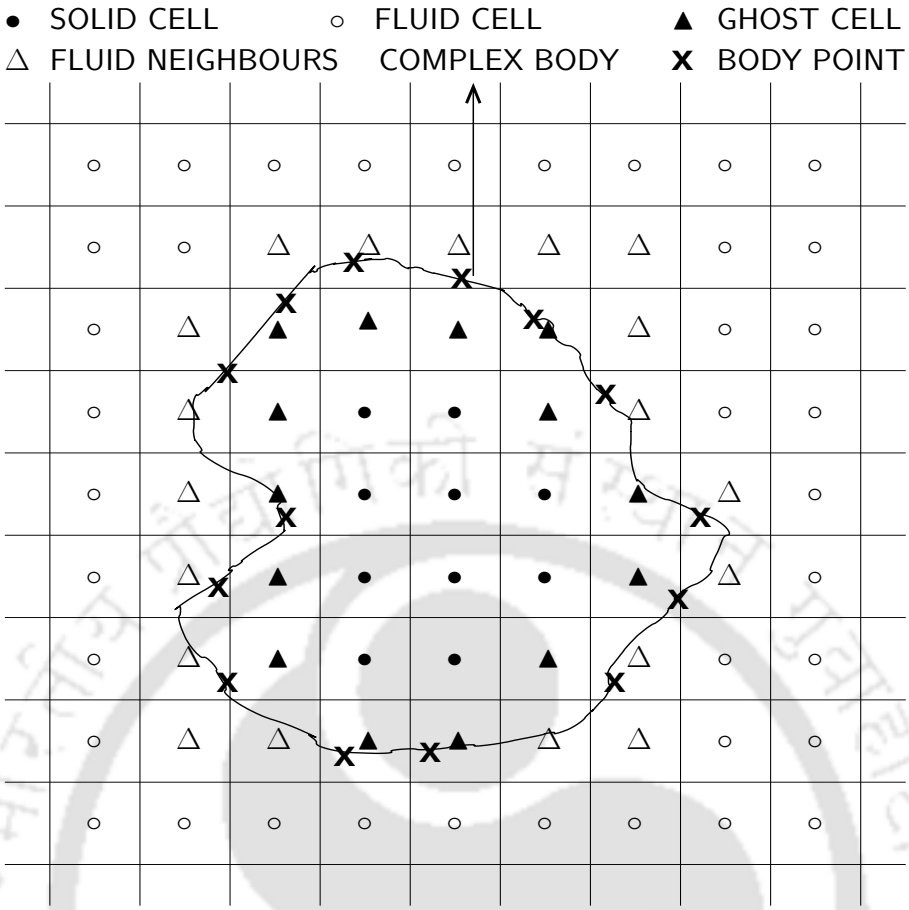

Figure 1.3: Classification of cells in GCIBM

to the complex object. All the body points taken together resemble the complex body on a non-conformal grid. The flow equations are satisfied only at the fluid cells while the solid cells are kept outside the scope of computations. To impose boundary conditions, the computational stencil near the complex body is modified by interpolating the flow variables at the ghost-cells using the known values of fluid neighbours (△) and body point. This interpolation is at heart of GCIBM and the procedure is called reconstruction. The word ghost in GCIBM signifies that though there is no flow inside the body still the flow variables are interpolated at inside cells.

Various polynomial interpolation procedures have been proposed [38], but these procedures are not always effective as matrix inversion is required. The matrix tends to be singular as: 1) higher degree polynomials are chosen, 2) mesh is refined and 3) body point approaches a neighbouring fluid cell. To remove this

singularity an image point is identified [38] in the fluid domain located as mirror of the ghost-cell centroid. The flow variables are interpolated at this image point while variables at ghost-cell are evaluated assuming a linear variation from the image point.

Iaccarino & Verzicco [39] suggested the inverse distance weighting (IDW) to avoid the matrix inversion associated with the polynomial interpolation. IDW is a weighted-averaged interpolation method which preserves the local maxima and produces a smooth reconstruction. Gao *et al.* [40] proposed the use of Taylor series expansion about the body point coupled with IDW to interpolate at the ghost-cells.

Incorporation of various boundary conditions in GCIBM was demonstrated by Tseng & Ferziger [41]. Mittal *et al.* [42] and De [43] extended GCIBM to problems involving highly complex three-dimensional and moving boundaries. Lee & You [44] coupled GCIBM with the mass source/sink algorithm [37] for controlling spurious force oscillations which appears for moving boundary problems using IBM in the inertial frame of reference.

Recently, Peter & De [45] has highlighted advantages of using GCIBM in the non-inertial frame of reference. Earlier Kim & Choi [46] extended the mass source/sink algorithm [37] in the non-inertial frame of reference to solve flow around an arbitrarily moving body. An extensive review on the developments, usage and implications of IBM can be found in the article by Mittal & Iaccarino [47].

1.4 Need of the present work

Firstly, numerous studies exist on free and forced vibrations for a circular cylinder in uniform flow, but for a sphere the first work by Williamson & Govardhan [48] appeared as late as in 1997. The reason can be attributed to the complexity in modelling and analysis for a three-dimensional flow. Since 1997 few studies have

been undertaken on VIV of a sphere, but forced vibration is yet to be reported.

Structures in a flow can acquire motions along any of the six degrees of freedom (*dof*). VIV studies usually consider three translational *dof* and neglect the rotational ones. Only a few studies [49–52] exist on combined rotational and translational motions. These studies considered a two-dimensional object (circular cylinder) and extension to a three-dimensional structure (sphere) is yet to be explored.

Lastly immersed boundary method needs to be advanced by applying it on problems that involve complex flow behaviour and boundary movement.

1.4.1 Thesis statement

The present thesis attempts to reveal the physics involved in following two problems: 1) Uniform flow past a transversely oscillating sphere and 2) Uniform flow past a simultaneously oscillating and rotating sphere. Both these problems raise several questions along with varying level of difficulties.

1. Questions for the first problem
   (a) Can forced transverse oscillation of a sphere in uniform flow predict the VIV modes as in the case of a circular cylinder?
   (b) When and why, the coefficient of energy C_E (normalized work done by fluid force to displace structure over an oscillation cycle) is negative?
   (c) Within the synchronization, what ensures equality between the forcing (f_e) and shedding (f_s) frequencies?
   (d) Within the synchronization for a circular cylinder, two different vortex formation mechanism occur, what happens for a sphere?
2. Questions for the second problem
   (a) Can synchronization persist if the oscillating sphere also rotates?
   (b) Is there a symmetry in the flow for a simultaneously oscillating and rotating sphere?

(c) Does orientation of the rotational axis change the flow features?

(d) Will the flow physics alter at a different frequency ratio?

1.4.2 Organization of the thesis

Following the introduction a detailed description of the mathematical modelling and numerical methods are provided in chapter 2. The present numerical code has been tested for 1) flow past a stationary sphere and 2) flow past a transversely oscillating and rotating circular cylinders. The test results along with the performance evaluation in parallel is reported in chapter 3. The final two chapters, 4 and 5 deal with the two problems mentioned above. Finally, chapter 6 summarizes the result and predicts scope for future work.

Chapter 2

Mathematical modelling

This chapter systematically describes the governing equations and numerical techniques required to solve them. Detailed discussion on immersed boundary method and its implementaion issues are also included.

2.1 Governing equations

The mass and momentum conservation equations for incompressible flow in the inertial frame of reference are given by

$$\frac{\partial u_i}{\partial x_i} = 0 \tag{2.1}$$

$$\frac{\partial u_i}{\partial t} + \frac{\partial (u_i u_j)}{\partial x_j} = -\frac{1}{\rho}\frac{\partial p}{\partial x_i} + \nu \frac{\partial^2 u_i}{\partial x_j \partial x_j} \tag{2.2}$$

where u_i, p and t represent the i-th component ($i = x, y, z$) of velocity, pressure and time, respectively while density (ρ) and kinematic viscosity (ν) are considered as constants.

Reference frames

Figure 2.1 shows a non-inertial frame (x', y', z') whose origin O' is accelerating with an acceleration of $\widetilde{A_i} = \dfrac{d\widetilde{U_i}}{dt}$ relative to the inertial frame (x, y, z) having origin

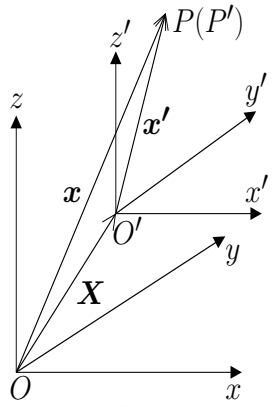

Figure 2.1: Relation between inertial and non-inertial frames of reference

at O. The transformation rule [53] between these two frames is given by

$$x_i = \widetilde{X_i} + x'_i \tag{2.3}$$

where $x_i, \widetilde{X_i}$ are the position vectors of P and O' in the inertial frame while x'_i is the position vector of P' in the non-inertial frame. Differentiating the above coordinate transformation rule with respect to time, we get

$$u_i = \widetilde{U}_i + u'_i \tag{2.4}$$

where $\widetilde{U}_i$ is the velocity of O' as observed from O while u'_i is the velocity of P' in the non-inertial frame.

Equations in non-inertial frame

When the transformation rules (2.3 & 2.4) are inserted into Eqs. (2.1) & (2.2) they modify to

$$\frac{\partial u'_i}{\partial x'_i} = 0 \tag{2.5}$$

$$\frac{\partial u'_i}{\partial t} + \frac{\partial (u'_i u'_j)}{\partial x'_j} = -\frac{1}{\rho}\frac{\partial p'}{\partial x'_i} + \nu \frac{\partial^2 u'_i}{\partial x'_j \partial x'_j} - \widetilde{A_i} \tag{2.6}$$

Normalized governing equations

Using the scales shown in Table 2.1, normalized form of the governing equations in the non-inertial frame of reference are obtained as (discarding $*$ for convenience)

$$\frac{\partial u_i}{\partial x_i} = 0 \tag{2.7}$$

$$\frac{\partial u_i}{\partial t} + \frac{\partial (u_i u_j)}{\partial x_j} = -\frac{\partial p}{\partial x_i} + \frac{1}{Re}\frac{\partial^2 u_i}{\partial x_j \partial x_j} - a_i \tag{2.8}$$

where $Re = UL/\nu$ is the Reynolds number associated with the flow and a_i is the

Variable	Scale	Normalized variable
Length (x_i')	L	$x_i{}^* = x_i'/L$
Velocity (u_i')	U	$u_i{}^* = u_i'/U$
Time (t')	L/U	$t^* = t'/(L/U)$
Pressure (p')	ρU^2	$p^* = p'/\rho U^2$

Table 2.1: Normalization scales and the normalized variables

normalized acceleration of the non-inertial frame.

2.2 Numerical details

If the spatial terms are approximated, then the semi-discrete form of Eq. (2.8) is

$$\frac{du_i}{dt} + C_i = -\delta_i p + D_i - a_i \tag{2.9}$$

where $C_i, D_i, \delta_i p$ & a_i are discrete approximation of the convective, diffusive acceleration, pressure gradient and frame acceleration, respectively.

2.2.1 Time integration

Numerical Integration of the semi-discrete form written above results in fully discrete equations which can be subsequently solved.

Crank-Nicolson (CN)

An implicit, two-time-level technique for Eq. (2.9) is given by

$$\frac{{u_i}^{n+1} - {u_i}^{n}}{\Delta t} + \frac{1}{2}\left(C_i^{n+1} + C_i^{n}\right) = -\frac{1}{2}\left(\delta_i p^{n+1} + \delta_i p^{n}\right) + \frac{1}{2}\left(D_i^{n+1} + D_i^{n}\right) - \frac{1}{2}\left(a_i^{n+1} + a_i^{n}\right)$$

Adams Bashforth Crank-Nicolson (ABCN)

An explicit, multi-time-level technique (***AB***) for the non-linear term and ***CN*** for all the linear terms yield

$$\frac{{u_i}^{n+1} - {u_i}^{n}}{\Delta t} + \frac{1}{2}\left(3C_i^{n} - C_i^{n-1}\right) = -\frac{1}{2}\left(\delta_i p^{n+1} + \delta_i p^{n}\right) + \frac{1}{2}\left(D_i^{n+1} + D_i^{n}\right) - \frac{1}{2}\left(a_i^{n+1} + a_i^{n}\right)$$

where ϕ^n denotes ϕ at n-th time level and Δt is the time increment.

2.2.2 Finite volume method

Figure 2.2 depicts a typical control volume (CV) considered to integrate each term

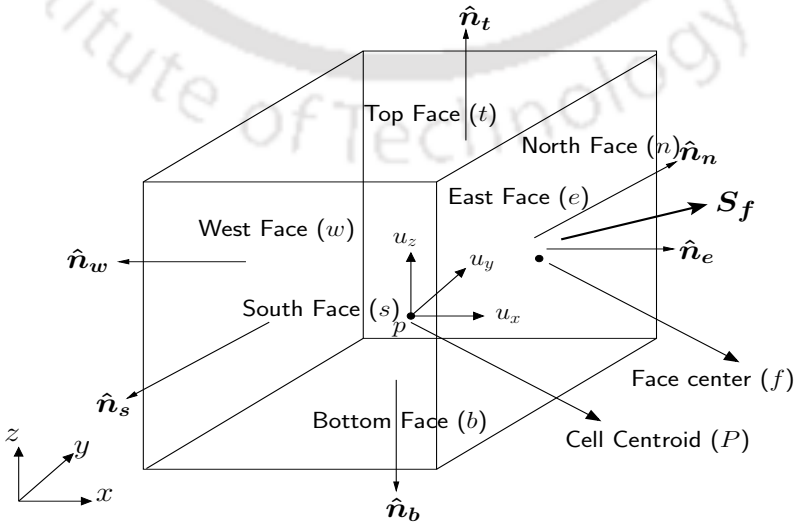

Figure 2.2: A typical control volume (CV)

in Eqs. (2.7) and (2.8). The flow variables (u_i, p) are defined at the centroid (P) of the CV. The six faces that bound the CV along with their outward unit normal is shown in the figure.

Integration of Eq. (2.7) over this CV can be simplified by using the divergence theorem

$$\int_V \frac{\partial u_i}{\partial x_i}\, dV = \int_V \nabla \,.\, \boldsymbol{u}\, dV = \int_S \boldsymbol{u} \,.\, \hat{\boldsymbol{n}}\, dS$$

The second-order approximation of the surface integral is

$$\int_S \boldsymbol{u} \,.\, \hat{\boldsymbol{n}}\, dS \approx \sum_f \boldsymbol{u_f} \,.\, \boldsymbol{S_f}$$

where $\boldsymbol{u_f}$ and $\boldsymbol{S_f}$ are the velocity at a face center and the area vector, respectively. Since the flow rate or mass flux through a face (f) is given by $F_f = \boldsymbol{u_f} \cdot \boldsymbol{S_f}$, one can write

$$\int_V \frac{\partial u_i}{\partial x_i}\, dV = \int_V \nabla \,.\, \boldsymbol{u}\, dV = \int_S \boldsymbol{u} \,.\, \hat{\boldsymbol{n}}\, dS \approx \sum_f \boldsymbol{u_f} \,.\, \boldsymbol{S_f} \approx \sum_f F_f$$

As the mesh is stationary, integration of the temporal acceleration over the CV reduces to

$$\int_V \frac{\partial u_i}{\partial t}\, dV = \frac{\partial}{\partial t} \int_V u_i\, dV \text{ (as the grid is fixed w.r.t. } t)$$

The above integral can be approximated by considering u_i as a polynomial of any degree. However, higher degrees polynomials require the knowledge of u_i at the vertices in addition to P. A linear polynomial results in a second-order approximation

$$\frac{\partial}{\partial t} \int_V u_i\, dV \approx \frac{\partial}{\partial t} \left(u_{i,P} V_P\right) \approx \frac{\partial (u_{i,P})}{\partial t} V_P + O[(\Delta x)^2, (\Delta y)^2, (\Delta z)^2]$$

The non-linear convective term can be simplified by using a second-order approximation for the resulting surface integral

$$\int_V \frac{\partial(u_i u_j)}{\partial x_j}\, dV = \int_V \nabla\,.\,(\boldsymbol{uu})\, dV = \int_S \boldsymbol{u}\,(\boldsymbol{u}\,.\,\hat{\boldsymbol{n}}\, dS) \approx \sum_f \boldsymbol{u_f}\,(\boldsymbol{u_f}\,.\,\boldsymbol{S_f}) \approx \sum_f u_{i,f} F_f$$

Volume integral of the pressure gradient in Eq. (2.8) is

$$\int_V \frac{\partial p}{\partial x_i}\, dV = \int_V \hat{\boldsymbol{n}}_{\boldsymbol{i}}\,.\,\nabla p\, dV$$

where $\hat{\boldsymbol{n}}_{\boldsymbol{i}}$ represents unit vector along the i-th direction. Since $\nabla\,.\,(p\;\hat{\boldsymbol{n}}_{\boldsymbol{i}}) = p\nabla\,.\,\hat{\boldsymbol{n}}_{\boldsymbol{i}} + \hat{\boldsymbol{n}}_{\boldsymbol{i}}\,.\,\nabla p$; and $\nabla\,.\,\hat{\boldsymbol{n}}_{\boldsymbol{i}} = 0$ one can express $\hat{\boldsymbol{n}}_{\boldsymbol{i}}\,.\,\nabla p$ in divergence form which facilitates its further simplification

$$\int_V \hat{\boldsymbol{n}}_{\boldsymbol{i}}\,.\,\nabla p\, dV = \int_V \nabla\,.\,(p\,\hat{\boldsymbol{n}}_{\boldsymbol{i}})\, dV = \int_S p\,(\hat{\boldsymbol{n}}_{\boldsymbol{i}}\,.\,\hat{\boldsymbol{n}}\, dS) \approx \sum_f p_f S_{f,i}$$

where $S_{f,i}$ represents the i-th component of the area vector at a face f.
Volume integral of the diffusion term in straight forward as it is already in divergence form

$$\int_V \frac{1}{Re}\frac{\partial^2 u_i}{\partial x_j \partial x_j}\, dV = \frac{1}{Re}\int_V \nabla\,.\,\nabla \boldsymbol{u}\, dV = \frac{1}{Re}\int_S \nabla \boldsymbol{u}\,.\,\hat{\boldsymbol{n}}\, dS$$
$$\approx \frac{1}{Re}\sum_f (\nabla \boldsymbol{u})_f\,.\,\boldsymbol{S_f} \approx \frac{1}{Re}\sum_f (\nabla u_i)_f\,.\,\boldsymbol{S_f} \approx \frac{1}{Re}\sum_f F_{df u_i}$$

here we represent $(\nabla u_i)_f\,.\,\boldsymbol{S_f}$ as diffusion flux $F_{df u_i}$ at a face f for convenience.

Computation of diffusion flux is explained here for one face since rest of them will follow the same way. Figure 2.3 shows the east face of a CV with centroid P having the neighbouring east cell centered at E. The four edges of this face shared by the south, north, bottom and top faces are denoted as edge centers se, ne, be and te, respectively. The outward surface normal vector is expressed as

$$\boldsymbol{S_e} = \alpha_1 \hat{\boldsymbol{n}}_{\boldsymbol{1}} + \alpha_2 \hat{\boldsymbol{n}}_{\boldsymbol{2}} + \alpha_3 \hat{\boldsymbol{n}}_{\boldsymbol{3}}$$

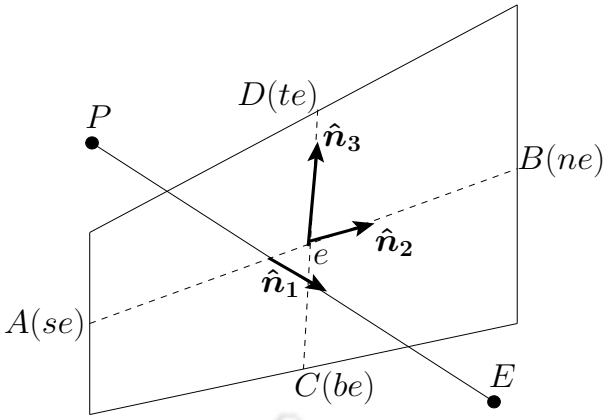

Figure 2.3: Diffusion flux computation at the east face

where $\hat{\boldsymbol{n}}_1$, $\hat{\boldsymbol{n}}_2$ and $\hat{\boldsymbol{n}}_3$ are three linearly independent unit vectors (not necessarily orthogonal) along $\overrightarrow{PE}$, $\overrightarrow{AB}$ and $\overrightarrow{CD}$, respectively. Thus,

$$F_{deu_i} = (\nabla u_i)_e \,.\, \boldsymbol{S_e} = \alpha_1 (\nabla u_i)_e \,.\, \hat{\boldsymbol{n}}_1 + \alpha_2 (\nabla u_i)_e \,.\, \hat{\boldsymbol{n}}_2 + \alpha_3 (\nabla u_i)_e \,.\, \hat{\boldsymbol{n}}_3$$

Now if Δx_1, Δx_2 and Δx_3 are three line segments and Δu_{i1}, Δu_{i2} and Δu_{i3} are differential changes in u_i along $\hat{\boldsymbol{n}}_1$, $\hat{\boldsymbol{n}}_2$ and $\hat{\boldsymbol{n}}_3$ such that

$$\Delta x_1 = |\overrightarrow{PE}|, \qquad \Delta x_2 = |\overrightarrow{AB}|, \qquad \Delta x_3 = |\overrightarrow{CD}|$$

$$\Delta u_{i1} = u_{i,E} - u_{i,P}, \qquad \Delta u_{i2} = u_{i,ne} - u_{i,se}, \qquad \Delta u_{i3} = u_{i,te} - u_{i,be}$$

then we can write

$$\Delta u_{i1} = (\nabla u_i)_e \,.\, \hat{\boldsymbol{n}}_1 \Delta x_1, \qquad \Delta u_{i2} = (\nabla u_i)_e \,.\, \hat{\boldsymbol{n}}_2 \Delta x_2, \qquad \Delta u_{i3} = (\nabla u_i)_e \,.\, \hat{\boldsymbol{n}}_3 \Delta x_3$$

Using the above relation diffusion flux at the east face reduces to

$$(\nabla u_i)_e \,.\, \boldsymbol{S_e} = \alpha_1 \frac{\Delta u_{i1}}{\Delta x_1} + \alpha_2 \frac{\Delta u_{i2}}{\Delta x_2} + \alpha_3 \frac{\Delta u_{i3}}{\Delta x_3}$$

If the surface vector $\boldsymbol{S_e}(S_{e1}, S_{e2}, S_{e3})$ is written in terms of the components of

$\hat{\boldsymbol{n}}_{\boldsymbol{1}}(n_{11}, n_{12}, n_{13}), \hat{\boldsymbol{n}}_{\boldsymbol{2}}(n_{21}, n_{22}, n_{23})$ and $\hat{\boldsymbol{n}}_{\boldsymbol{3}}(n_{31}, n_{32}, n_{33})$ then the matrix equation

$$\begin{bmatrix} n_{11} & n_{21} & n_{31} \\ n_{12} & n_{22} & n_{32} \\ n_{13} & n_{23} & n_{33} \end{bmatrix} \begin{Bmatrix} \alpha_1 \\ \alpha_2 \\ \alpha_3 \end{Bmatrix} = \begin{bmatrix} S_{e1} \\ S_{e2} \\ S_{e3} \end{bmatrix}$$

can be solved to obtain α_1, α_2 and α_3. Note the above coefficient matrix is always non-singular owing to the assumed linear independence of $\hat{\boldsymbol{n}}_{\boldsymbol{1}}$, $\hat{\boldsymbol{n}}_{\boldsymbol{2}}$ and $\hat{\boldsymbol{n}}_{\boldsymbol{3}}$.
As the rectilinear acceleration of the coordinate frame is only time dependent its volume integral is simply

$$\int_V a_i \, dV \approx a_{i,P} V_P + O[(\Delta x)^2, (\Delta y)^2, (\Delta z)^2]$$

Geometrical parameters

The volume and surface areas of the six faces of a CV are computed by defining the diagonal vectors $\boldsymbol{r_{ij}} = \boldsymbol{r_i} - \boldsymbol{r_j}$, where $\boldsymbol{r_i}$ and $\boldsymbol{r_j}$ are the position vectors of the vertices i and j, respectively, shown in Fig. 2.4

$$\begin{aligned}
\text{East face} : \boldsymbol{S_e} &= \frac{1}{2}(\boldsymbol{r_{74}} \times \boldsymbol{r_{83}}) \\
\text{West face} : \boldsymbol{S_w} &= \frac{1}{2}(\boldsymbol{r_{16}} \times \boldsymbol{r_{52}}) \\
\text{North face} : \boldsymbol{S_n} &= \frac{1}{2}(\boldsymbol{r_{27}} \times \boldsymbol{r_{63}}) \\
\text{South face} : \boldsymbol{S_s} &= \frac{1}{2}(\boldsymbol{r_{18}} \times \boldsymbol{r_{45}}) \\
\text{Top face} : \boldsymbol{S_t} &= \frac{1}{2}(\boldsymbol{r_{57}} \times \boldsymbol{r_{86}}) \\
\text{Bottom face} : \boldsymbol{S_b} &= \frac{1}{2}(\boldsymbol{r_{13}} \times \boldsymbol{r_{24}}) \\
\text{Volume} : V &= \boldsymbol{r_{71}} \cdot (\boldsymbol{S_n} + \boldsymbol{S_b} + \boldsymbol{S_w})
\end{aligned}$$

Discretized equations

Thus, using the integral approximations discussed above the governing equations now reduce to fully discrete form

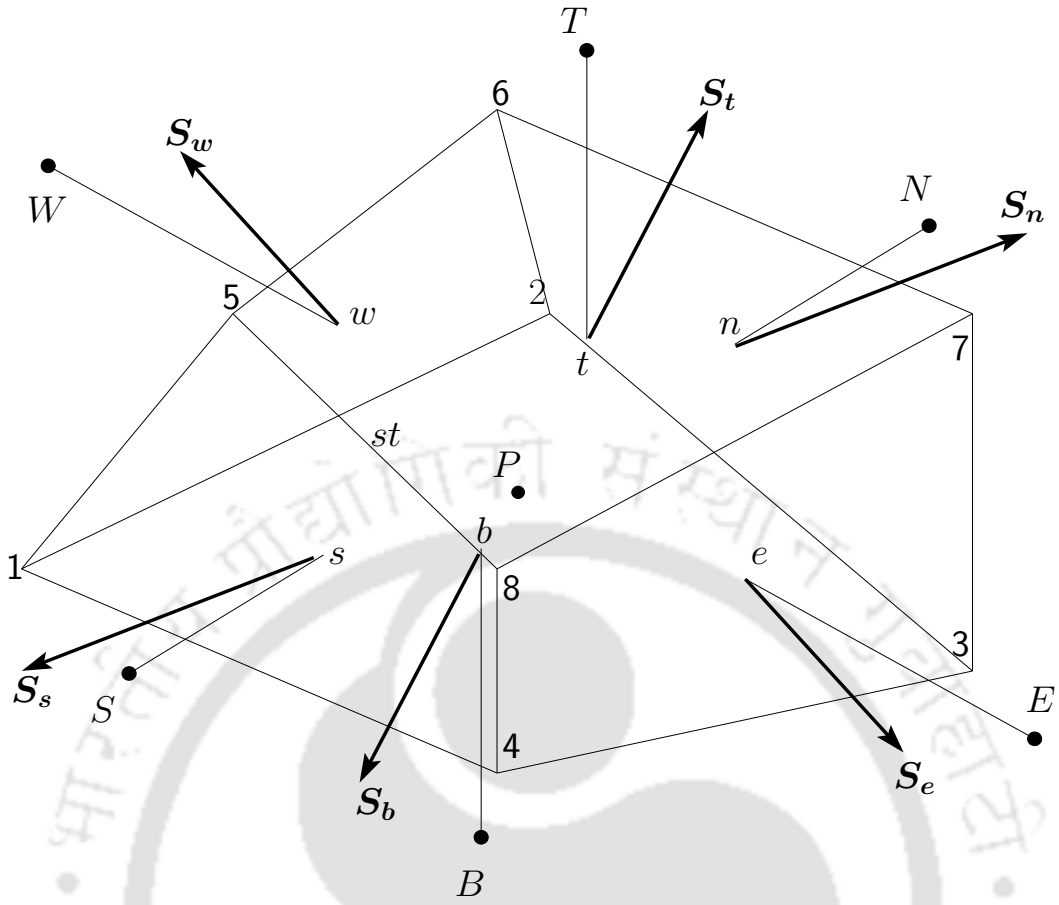

Figure 2.4: Geometrical features of a typical finite volume

Discrete Continuity equation:

$$\sum_f F_f^{n+1} = 0 \tag{2.10}$$

Discrete Momentum equation using Explicit time integration (ABCN) technique:

$$\begin{aligned} &\frac{u_{i,P}^{n+1} - u_{i,P}^{n}}{\Delta t} V_P + \frac{1}{2} \sum_f \left(3F_f^n u_{i,f}^n - F_f^{n-1} u_{i,f}^{n-1} \right) \\ = \; & -\frac{1}{2} \sum_f \left(p_f^{n+1} + p_f^n \right) S_{f,i} + \frac{1}{2Re} \sum_f \left(F_{dfu_i}^{n+1} + F_{dfu_i}^n \right) - \frac{V_P}{2} \left({a_i}^{n+1} + {a_i}^n \right) \end{aligned} \tag{2.11}$$

and using Implicit time integration (CN) technique:

$$\frac{u_{i,P}^{n+1} - u_{i,P}^{n}}{\Delta t} V_P + \frac{1}{2} \sum_f \left(F_f^{n+1} u_{i,f}^{n+1} + F_f^{n} u_{i,f}^{n} \right)$$
$$= -\frac{1}{2} \sum_f \left(p_f^{n+1} + p_f^{n} \right) S_{f,i} + \frac{1}{2Re} \sum_f \left(F_{df u_i}^{n+1} + F_{df u_i}^{n} \right) - \frac{V_P}{2} \left({a_i}^{n+1} + {a_i}^{n} \right) \quad (2.12)$$

To retain the locally second-order accurate form, face interpolation required for the convective flux is carried out using a linear polynomial. This approximation is written here for the east face

$$\phi_e = \frac{\phi_P V_E + \phi_E V_P}{V_P + V_E}$$

Velocity-pressure coupling

First a provisional velocity ($\boldsymbol{u}^*$) is computed, excluding the pressure term [43, 54] in Eq. (2.11) or (2.12), and using the latest available mass flux ($F_f^{n+1,l}$), by solving the equation

$$\frac{u_{i,P}^{*} - u_{i,P}^{n}}{\Delta t} V_P + \frac{1}{2} \sum_f \left(F_f^{n+1,l} u_{i,f}^{*} + F_f^{n} u_{i,f}^{n} \right)$$
$$= \frac{1}{2Re} \sum_f \left(F_{df u_i}^{*} + F_{df u_i}^{n} \right) - \frac{V_P}{2} \left({a_i}^{n+1} + {a_i}^{n} \right) \quad (2.13)$$

The provisional (tentative) mass flux ($F_f{}^*$) follows immediately using the provisional face velocity ($\boldsymbol{u_f^*}$)

$$F_f{}^* = \boldsymbol{u_f}^* \,.\, \boldsymbol{S_f} \quad (2.14)$$

The correct face velocity ($\boldsymbol{u_f}$) is conceived by adding the local pressure gradient

$$\boldsymbol{u_f} = \boldsymbol{u_f^*} - \Delta t (\nabla p)_f \quad (2.15)$$

Since this corrected velocity has the pressure gradient in-built into it, mass flux calculated from it is expected to be physically correct. This step [54] is close to the Rhie-Chow interpolation [55] procedure. Thus, the new estimate of mass flux

is

$$F_f{}^{n+1,l+1} = \boldsymbol{u_f} \,.\, \boldsymbol{S_f} = \boldsymbol{u_f^*} \,.\, \boldsymbol{S_f} - \Delta t(\nabla p)_f \,.\, \boldsymbol{S_f} = F_f^* - \Delta t(\nabla p)_f \,.\, \boldsymbol{S_f} \tag{2.16}$$

which must satisfy the discrete continuity equation. Substitution of Eq. (2.16) in Eq. (2.10) yields a pressure Poisson equation

$$\sum_f (\nabla p)_f \,.\, \boldsymbol{S_f} = \frac{1}{\Delta t} \sum_f F_f{}^* \tag{2.17}$$

The pressure field (p) obtained from Eq. (2.17) is used in Eq. (2.16) to update $F_f{}^{n+1,l+1}$. In explicit procedure pressure obtained from Eq. (2.17) is used to solve Eq. (2.11) to obtain the final velocity field. However, Eqs. (2.13) & (2.17) are repeatedly solved with Eq. (2.16) as updating expression until the mass flux ceases to change in implicit procedure. Once the mass flux has converged, like in the explicit procedure, the final velocity field is obtained.

2.3 GCIBM modified

Figure 2.5 shows a typical near boundary stencil comprising of a ghost-cell (G), immediate neighbouring fluid cells ($F_1, F_2, \ldots$) and boundary point (B). The boundary (or forcing) point is so chosen that $\overrightarrow{GB}$ points in the outward surface normal direction at B. The fluid neighbours $F_1, F_2, F_3, F_4 \ldots F_n, F_{n+1}$ are at distances $h_1 < h_2 < h_3 < h_4 \ldots h_n < R$ from B. Instead of fitting a localized polynomial [38, 41–44], Taylor series expansion about B can serve to reconstruct [40] the solution at G

$$\phi_G = \phi_B + \Delta x_i \left(\frac{\partial \phi}{\partial x_i}\right)_B + \frac{1}{2}\Delta x_i \Delta x_j \left(\frac{\partial^2 \phi}{\partial x_i \partial x_j}\right)_B + 3^{rd}\text{-order terms} \tag{2.18}$$

where i, j expand for spatial directions with $\Delta x_i = x_{i,G} - x_{i,B}$ $(i = x, y, z)$.

At the boundary point (B) inverse distance weighting [40] interpolation can be

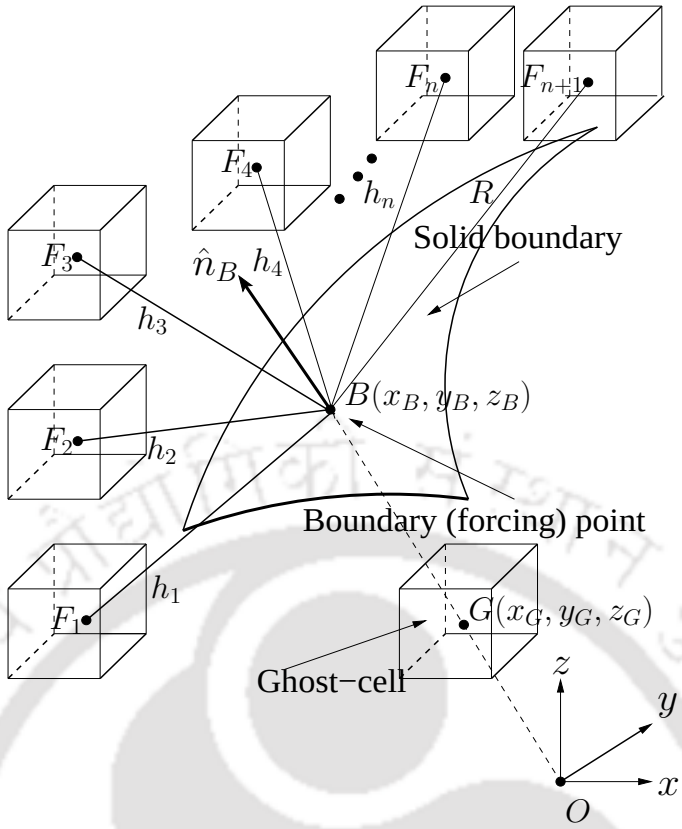

Figure 2.5: Schematic diagram for evaluating flow variables at G.

used for the flow variables and their partial derivatives

$$\text{flow variables:} \qquad \phi_B = \frac{1}{q}\sum_{m=1}^{n} w_m \phi_m \tag{2.19}$$

$$\text{first derivative:} \qquad \left(\frac{\partial \phi}{\partial x_i}\right)_B = \frac{1}{q}\sum_{m=1}^{n} w_m \left(\frac{\partial \phi}{\partial x_i}\right)_m \tag{2.20}$$

$$\text{second derivative:} \qquad \left(\frac{\partial^2 \phi}{\partial x_i \partial x_j}\right)_B = \frac{1}{q}\sum_{m=1}^{n} w_m \left(\frac{\partial^2 \phi}{\partial x_i \partial x_j}\right)_m \tag{2.21}$$

where $w_m = (1/h_m - 1/R)^2$ is the weighting coefficients and $q = \sum_{m=1}^{n} w_m$. All the derivatives at the fluid points are calculated (see Appendix) on a non-uniform grid with the latest available values of the flow variables instead of previous time step values on a uniform grid [40]. It has been observed that the number of supporting points $n = 4{-}5$ (excluding the one with distance R) are enough to enforce the

boundary conditions on the immersed surface satisfactorily which is in agreement with Gao *et al.* [40].

Dirichlet boundary condition: A specified value for a variable ϕ_D implies

$$\phi_B = \phi_D \tag{2.22}$$

Thus the ghost point value (ϕ_G) can be evaluated using Eqs. (2.18)−(2.22)

Neumann boundary condition: If $\hat{n}$ is the unit normal vector (n_x, n_y, n_z) at B, a specified normal gradient for a variable ϕ' implies

$$(\nabla\phi)_B \,.\, \hat{n}_B = \phi' \tag{2.23}$$

This condition simplifies to

$$\left(n_x \frac{\partial\phi}{\partial x}\right)_B + \left(n_y \frac{\partial\phi}{\partial y}\right)_B + \left(n_z \frac{\partial\phi}{\partial z}\right)_B = \phi'$$

$$\implies \left(\frac{\partial\phi}{\partial z}\right)_B = \frac{\phi' - n_x \frac{\partial\phi}{\partial x}\Big|_B - n_y \frac{\partial\phi}{\partial y}\Big|_B}{n_z} \tag{2.24}$$

The second derivatives can be calculated as follows

$$\left(\frac{\partial^2\phi}{\partial x_i \partial z}\right)_B = \left(\frac{\partial}{\partial x_i}\left\{\frac{\partial\phi}{\partial z}\right\}\right)_B$$

In case of planar object ($n_z = 0$), either $\frac{\partial\phi}{\partial x}$ or $\frac{\partial\phi}{\partial y}$ replaces $\frac{\partial\phi}{\partial z}$ in Eq. (2.24), thereby making it applicable for any geometry with an implicit analytical description of the surface.

Application of GCIBM to moving boundary problems

Flow past a accelerating body can be solved in inertial or non-inertial frames of reference. In the inertial frame of reference, as the body moves all geometrical constructions need to be recomputed at every time step which slows the calculations. Moreover, since the body and thus the associated ghost-cells move frequently, the above mentioned issue of complex communications take the center stage. Also, the application of IBM to moving boundary problems in the inertial

frame of reference encounters spurious force oscillation. The use of non-inertial frame avoids these difficulties as the body remains stationary, and only the boundary moves which is accommodated in the boundary conditions.

2.4 Linear solver

Numerical approximation of the governing equations and boundary conditions, as described in sections 2.2 & 2.3, reduce them to set of simultaneous algebraic equations. Owing to the local nature of these approximations, the coefficient matrices are sparse and banded, which is exploited during their solution. The generic resulting form of these equations is

$$a_S\phi_S + a_B\phi_B + a_W\phi_W + a_P\phi_P + a_E\phi_E + a_T\phi_T + a_N\phi_N = b_P$$

where $a_S, a_B, a_W, a_E, a_T, a_N$ are the coefficients corresponding to neighbouring cells denoted by S, B, W, E, T, N, while a_P corresponds to the point P as shown in Fig. 2.4; and b_P represents the right-hand side. Thus, for the highly sparse linear system

$$A\boldsymbol{\phi} = \boldsymbol{b} \tag{2.25}$$

A has seven non-zero diagonals, corresponding to six immediate neighbours and point P itself.

Iterative methods in general are of the form

$$M\boldsymbol{\phi}^{l+1} = N\boldsymbol{\phi}^{l} + \boldsymbol{b} \tag{2.26}$$

where M, N are iteration matrices and l is the iteration count. Since at the convergence $\boldsymbol{\phi}^{l+1} \longrightarrow \boldsymbol{\phi}^{l} \longrightarrow \boldsymbol{\phi}$ the above equation yields

$$M\boldsymbol{\phi} = N\boldsymbol{\phi} + \boldsymbol{b} \Longrightarrow (M - N)\boldsymbol{\phi} = \boldsymbol{b} \tag{2.27}$$

Thus, for consistency of Eqs. (2.25) and (2.27) $A = M - N$ which is a relation between the original coefficient matrix and the iteration matrices. Equation (2.26) can be cast into the residual form by subtracting $M\boldsymbol{\phi}^l$ from both the sides

$$M\boldsymbol{\phi}^{l+1} - M\boldsymbol{\phi}^l = \boldsymbol{b} - (M-N)\boldsymbol{\phi}^l \Longrightarrow M(\boldsymbol{\phi}^{l+1} - \boldsymbol{\phi}^l) = \boldsymbol{b} - A\boldsymbol{\phi}^l \Longrightarrow M\boldsymbol{\delta}^{l+1} = \boldsymbol{\rho}^l$$

where $\boldsymbol{\delta}^{l+1} = \boldsymbol{\phi}^{l+1} - \boldsymbol{\phi}^l$ is an update in $\boldsymbol{\phi}$ at $(l+1)$ iteration level and $\boldsymbol{\rho}^l = \boldsymbol{b} - A\boldsymbol{\phi}^l$ is the residual after l iterations.

Incomplete LU factorization (ILU)

Matrix A can be uniquely LU factorized by keeping the main diagonal of U as unity, i.e.,

$$A = [\, L_S \;\; L_B \;\; L_W \;\; L_P] \, [\, I \;\; U_E \;\; U_T \;\; U_N]$$

where L_P, L_W, L_S, L_B and U_E, U_T, U_N are non-zero diagonals of L and U. Using the above factors, the original system ($A\boldsymbol{\phi} = \boldsymbol{b}$) becomes

$$[\, L_S \;\; L_B \;\; L_W \;\; L_P] \, [\, I \;\; U_E \;\; U_T \;\; U_N] \, \boldsymbol{\phi} = \boldsymbol{b}$$

carrying out symbolic multiplication of the diagonals leads to first

$$[\, L_S \;\; L_B \;\; L_W \;\; L_P] \, [\phi_P \;+\; U_E\phi_E \;+\; U_T\phi_T \;+\; U_N\phi_N] \;\; = \;\; b_P$$

and finally

$$\begin{aligned}
&(L_P\phi_P + L_PU_E\phi_E + L_PU_T\phi_T + L_PU_N\phi_N) \;\; + \\
&\left(L_W\phi_W + L_WU_{E_{i-1}}\phi_P + \boxed{L_WU_{T_{i-1}}\phi_{TW}} + \boxed{L_WU_{N_{i-1}}\phi_{NW}}\right) \;\; + \\
&\left(L_B\phi_B + \boxed{L_BU_{E_{k-1}}\phi_{BE}} + L_BU_{T_{k-1}}\phi_P + \boxed{L_BU_{N_{k-1}}\phi_{NB}}\right) \;\; + \\
&\left(L_S\phi_S + \boxed{L_SU_{E_{j-1}}\phi_{SE}} + \boxed{L_SU_{T_{j-1}}\phi_{ST}} + L_SU_{N_{j-1}}\phi_P\right) \;\; = \;\; b_p
\end{aligned} \tag{2.28}$$

Note the above equation should be seen in only the locations which differ from i, j or k are mentioned, e.g., $U_{E_{i-1}}$ is $U_{E_{i-1,j,k}}$ and L_W is $L_{W_{i,j,k}}$. The extra terms

other than the seven locations (S, B, W, P, E, T, N) conjunction to Fig. 2.6 and

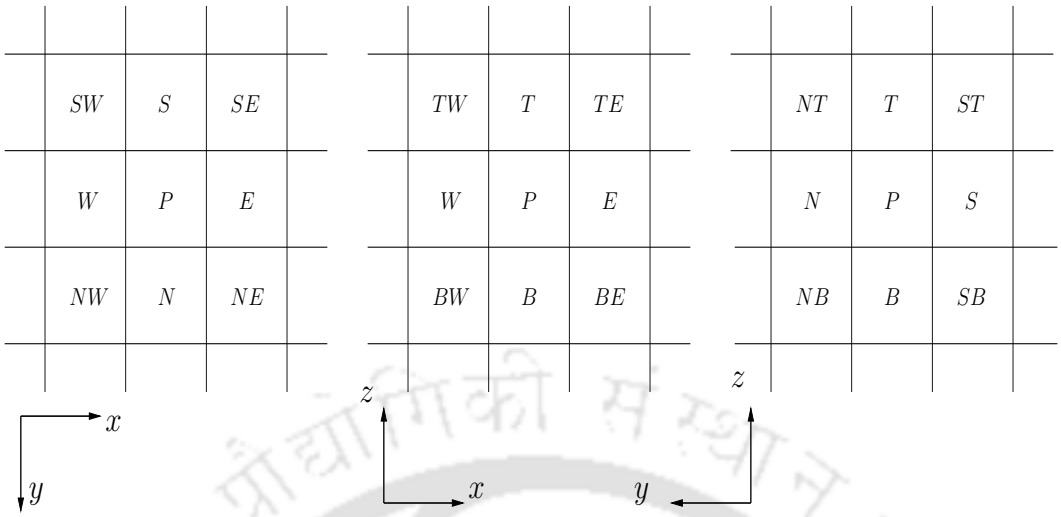

Figure 2.6: Planar view of finite volumes and their neighbors

that arise because of LU multiplication are enclosed in boxes. The factorization given by Eq. (2.28) has to be used for the iteration matrices M and N. Since M must be closest to A, only the seven locations corresponding to the A matrix are considered in M

$$\begin{aligned} M_S = L_S = a_S, M_B = L_B = a_B, M_W = L_W = a_W \\ M_P = L_P + L_W U_{E_{i-1}} + L_S U_{N_{j-1}} + L_B U_{T_{k-1}} = a_P \\ M_E = L_P U_E = a_E, M_T = L_P U_T = a_T, M_N = L_P U_N = a_N \end{aligned} \tag{2.29}$$

The above relations are used to compute L and U diagonals in the following order

$$\begin{aligned} L_S &= a_S \\ L_B &= a_B \\ L_W &= a_W \\ L_P &= a_P - L_W U_{E_{i-1}} - L_S U_{N_{j-1}} - L_B U_{T_{k-1}} \\ U_E &= \frac{a_E}{L_P} \\ U_T &= \frac{a_T}{L_P} \\ U_N &= \frac{a_N}{L_P} \end{aligned} \tag{2.30}$$

As the L and U diagonals of equation (2.30) does not give back Eq. (2.28), it is only an incomplete splitting. To complete the factorization, N should carry the extra diagonals (enclosed ones in Eq. (2.28)) as $A = M + N$.

$$\begin{aligned} N_{TW} = L_W U_{T_{i-1}}, N_{NW} = L_W U_{N_{i-1}} \\ N_{SE} = L_S U_{E_{j-1}}, N_{ST} = L_S U_{T_{j-1}} \\ N_{BE} = L_B U_{E_{k-1}}, N_{NB} = L_B U_{N_{k-1}} \end{aligned} \tag{2.31}$$

Strongly implicit procedure (SIP)

Stone [56] proposed that the convergence can be improved if N, instead of only extra diagonals, has all the diagonals appearing in LU. Moreover, as M must be closer to A, N must be small for faster convergence, i.e., $[N\phi]_P \approx 0$

$$\begin{aligned} \implies N_S\phi_S + N_B\phi_B + N_W\phi_W + N_P\phi_P + N_E\phi_E + N_T\phi_T + N_N\phi_N + \\ N_{TW}\phi_{TW} + N_{NW}\phi_{NW} + N_{SE}\phi_{SE} + N_{ST}\phi_{ST} + N_{BE}\phi_{BE} + N_{NB}\phi_{NB} \approx 0 \end{aligned} \tag{2.32}$$

Thus the effect of extra diagonals is nullified by the other diagonals of N. In other words, Eq. (2.32) should reduce to

$$\begin{aligned} N_{TW}(\phi_{TW} - \phi^*_{TW}) + N_{NW}(\phi_{NW} - \phi^*_{NW}) + N_{SE}(\phi_{SE} - \phi^*_{SE}) + \\ N_{ST}(\phi_{ST} - \phi^*_{ST}) + N_{BE}(\phi_{BE} - \phi^*_{BE}) + N_{NB}(\phi_{NB} - \phi^*_{NB}) \approx 0 \end{aligned} \tag{2.33}$$

where quantities in $*$ account for the diagonals that are originally present in A. The ϕ^* quantities are expressed implicitly in terms of neighbouring nodal values

$$\begin{aligned} \phi^*_{TW} &\approx \gamma(\phi_T + \phi_W - \phi_P), \quad \phi^*_{NW} \approx \gamma(\phi_N + \phi_W - \phi_P) \\ \phi^*_{SE} &\approx \gamma(\phi_S + \phi_E - \phi_P), \quad \phi^*_{ST} \approx \gamma(\phi_S + \phi_T - \phi_P) \\ \phi^*_{BE} &\approx \gamma(\phi_B + \phi_E - \phi_P), \quad \phi^*_{NB} \approx \gamma(\phi_N + \phi_B - \phi_P) \end{aligned}$$

It has been seen from numerical exercises that $\gamma \approx 0.9$ gives the best conver-

gence, though there is no universally accepted value of it that ensures the best convergence for a range of grid structures with different aspect ratios. Inserting the above relations in Eq. (2.33) results in

$$N_{TW}(\phi_{TW} - \gamma\phi_T - \gamma\phi_W + \gamma\phi_P) + N_{NW}(\phi_{NW} - \gamma\phi_N - \gamma\phi_W + \gamma\phi_P) +$$
$$N_{SE}(\phi_{SE} - \gamma\phi_S - \gamma\phi_E + \gamma\phi_P) + N_{ST}(\phi_{ST} - \gamma\phi_S - \gamma\phi_T + \gamma\phi_P) +$$
$$N_{BE}(\phi_{BE} - \gamma\phi_B - \gamma\phi_E + \gamma\phi_P) + N_{NB}(\phi_{NB} - \gamma\phi_N - \gamma\phi_B + \gamma\phi_P) \approx 0$$

If the above equation is compared with Eq. (2.32) non-zero diagonals of N are obtained as

$$\begin{aligned}
N_S &= -\gamma(N_{ST} + N_{SE}) \\
N_B &= -\gamma(N_{BE} + N_{NB}) \\
N_W &= -\gamma(N_{NW} + N_{TW}) \\
N_P &= \gamma(N_{NW} + N_{ST} + N_{SE} + N_{BE} + N_{TW} + N_{NB}) \\
N_E &= -\gamma(N_{SE} + N_{BE}) \\
N_T &= -\gamma(N_{ST} + N_{TW}) \\
N_N &= -\gamma(N_{NW} + N_{NB})
\end{aligned} \tag{2.34}$$

Substituting the diagonals of M from Eq. (2.29) and N from Eq. (2.34) (the diagonals in brackets are same as in ILU, i.e., from Eq. (2.31)) into the matrix relation $A = M - N$ one gets

$$a_S - \gamma L_S U_{T_{j-1}} - \gamma L_S U_{E_{j-1}} = L_S$$
$$a_B - \gamma L_B U_{E_{k-1}} - \gamma L_B U_{N_{k-1}} = L_B$$
$$a_W - \gamma L_W U_{N_{i-1}} - \gamma L_W U_{T_{i-1}} = L_W$$
$$a_P + \gamma L_W U_{N_{i-1}} + \gamma L_S U_{T_{j-1}} + \gamma L_S U_{E_{j-1}} + \gamma L_B U_{E_{k-1}} +$$
$$\gamma L_W U_{T_{i-1}} + \gamma L_B U_{N_{k-1}} = L_P + L_W U_{E_{i-1}} + L_S U_{N_{j-1}} + L_B U_{T_{k-1}}$$
$$a_E - \gamma L_S U_{E_{j-1}} - \gamma L_B U_{E_{k-1}} = L_P U_E$$

$$a_T - \gamma L_S U_{T_{j-1}} - \gamma L_W U_{T_{i-1}} = L_P U_T$$
$$a_N - \gamma L_W U_{N_{i-1}} - \gamma L_B U_{N_{k-1}} = L_P U_N$$

the above relations are used to compute L and U diagonals in the following order

$$\begin{aligned}
L_S &= \frac{a_S}{1+\gamma(U_{T_{j-1}} + U_{E_{j-1}})} \\
L_B &= \frac{a_B}{1+\gamma(U_{E_{k-1}} + U_{N_{k-1}})} \\
L_W &= \frac{a_W}{1+\gamma(U_{N_{i-1}} + U_{T_{i-1}})} \\
L_P &= a_P + \gamma(L_W U_{N_{i-1}} + L_W U_{T_{i-1}} + L_S U_{T_{j-1}} + L_S U_{E_{j-1}} + L_B U_{E_{k-1}} + L_B U_{N_{k-1}}) \\
&\quad - L_W U_{E_{i-1}} - L_S U_{N_{j-1}} - L_B U_{T_{k-1}} \\
U_E &= \frac{a_E - \gamma(L_S U_{E_{j-1}} + L_B U_{E_{k-1}})}{L_P} \\
U_T &= \frac{a_T - \gamma(L_S U_{T_{j-1}} + L_W U_{T_{i-1}})}{L_P} \\
U_N &= \frac{a_N - \gamma(L_W U_{N_{i-1}} + L_B U_{N_{k-1}})}{L_P}
\end{aligned} \tag{2.35}$$

It is to be noted that $\gamma = 0$ in the above equations give equation (2.30); i.e., the L and U diagonals of ILU. After obtaining the L and U factors, we can solve the original system $A\phi = \boldsymbol{b}$ in two steps through the residual form of the iterative methods as follows

$$\begin{aligned}
& LU\boldsymbol{\delta}^{l+1} = \boldsymbol{\rho}^k \\
\Longrightarrow \quad & \text{step 1: forward substitution:} \quad L\boldsymbol{s} = \boldsymbol{\rho}^k \\
\Longrightarrow \quad & \text{step 2: backward substitution:} \quad U\boldsymbol{\delta}^{k+1} = \boldsymbol{s}
\end{aligned}$$

Pre-conditioning

Condition number of a linear system indicates how ready the coefficient matrix is for numerical inversion. During solution either the coefficient matrix or the right hand side vector can pick-up errors. A well-conditioned matrix is less affected by this accumulation of errors. Moreover, conditioning of a matrix refine its spectral

radius in such a way that its eigen values improve the convergence behaviour.

Conditioning of the original A matrix is achieved by pre-multiplying the original system ($A\boldsymbol{\phi} = \boldsymbol{b}$) by inverse of the pre-conditioning matrix (P^{-1})

$$P^{-1}A\boldsymbol{\phi} = P^{-1}\boldsymbol{b} \Longrightarrow \widetilde{A}\boldsymbol{\phi} = \widetilde{\boldsymbol{b}}$$

The above system has a favourable condition number and thus converges much faster than the original system, since $\widetilde{A}$ is closer to the unity matrix than A is. As M in the SIP method is constructed by splitting decomposition (LU), its inversion is cheap and thus can be used as a preconditioner, i.e., $P = M$. The algorithms for the BiCGSTAB technique [57] and its pre-conditioned version are written below

BiCGSTAB technique:

1. Initialize: $\boldsymbol{\phi} = \boldsymbol{\phi_{in}},\ \boldsymbol{r} = \boldsymbol{b} - A\boldsymbol{\phi_{in}},\ \boldsymbol{r_0} = \boldsymbol{r},\ \ \alpha,\ \beta,\ \xi$ any large value, $k = 0$
2. Compute $\boldsymbol{p} = \boldsymbol{r} + \beta(\boldsymbol{p} - \xi A\boldsymbol{p})$
3. $\alpha = \dfrac{||\boldsymbol{r} \cdot \boldsymbol{r_0}||}{||A\boldsymbol{p} \cdot \boldsymbol{r_0}||}$
4. Compute $\boldsymbol{z} = \boldsymbol{r} - \alpha A\boldsymbol{p}$
5. $\xi = \dfrac{||A\boldsymbol{z} \cdot \boldsymbol{z}||}{||A\boldsymbol{z} \cdot A\boldsymbol{z}||}$
6. $\boldsymbol{\phi} = \boldsymbol{\phi} + \alpha\boldsymbol{p} + \xi\boldsymbol{z}$

   $\boldsymbol{r} = \boldsymbol{z} - \xi A\boldsymbol{z}$

   $\beta = \dfrac{\alpha||\boldsymbol{r_0} \cdot \boldsymbol{r}||}{\xi||\boldsymbol{r_0} \cdot \boldsymbol{r}||_{k-1}}$
7. If $||\boldsymbol{b} - A\boldsymbol{\phi}||_{l_2} < \epsilon$ exit else $k \longrightarrow k + 1$ and return to step 2.

BiCGSTAB pre-conditioned by the SIP Method:

1. Initialize: $\boldsymbol{\phi} = \boldsymbol{\phi_{in}},\ \boldsymbol{r} = \boldsymbol{b} - A\boldsymbol{\phi_{in}},\ \boldsymbol{r_0} = \boldsymbol{r},\ \rho_0,\ \alpha,\ \xi$ any large value, $k = 0$
2. $\rho = ||\boldsymbol{r} \cdot \boldsymbol{r_0}||,\ \beta = (\rho\alpha)/(\rho_0\xi)$
3. Compute $\boldsymbol{p} = \boldsymbol{r} + \beta(\boldsymbol{p} - \xi\boldsymbol{v})$

4. Solve $LU\boldsymbol{y} = \boldsymbol{p}$ where L and U factors computed by Eq. (2.35)

5. Compute $\boldsymbol{v} = A\boldsymbol{y}$

6. $\alpha = \dfrac{||\boldsymbol{r} \cdot \boldsymbol{r_0}||}{||A\boldsymbol{y} \cdot \boldsymbol{r_0}||}$

7. Compute $\boldsymbol{s} = \boldsymbol{r} - \alpha\boldsymbol{v}$

8. Solve $LU\boldsymbol{z} = \boldsymbol{s}$ where L and U factors computed by Eq. (2.35)

9. $\xi = \dfrac{||A\boldsymbol{z} \cdot \boldsymbol{s}||}{||A\boldsymbol{z} \cdot A\boldsymbol{z}||}$

10. $\boldsymbol{\phi} = \boldsymbol{\phi} + \alpha\boldsymbol{y} + \xi\boldsymbol{z}$

    $\boldsymbol{r} = \boldsymbol{s} - \xi A\boldsymbol{z}$

    $\rho_0 = \rho$

11. If $||\boldsymbol{b} - A\boldsymbol{\phi}||_{l_2} < \epsilon$ exit else $k \longrightarrow k + 1$ and return to step 2.

2.5 Solution algorithm

The sequential steps that define the entire solution procedure is written here as a flowchart in Fig. 2.7

2.6 Parallel implementation

The present numerical code has parallelized based on the distributed memory allocation. The computational domain is decomposed into a number of sub-domains and each of them is assigned to a processor. At the interfaces of these sub-domains communication of solution variables are performed in the MPI environment to synchronize computations among the processors. All the computations in the present work have been performed using nine processors. Each computing node consists of twelve Intel Xeon E5620 processors powered by 32 GB of memory.

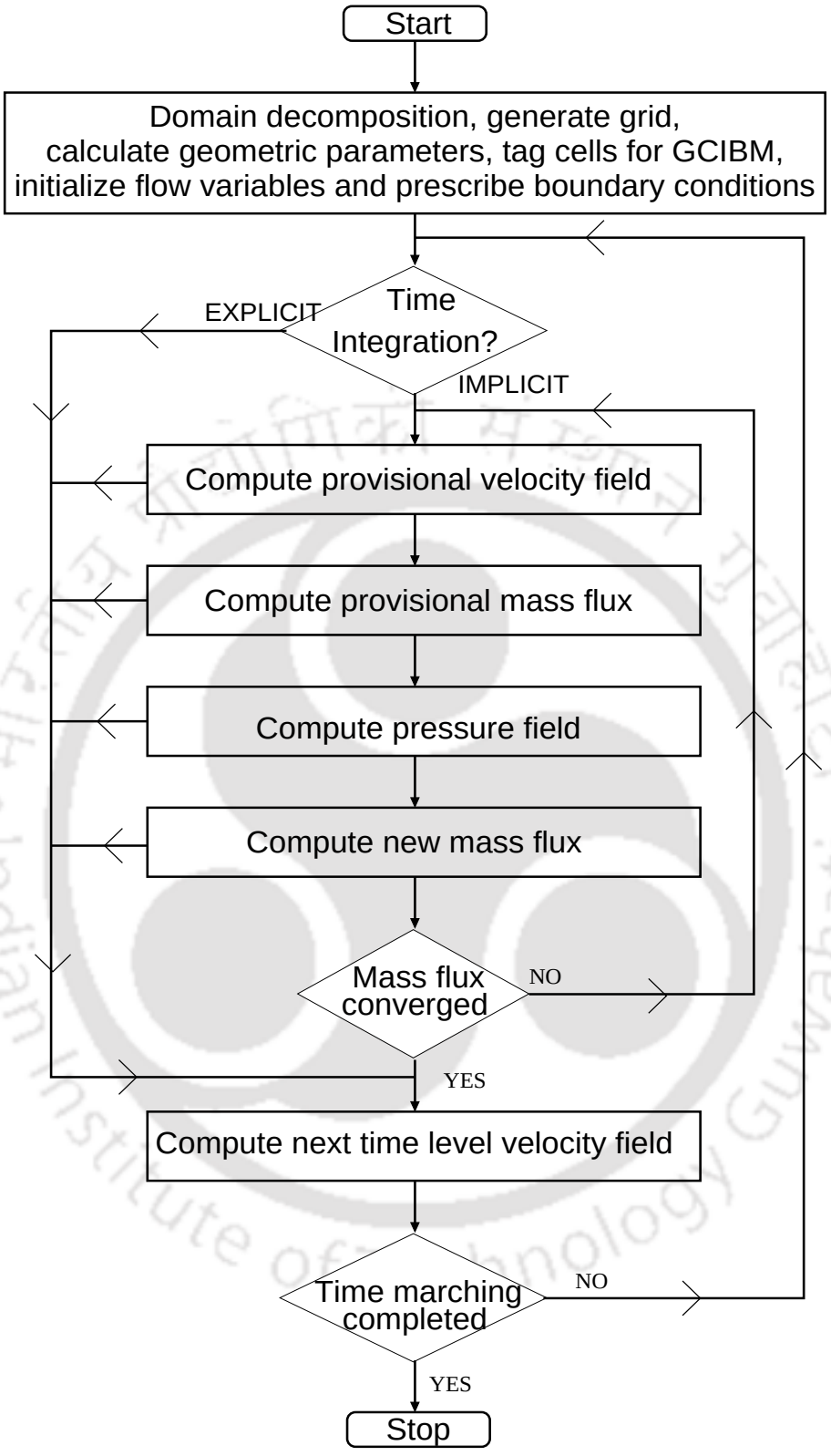

Figure 2.7: Flowchart for the solution steps

Implementation of GCIBM in a distributed memory based parallel environment is a challenging task. If a ghost-cell and its immediate fluid neighbours do not fall

in the same processor, the interpolation required for the boundary reconstruction cannot be carried. Moreover, domain decomposition causes non-uniform distribution of the ghost-cells in the processors. This non-uniformity, affecting the load balancing among computing processors, strongly influences the speed-up, efficiency and convergence behaviour. Also this non-uniform distribution may lead to a stall or blowing up of the computations. To overcome these difficulties there are two approaches: (1) restrict the search for immediate fluid neighbours to the host processor (i.e., where ghost-cell lies) and (2) communicate the information of the fluid neighbors to the relevant processor. The second approach puts an overhead of complex communications, so we have adopted the first approach.

Chapter 3

Performance evaluation of the solver

The numerical strategies described in chapter 2 are tested on three bench mark problems: 1) uniform flow past a stationary sphere, 2) uniform flow past a transversely oscillating circular cylinder and 3) uniform flow past a rotating circular cylinder. The results obtained for these three problems are reported in this chapter.

3.1 Uniform flow past a stationary sphere

The wake behind a sphere is marked by several regimes at increasing Re. Creeping flow in which the flow divides, swims over the surface and reunites at the rear end of the sphere exists for Re →0. The laminar Boundary layer separates at Re ≈20 from the sphere surface leading to a laminar wake. Four flow regimes of laminar wake are: steady axisymmetric ($20 < Re < 210$), steady planar symmetric ($210 < Re < 270$), unsteady planar symmetric ($280 < Re < 420$) and unsteady asymmetric ($420 < Re < 800$).

First regime is characterized with an axisymmetric stationary vortex-ring attached at the rear end of the sphere. In the second regime, the axisymmetry is replaced by a planar symmetry. A trail of two parallel counter rotating vortices

is observed, and is known as the double-threaded wake. The third regime is characterized by the periodic vortex shedding, where vortices are shed as interconnected vortex loops; maintaining a planar symmetry about a plane passing through the wake centerline. In the fourth regime, irregular and asymmetric shedding of hairpin vortices is observed.

3.1.1 Computational details

Figure 3.1 shows schematic diagram describing the problem, computational do-

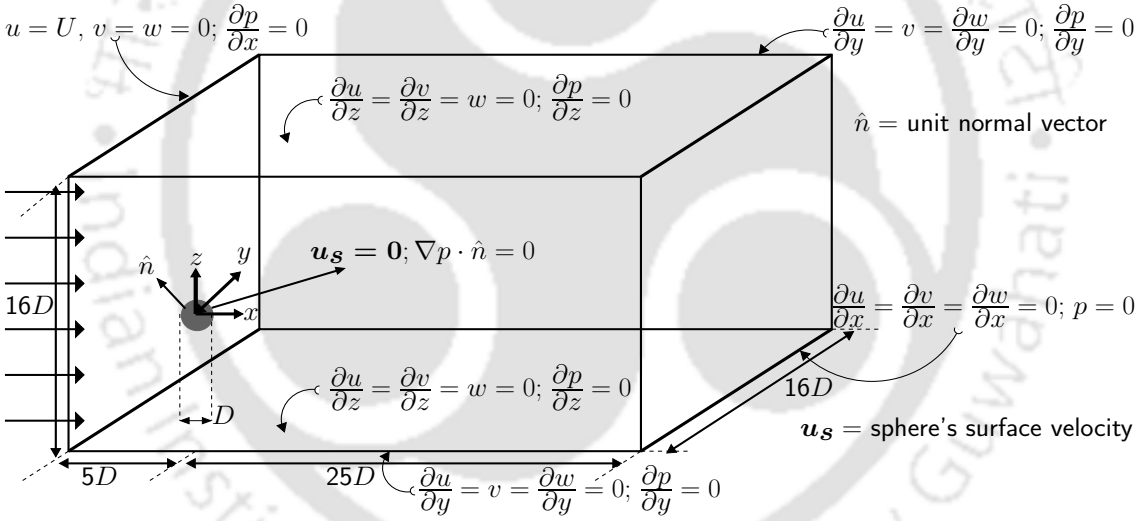

Figure 3.1: Schematic diagram for uniform flow past a stationary sphere

main and boundary conditions employed. Three-dimensional numerical simulations were carried out on a non-uniform cartesian grid $217 \times 181 \times 181$ in the stream-wise (x), lateral (y) and side directions (z), respectively. A cubical domain of edge 3 with grid size $151 \times 151 \times 151$ was used to provide an uniform finer mesh engulfing the sphere which generated grid resolution $\Delta x = \Delta y = \Delta z = 0.02$ in and around the sphere. Computations were performed for $Re = 100,\ 250$ and 300 with time increment $\Delta t = 0.003$.

3.1.2 Body points on the sphere surface

Unit outward normal vector at B (Fig. 2.5) for a sphere, $x^2 + y^2 + z^2 = r^2$ is

$$\hat{\boldsymbol{n}}_{\boldsymbol{B}} = \frac{\hat{i}2x_B + \hat{j}2y_B + \hat{k}2z_B}{\sqrt{4(x_B^2 + y_B^2 + z_B^2)}} = \hat{i}\frac{x_B}{r} + \hat{j}\frac{y_B}{r} + \hat{k}\frac{z_B}{r}$$

Normal to a sphere always passes through its center. To find B such that the normal passes through G, we calculate the unit vector along $\boldsymbol{GB}$ and equate to $\hat{\boldsymbol{n}}_{\boldsymbol{B}}$.

$$\hat{\boldsymbol{n}}_{\boldsymbol{GB}} = \frac{\boldsymbol{GB}}{|\boldsymbol{GB}|} = \frac{\hat{i}(x_B - x_G) + \hat{j}(y_B - y_G) + \hat{k}(z_B - z_G)}{|\boldsymbol{GB}|}$$

$$\frac{x_B - x_G}{|\boldsymbol{GB}|} = \frac{x_B}{r}\ ,\ \frac{y_B - x_G}{|\boldsymbol{GB}|} = \frac{y_B}{r}\ ,\ \frac{z_B - z_G}{|\boldsymbol{GB}|} = \frac{z_B}{r}$$

we get $rx_B - rx_G = x_B|\boldsymbol{GB}| \implies x_B(r - |\boldsymbol{GB}|) = rx_G$, but $r = |\boldsymbol{OG}| + |\boldsymbol{GB}| \implies r - |\boldsymbol{GB}| = |\boldsymbol{OG}| = \sqrt{{x_G}^2 + {y_G}^2 + {z_G}^2} = distance$

$$x_B = \frac{rx_G}{distance},\quad y_B = \frac{ry_G}{distance},\quad z_B = \frac{rz_G}{distance}$$

3.1.3 Computation of the fluid forces

Conventionally, forces exerted by the flow on a body are calculated on its surface. In GCIBM we use non-body conformal cartesian grid, so it becomes tedious to calculate the forces on the surface of the body. A more convenient way is to calculate the forces using the change in momentum principle. If a control volume shown in Fig. 3.2 having volume V and surface area S encloses the body, then force in the i-th direction using the momentum balance principle is

$$F_i = \int_V \frac{\partial(\rho u_i)}{\partial t} dV + \int_S \rho u_i(\boldsymbol{u}\ .\ \hat{\boldsymbol{n}}\ dS) + \int_S p(\hat{\boldsymbol{n}}_{\boldsymbol{i}}\ .\ \hat{\boldsymbol{n}}\ dS) + \int_V \rho a_i dV$$

$\hat{\boldsymbol{n}}$ and $\hat{\boldsymbol{n}}_{\boldsymbol{i}}$ are unit vectors along the surface normal of the chosen control volume and i-th direction, respectively. The corresponding non-dimensional force

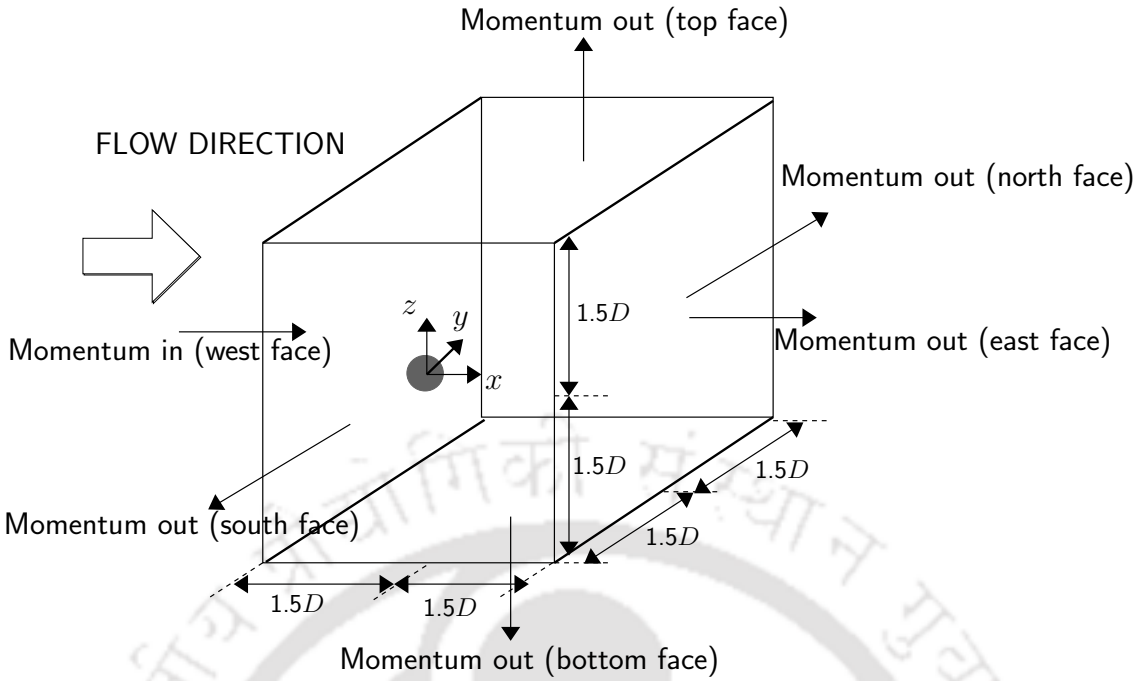

Figure 3.2: Cubical control volume for calculating the force coefficients

coefficients are

$$C_i = \frac{F_i}{\frac{1}{2}\rho U^2 A}$$

where A is the plan or projected area of the body, $A = \frac{\pi}{4}D^2$ for a sphere.

3.1.4 Domain size and Grid spacing

Numerical simulations of physical phenomena replace continuous (infinite) space by discrete (finite) one. This must retain the overall physics of the phenomena to an acceptable tolerance level for true realization. There are two criteria which must be satisfied before using the numerical data to analyse the flow. These two criteria are adequate size of domain and grid spacing.

Domain size

It is well known that solutions from numerical experiments depend substantially on the computational domain and mesh used, especially at high instability regimes of the flow. The computational domain is composed of many boundaries in the stream-wise (inlet/outlet), transverse (far fields) and vertical (sides) directions.

These boundaries must be located at enough distances so that artificial effects do not introduce significantly large errors.

Grid spacing

Grid spacing is the most obvious source of error in numerical simulations. It not only dictates the replacement of infinite space by finite, but also the discretization or truncation error inherent with the governing equations. Theoretically, the grid spacing must be extremely low, but no computer can handle infinite number of points practically.

For maintaining same grid spacing throughout the domain, large number of grid points are required, thereby putting heavy burden on computer memory and space. Use of non-uniform grid, simultaneously nullifies the domain size effects and provide steep velocity gradients near the solid surface.

3.1.5 Domain independence study

Based on the earlier studies for stationary [18, 21] and VIV [23, 24] of a sphere, inlet, outlet and the side boundaries are kept at $5D$, $25D$ and $8D$ distances from the center of the sphere, respectively. These extents are reported [18, 21, 23, 24] to assure domain independent solution and increasing them further only leads to negligible difference in flow solution.

3.1.6 Mesh independence study

First column in Table 3.1 shows four grid levels (M1, M2, M3 and M4) used to determine grid dependency of the solution for uniform flow past a transversely oscillating sphere. Other simulations parameters for these four meshes are Reynolds number $Re = 300$, normalized amplitude $A = 0.5$, frequency ratio $f_R = 1.3$ and time increment $\Delta t = 0.004$. Mesh size is progressively refined from M1 to M4, measured by minimum grid spacing (Δ) in second column of Table 3.1.

Figure 3.3 shows qualitative similarity in time evolution of the coefficients of

Mesh	Δ	$< C_D >$	C'_D	C'_L	$C_{L_{max}}$	St
$172 \times 136 \times 136$ (M1)	40%	-0.20%	5.2%	-2.1%	-3.5%	0%
$193 \times 157 \times 157$ (M2)	20%	0.10%	2.9%	-2.4%	-3.4%	0%
$217 \times 181 \times 181$ (M3)	0.020	0.978	0.134	0.379	0.566	0.178
$241 \times 205 \times 205$ (M4)	-15%	0%	-1.5%	1.6%	1.9%	0%

Table 3.1: Comparison of global flow parameters at different mesh sizes

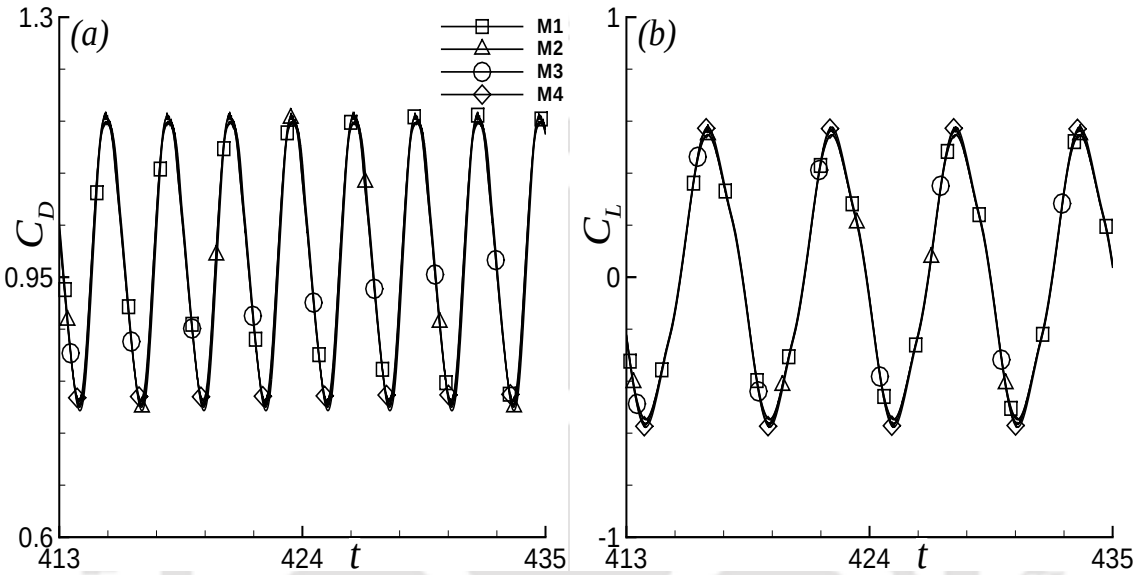

Figure 3.3: Comparison of signals for different grid sizes

drag (C_D) and lift (C_L) on four meshes (in the statistically stationary state). Quantitative assessments of the grid levels are made through the following global flow parameters: average coefficient of drag ($< C_D >$), rms values of drag and lift (C'_D and C'_L), maximum lift ($C_{L_{max}}$) and Strouhal number (St). Values of these parameters at M3 and percentage change relative to M3 on other meshes are listed in the table. The changes observed in Table 3.1 show refinement beyond M3 does not yield a better solution considering the increase in cost.

All the simulations hereafter are carried out on $217 \times 181 \times 181$ (M3) as this grid resolution proved adequate for the solutions to be grid-insensitive and thus it is suitable combination of accuracy and cost involved. Figure 3.4 shows the planar and three-dimensional views of the computational grid at M3. The edges of each processor and the boundary of the computational domain is shown with bold lines

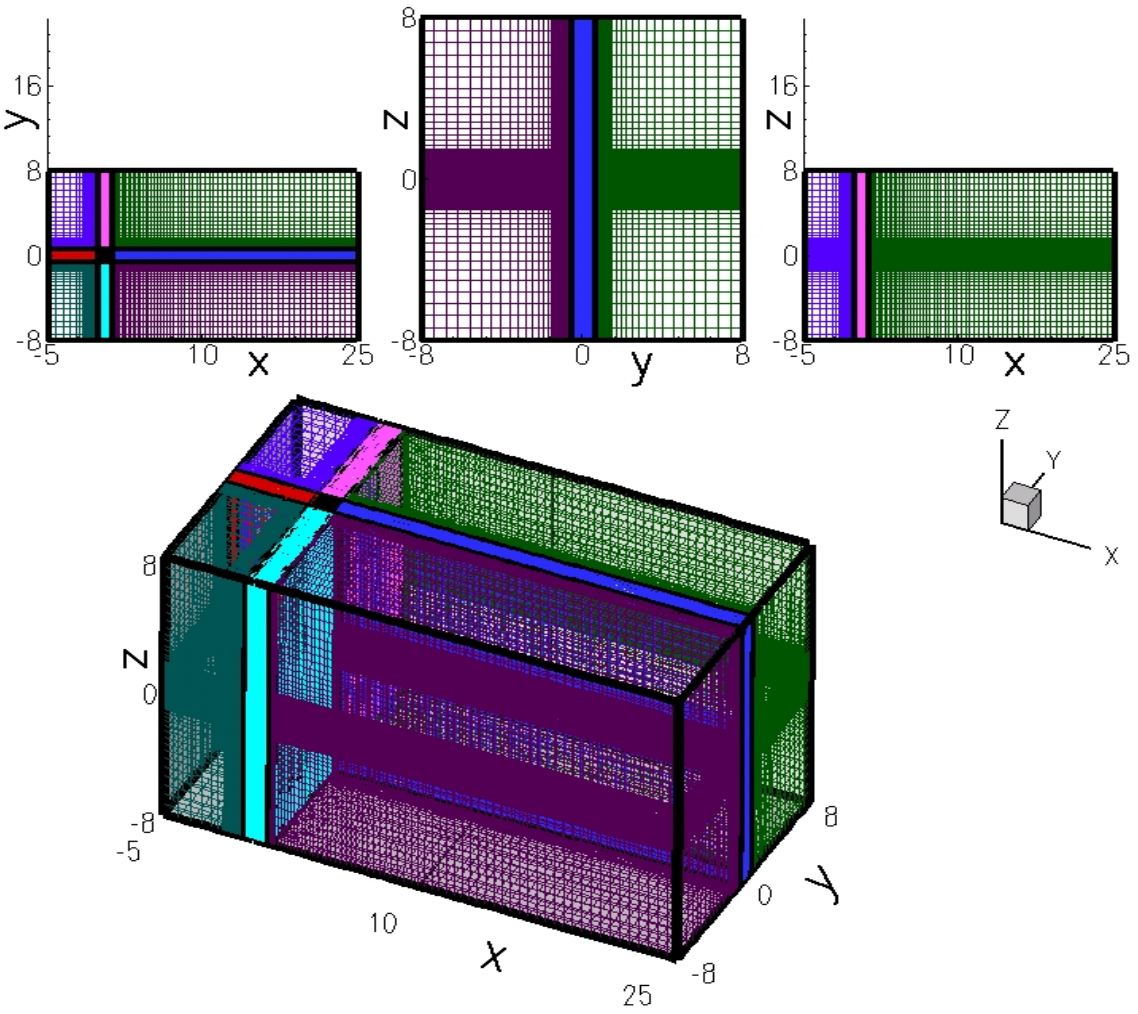

Figure 3.4: Planar and three-dimensional views of the grid

with different colours used to mark different processors. These views clearly show the extent of the computational domain and non-uniform grid distribution.

3.1.7 Steady axisymmetric flow, $Re = 100$

The coefficient of lateral force (C_L) and coefficient of side-wise force (C_S) are asymptotically zero. The coefficient of drag ($C_D = 1.085$) is in good agreement to the reported [18] value of 1.080. The wake structure [58] using $Q = 0.001$, (see Fig. 3.5 top row) reveals the axisymmetric vortex-ring at $Re = 100$. The z-component of vorticity shown in Fig. 3.6 agrees well with the reported [18] trend, and is similar to the steady near wake of a circular cylinder at subcritical Reynolds numbers.

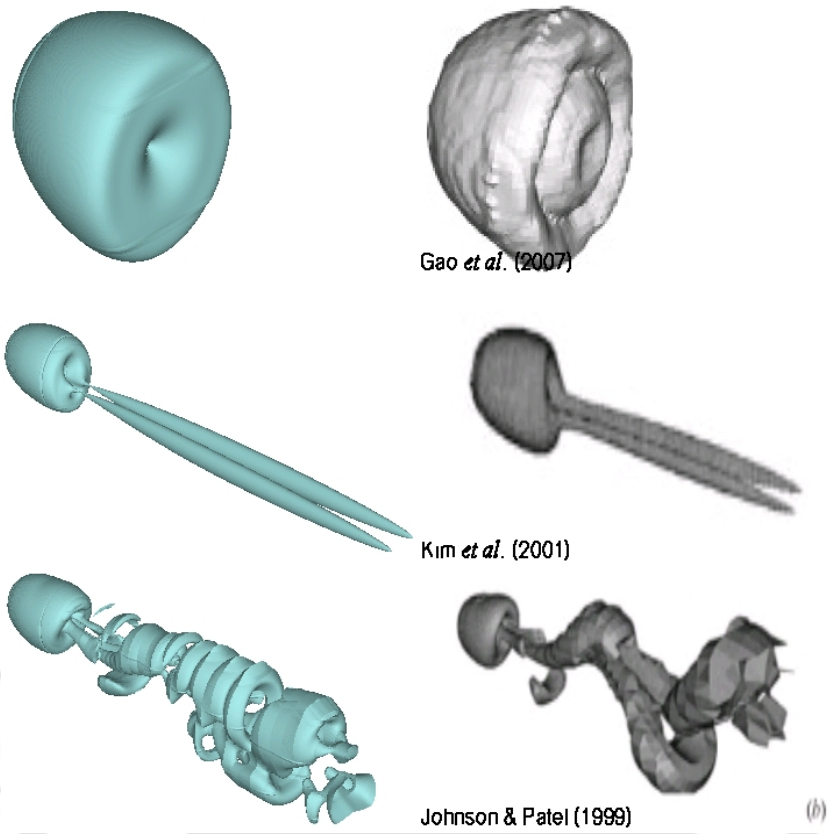

Figure 3.5: Comparison of computed wake structures with reported results for flow past a sphere at $Re = 100,\ 250$ and 300

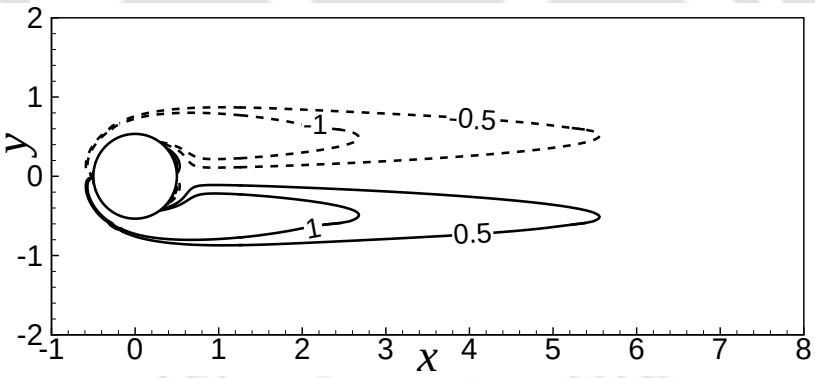

Figure 3.6: Vorticity contour (z-component) for flow past a sphere at $Re = 100$

3.1.8 Steady planar symmetric flow, $Re = 250$

The wake remains steady with $C_D = 0.702$, in agreement to the reported [18] value of 0.700. The non-zero $C_L = -0.066$, compared to -0.062 reported by Johnson & Patel [18], signifies the loss of axial symmetry. Instead the flow admits a planar symmetry (x, y)-plane at $z = 0$, which is supported by zero C_S. The wake structure (see Fig. 3.5 middle row) demonstrates the trail of two counter rotating

vortices, which in literature is called a double-threaded wake. At this Re the flow acquires three dimensionality, which is evident by the three components of vorticity (see Fig. 3.7) in agreement with the reported results [18]. Stream wise vorticity

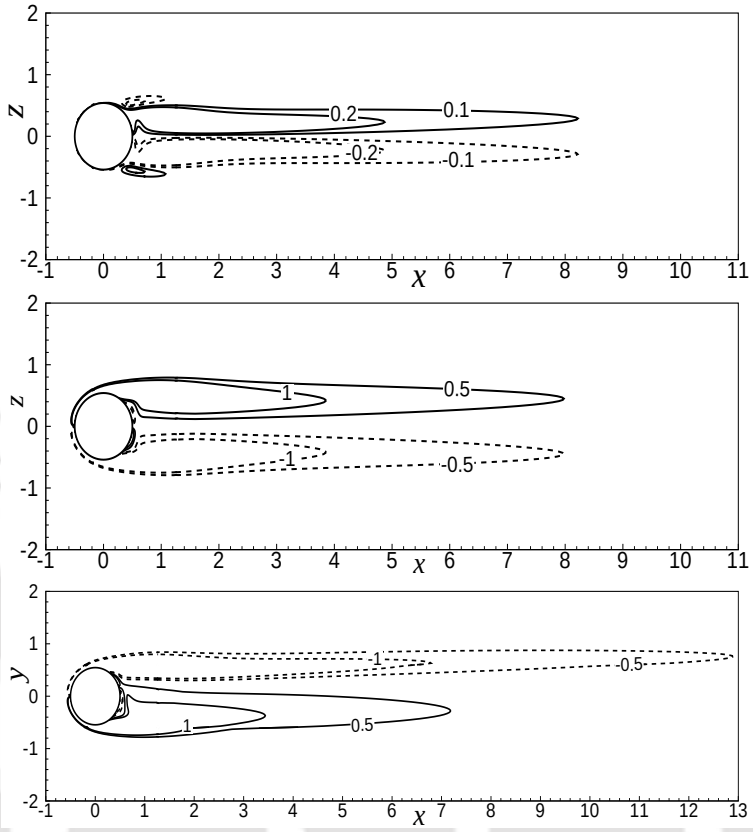

Figure 3.7: Vorticity contours for flow past a sphere at $Re = 250$

(w_x) contours in (Fig. 3.7 top row) reveals an antisymmetric distribution about the symmetry plane. As the flow has a planar symmetry; the lateral vorticity (w_y) in (Fig. 3.7 middle row) is symmetric, while the side-wise vorticity (w_z) appears to be shifted towards positive-y in (Fig. 3.7 bottom row).

3.1.9 Unsteady planar symmetric flow, $Re = 300$

At $Re = 300$ the periodic signals of C_D and C_L indicates flapping of the wake, which is seen at a much lower Reynolds number for a circular cylinder wake. However, the zero coefficient of side-wise force results from the prevailing planar symmetry observed at $Re = 250$. The wake structure (see Fig. 3.5 bottom row) consists of hairpin like inter-connected vortex loops. Table 3.2 compares the

Work	$< C_D >$	$< C_L >$	St
Present	0.659	-0.069	0.137
Johnson & Patel [18]	0.656	-0.069	0.137
Kim *et al.* [37]	0.657	0.067	0.134

Table 3.2: Comparison of computed global flow parameters for flow past a stationary sphere at $Re = 300$ with reported results

global flow parameters: average coefficient of drag ($< C_D >$), average coefficient of lateral force ($< C_L >$) and Strouhal number (St) with the literature. Figure 3.8

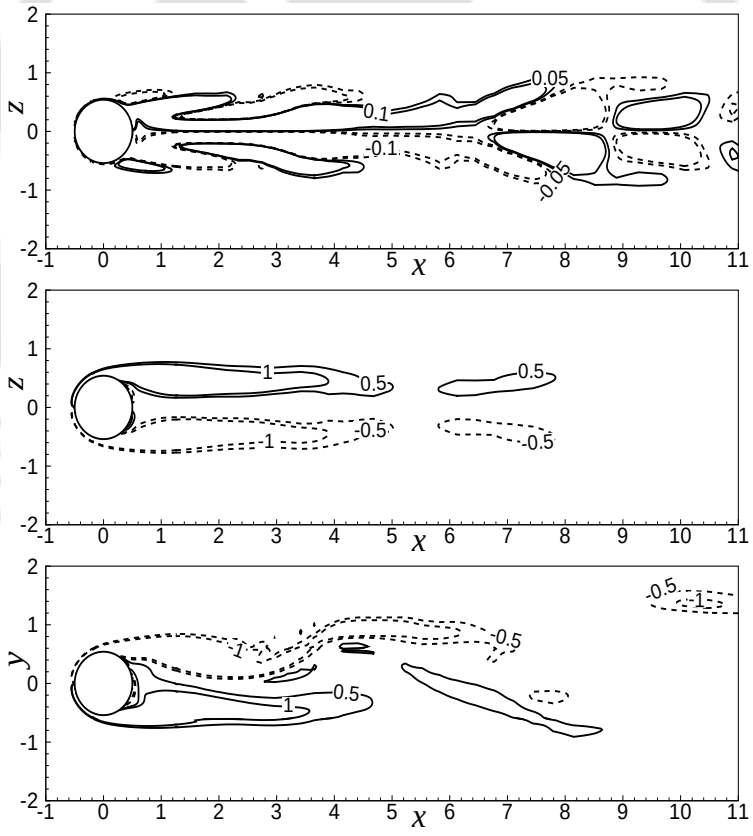

Figure 3.8: Vorticity contours for flow past a sphere at $Re = 300$

shows the instantaneous vorticity contours at three different planes, which agree well with the reported results [18].

3.1.10 Convergence behavior of different linear solvers

Convergence behavior of different linear solvers are compared as fast and monotonic decay of the error is essential in cases where the computations are initiated with a flow which is otherwise stationary. All the parallel cases are computed with 16 processors and iteration is terminated at an error level of 10^{-6}. The identical maps of the sequential and parallel solvers in Fig. 3.9 indicate absence of

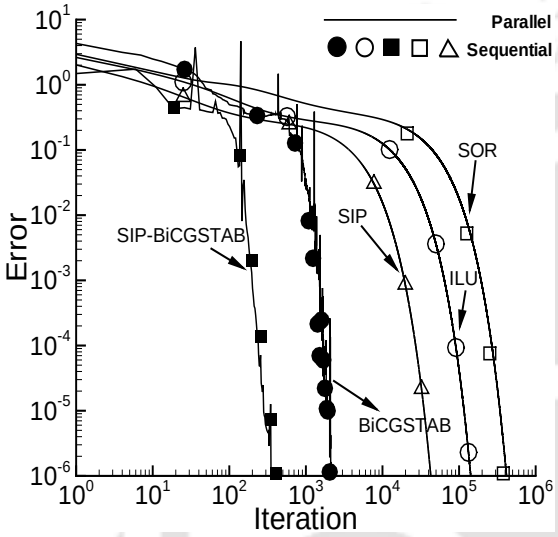

Figure 3.9: Convergence behavior of the linear solvers

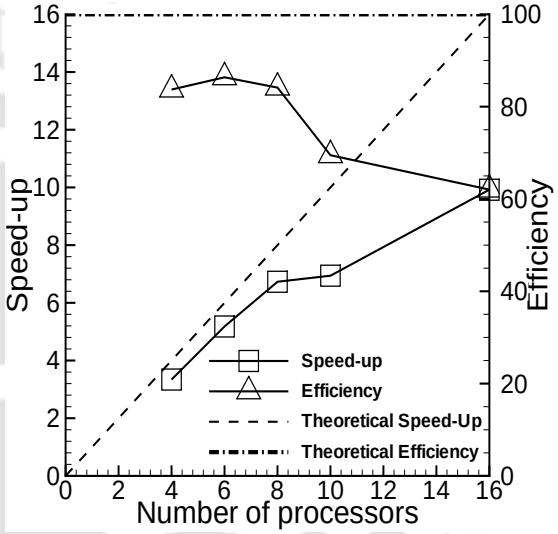

Figure 3.10: Performance of the parallel solver with processors

any possible excursion in error owing to inter-processor communications. The effect of the preconditioner in removing the spurious oscillation observed in the BiCGSTAB solver should be noted. The iteration numbers shown in Table 3.3

Processors	Attribute	SOR	ILU	SIP	BiCGSTAB	SIP-BiCGSTAB
Sequential	Iterations	380651	142041	42758	2105	413
	Time (s)	128951	50476	15198	1416	390
Sixteen	Iterations	416653	142026	42753	2121	351
	Time (s)	25342	14402	4488	243	78

Table 3.3: Comparison of iterations and time taken by different linear solvers

is indicative of only the first time step. It can be noted that iteration counter is amenable to change from sequential to parallel calculations owing to the implementation of procedures such as incomplete LU decomposition. Among all the solvers the preconditioned SIP-BiCGSTAB is found to be the best in terms of number of calculations per iteration and overall decay rate of the error.

3.1.11 Performance of the parallelized method

Performance of the parallel simulations are assessed using speed-up ($S = T_s/T_p$) and efficiency ($\eta = S/p$) where T_s and T_p are the sequential and parallel (with p processors) CPU-times, respectively. Theoretically, S must increase linearly with p at the maximum $\eta = 100\%$. However, owing to the increase in inter-processor communications, S reaches a near-optimum value which can no further be improved while η drops. The comparison of the theoretical and actual S and η is shown in Fig. 3.10 which clearly shows the trend described above.

3.2 Transverse oscillation of a circular cylinder

Den Hartog [9] was the first to report synchronization of the periodic wake behind a transversely oscillating cylinder. Within the synchronization jumps in the phase and amplitude of the lift and drag forces were reported by Bishop & Hassan [10]. Vibration of the cylinder at the upper and lower frequency limits of the synchronized regime causes vortex street to be compressed and expanded [59], respectively. The oscillating cylinder imposes timing and frequency of vortex shedding on the wake in the synchronized regime [11]. Williamson & Roshko [12] suggested that the jumps [10] were associated with the change of vortex shedding Modes namely 2S and 2P.

3.2.1 Computational details

Figure 3.11 shows schematic diagram describing the problem, computational do-

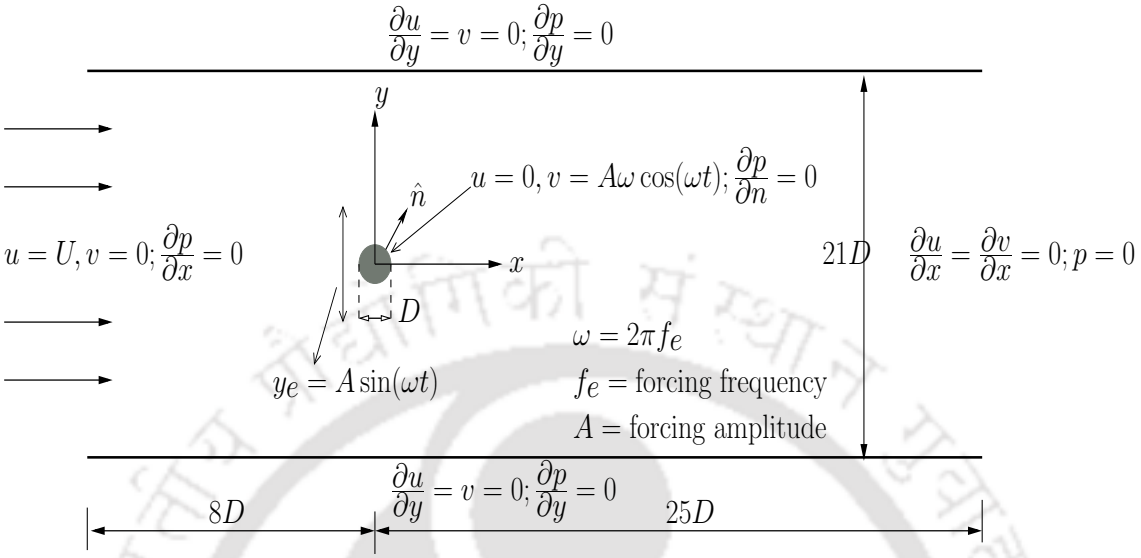

Figure 3.11: Schematic diagram for forced transverse oscillation of a circular cylinder

main and boundary conditions employed. Two-dimensional numerical simulations were carried out on a non-uniform cartesian grid 293×226 in the stream-wise (x) and transverse (y) directions, respectively. A square domain of side 1.2 with grid size 161×161 was used to provide an uniform finer mesh engulfing the cylinder which generated grid resolution $\Delta x = \Delta y = 0.007$ in and around the cylinder. We defined a frequency ratio ($f_R = f_e/f_o$), where f_o is the vortex shedding frequency from the stationary cylinder. If $St_o = f_o D/U$ is the Strouhal number associated with the vortex shedding from a stationary cylinder, then the forced Strouhal number ($St_e = f_e D/U$) can be expressed as $St_e = f_R St_o$; in this study St_o was found out to be 0.201. Computations were performed for non-dimensional amplitude ($A = 0.2$), $Re = 185$ and $0.5 \leq f_R \leq 2.0$ with time increment ($\Delta t = 0.0004$).

3.2.2 Results

Figure 3.12 shows that the time evolution of the coefficient of drag (C_D, upper signals) and coefficient of lift (C_L, lower signals) match well with the reported

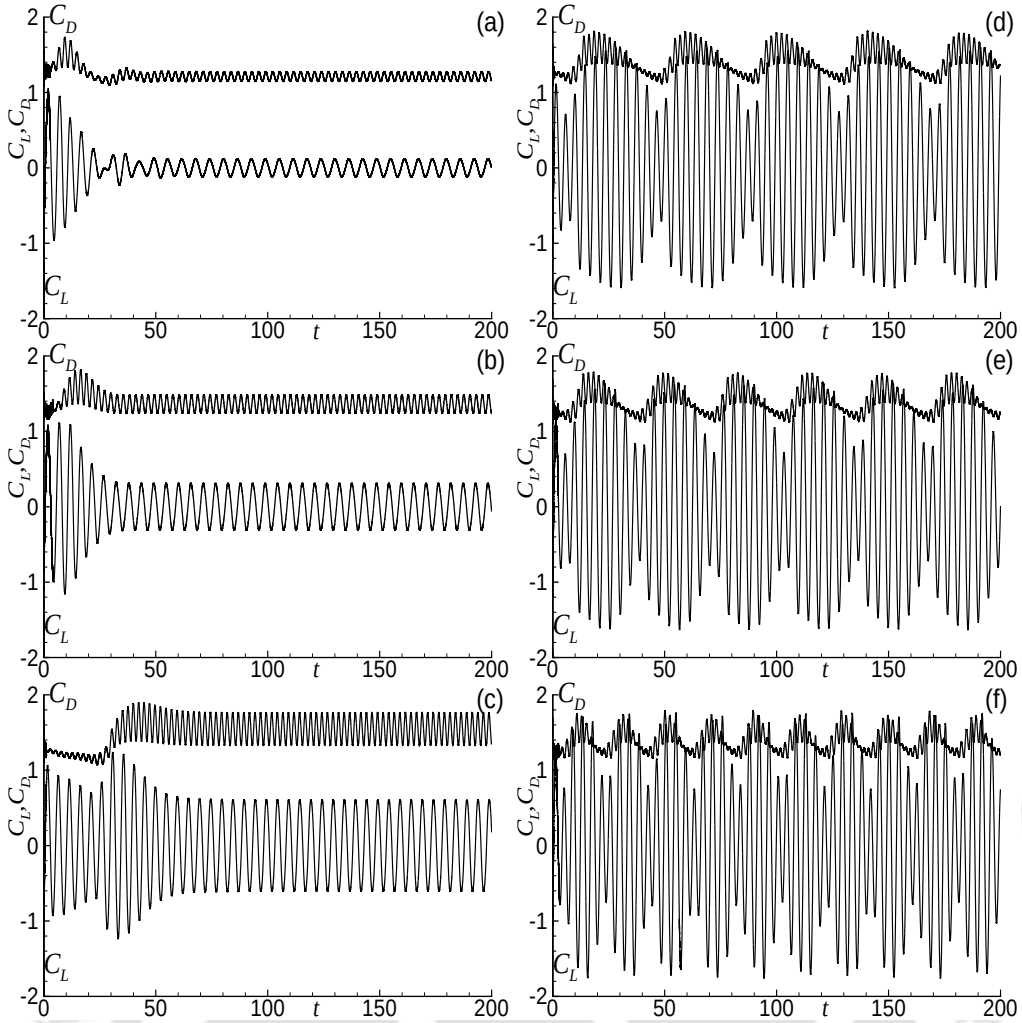

Figure 3.12: Time evolution of the coefficient of drag and lift for forced transverse oscillation of a circular cylinder (a) $f_R = 0.8$, (b) $f_R = 0.9$, (c) $f_R = 1.0$, (d) $f_R = 1.1$, (e) $f_R = 1.12$, (f) $f_R = 1.2$

[60] results. The signals for $f_R = 0.8$, 0.9 and 1.0 are purely sinusoidal, while the signals for $f_R = 1.1$, 1.12 and 1.2 are complex wave-forms. The complex wave-forms reflect [10] the existence of two frequencies: 1) the natural vortex shedding frequency (f_o) of a stationary circular cylinder and 2) the forcing frequency (f_e). Purely sinusoidal signals are consequence of the lock-in state of the wake ($0.8 \leq f_R \leq 1.0$), where the ratio of the forcing frequency to the vortex shedding frequency is unity. Outside the lock-in regime the dominant vortex shedding frequency (f_s) varies almost linearly with f_R (see Fig. 3.13). The global parameters: (i) average coefficient of drag ($\overline{C}_D$), (ii) root mean square (rms) value of the coefficient of lift (C_{Lrms}) and (iii) rms value of the coefficient of drag (C_{Drms})

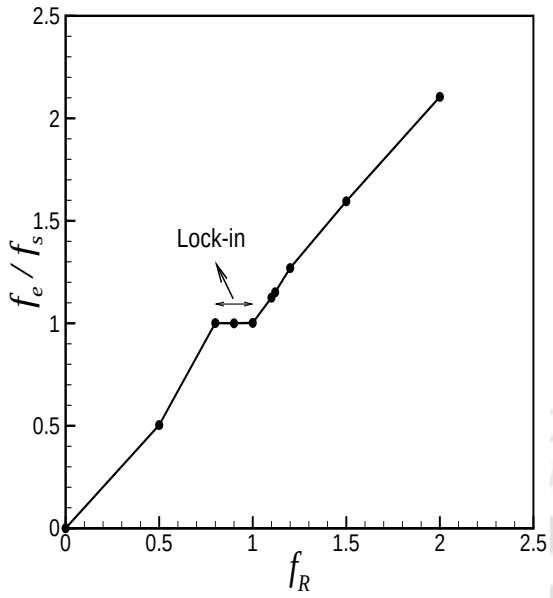

Figure 3.13: Ratio of the forcing and the vortex shedding frequency as a function of f_R for forced transverse oscillation of a circular cylinder

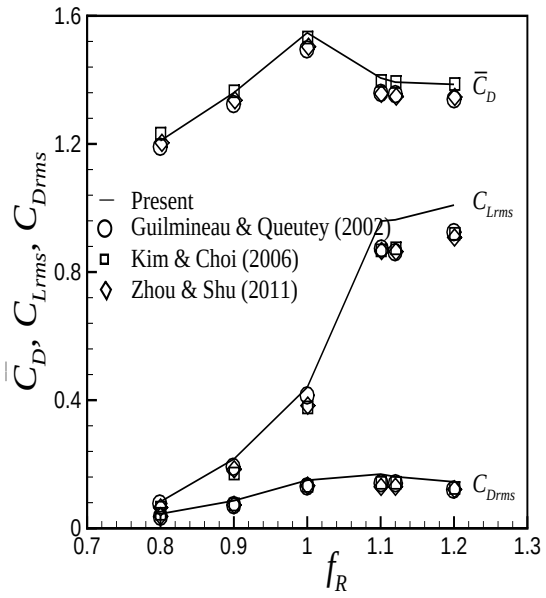

Figure 3.14: Comparison of computed global flow parameters for forced transverse oscillation of a circular cylinder with reported results

shown in Fig. 3.14 are in good agreement with the reported results of Kim & Choi [46], Guilmineau & Queutey [60], Zhou & Shu [61].

3.3 Uniform flow past a rotating circular cylinder

The rotation of a circular cylinder in a uniform flow is expected to reduce the flow-induced oscillations [62]. In addition to $Re = UD/\nu$ the other parameter that influence the flow is non-dimensional rotation rate ($\alpha = D\omega/2U$), where ω represents the angular velocity of the cylinder about its axis. Kang *et al.* [62] found that the vortex shedding is completely suppressed beyond a critical non-dimensional rotational speed (α_L), which increases logarithmically with Re. In a narrow range, $4.8 < \alpha < 5.15$ at $Re = 100$ [63] interestingly found again an unsteady behavior in the flow field with large amplitudes in the fluctuation of the drag and lift forces. At $Re = 200$ and $4.34 \leq \alpha \leq 4.7$ a reappearance of unsteady wake was reported by Mittal & Kumar [64] which was later experimentally confirmed by Kumar *et al.* [65].

3.3.1 Computational details

All the computational features employed were same as that of the previous section. Two-dimensional simulations were performed at $Re = 200$ and ($0 \leq \alpha \leq 2.5$) in steps of 0.5.

3.3.2 Results

Figure 3.15(a) shows that $\overline{C}_D$ decreases while C_{Drms} increases up to $\alpha \leq 1.5$ for

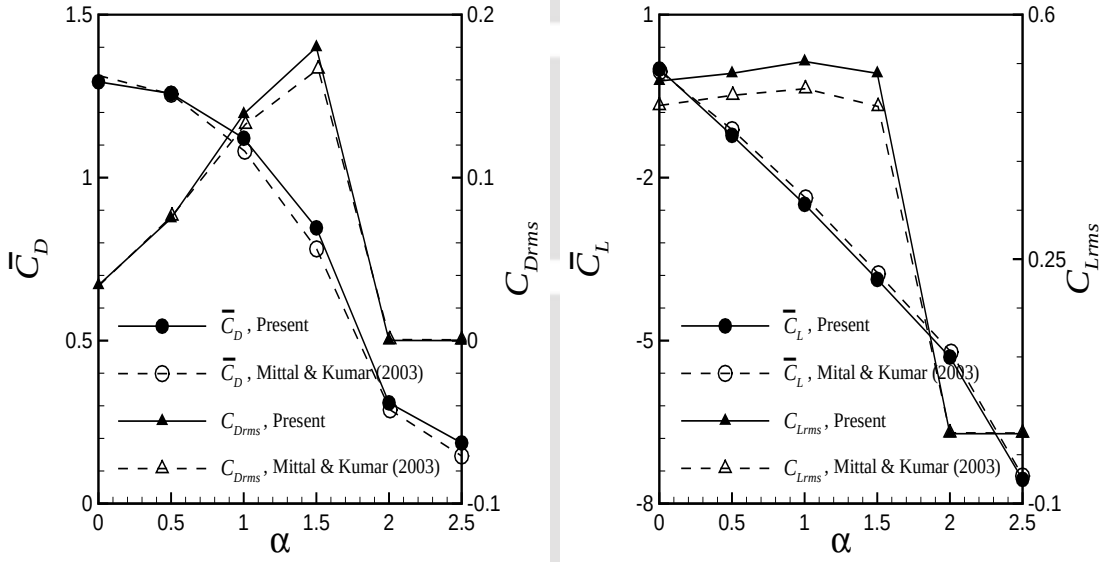

(a) Drag (b) Lift

Figure 3.15: Comparison of the average and rms values of the drag and lift coefficient for rotating circular cylinder with reported results

which the vortex shedding is observed. Figure 3.15(b) shows that $\overline{C}_L$ increases while C_{Lrms} is nearly constant for $\alpha \leq 1.5$. In agreement to Mittal & Kumar [64] our results show no vortex shedding for $\alpha = 2$ and 2.5, which is supported by zero C_{Drms} and C_{Lrms}. Moreover, $|\overline{C}_L|$ continuously increases with α because of the Magnus effect.

Chapter 4

Uniform flow past a transversely oscillating sphere

The effect of forced transverse oscillation of a sphere on the resulting wake is studied in details. This chapter reports the results thus obtained and based on the observations made instability modes of the wake are revealed in the light of VIV of the sphere. The sphere is oscillated by a range of forcing frequencies at fixed amplitude and Reynolds number.

4.1 Introduction

Dynamics of tethered objects in a flow is practically relevant to: tethered bodies like marine buoys, underwater mines, tethered balloons in the atmosphere and towed objects behind ships. Williamson & Govardhan [48] were the first to observe the dynamics of tethered spheres in a steady fluid flow. Vibration in the transverse direction were more vigorous (saturation amplitude of close to two diameters peak-to-peak) compared with that in the stream-wise direction. The frequency of oscillation in the stream-wise direction was twice the transverse oscillation frequency. The reduced velocity ($U^* = U/f_n D$) instead of the Reynolds number (Re), where U, f_n and D are the free-stream velocity, natural frequency of the system and the diameter of the sphere, respectively was found as a more

suitable parameter to scale the response amplitudes.

Embarking upon these observations Govardhan & Williamson [66] characterized the transverse oscillations by the root-mean-square (rms) of the sphere's displacement instead of the amplitude. The rms response curve displayed a local peak followed by a saturation value. The local peak was explained as a resonance between the vortex shedding frequency from a stationary sphere (f_o) and f_n. Jauvtis *et al.* [67] named these resonance condition and the saturation state as Modes I and II, respectively. They extended the works to higher mass ratio ($m^* =$ sphere mass/ displaced mass of fluid) and U^* feasible in wind tunnel instead of water channel. A new periodic response for ($20 \leq U^* \leq 40$) at $m^* = 80$ was named as Mode III. They also discovered Mode IV response characterized by intermittent bursts of large-amplitude vibration beyond $U^* = 100$.

All the researches, so far were focused on the dynamics of sphere without associating the vortex dynamics in the wake. Govardhan & Williamson [68] hereafter referred to as G-W were the first to report a chain of stream-wise vortex loops on alternating sides of the wake for the first three periodic responses. Modes I and II represented the synchronized regime, where the sphere's oscillation and the wake vortex shedding frequencies were synchronized (or tuned) to each other. Oscillations of the sphere in the vertical direction (z) were found to be less than 5% of that in the transverse direction (y). Response for a tethered sphere (xy motion) and hydroelastic sphere (y-only) compared well for similar mass-damping parameter $(m^* + C_A)\zeta$, where C_A is the potential added mass coefficient and ζ is the damping ratio.

Hout *et al.* [69] discovered three bifurcation regions for a tethered sphere. In the first region, vortex shedding pattern was identical to that of a stationary sphere with no transverse oscillation. The second region was characterized by periodic and large amplitude transverse oscillation of half the sphere diameter. The vortex shedding and the wake structure were similar to that observed by G-W in the second region. For the third region, the sphere exhibited non-stationary

oscillations in the transverse direction. Second bifurcation region overlapped with the Modes I and II, while the third bifurcation region was linked to Mode IV.

Numerical investigation of Behara *et al.* [23] at $Re = 300$ observed shedding of spiral vortices in addition to the hairpin vortices reported in G-W. Eshbal *et al.* [70] observed an increase of fragmented vortical structures as Re increased from 550 to 1925. This increase of fragmented vortical structures was attributed to the increase in shear layer instabilities. Numerical and experimental study by Lee *et al.* [24] showed the existence of seven different flow regimes for 50$\leq$ Re $\lesssim$1200. These regimes do not have any relation with the four modes previously reported. Entirely different observations are attributed to the use of neutrally buoyant tethered sphere instead of the light and heavy spheres. An interesting observation was made by Williamson & Govardhan [48] and G-W that the flow remains same in the range $2000 \leq Re \leq 12000$.

The aim of this work is to identify and study the wake instability modes for forced transverse oscillation of a sphere at $Re = 300$. In the following sections we shall establish a correlation between the modes revealed and those found in VIV of a sphere. The energy transferred from the fluid to the sphere is found to be negative which is explained by revealing two mechanisms of forcing in section 4.3.2. In the next section the governing equations are followed by a brief discussion on the numerical technique employed. In section 4.3 three wake instability modes are analyzed based on time traces of force coefficients, phases and energy transfer rates. Vortex shedding modes, instantaneous wake structures are shown and discussed in section 4.4 in order to characterize the near wake region. Finally the principal findings of the present work are summarized in section 4.5.

4.2 Problem set-up

A sphere of diameter D oscillates transversely (y) in a stream-wise (x) uniform incompressible flow (U). Figure 4.1 shows the computational domain and boundary

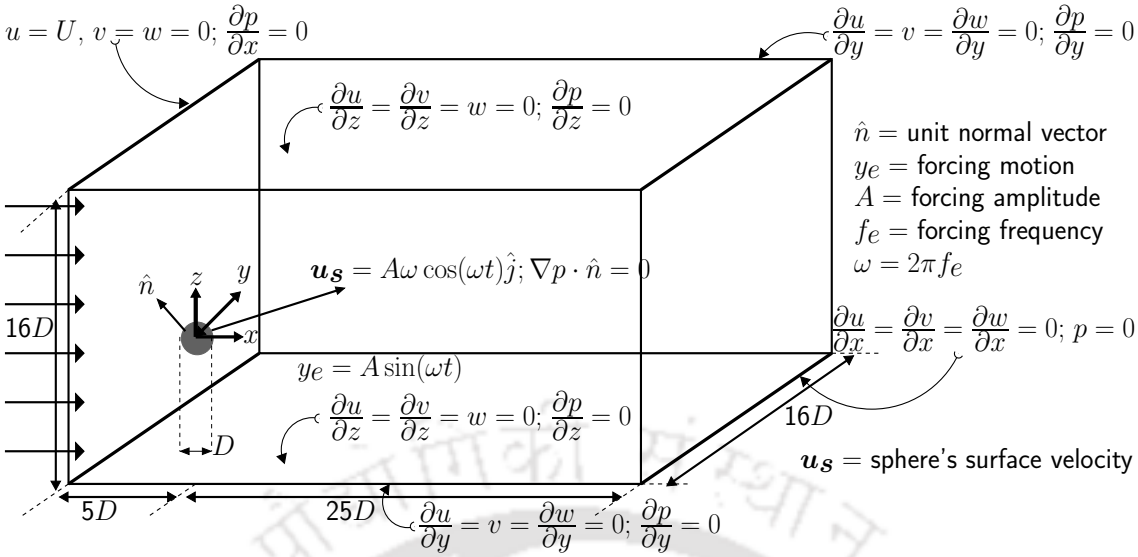

Figure 4.1: Schematic diagram for the forced transverse oscillation of a sphere

conditions in the inertial frame of reference. Equations (2.7) and (2.8) govern the above problem, where normalized acceleration of the non-inertial frame fixed to the oscillating sphere is $A_i = -4(\pi St_e)^2 A\sin(2\pi St_e t)\delta_{iy}$. Here A and $St_e = f_e D/U$ represent the normalized amplitude and the forcing Strouhal number. For a stationary sphere if the vortex shedding frequency (f_o) and the associated Strouhal number ($St_o = f_o D/U$) are known, then the forcing Strouhal number can be expressed as $St_e = f_R St_o$ by prescribing a frequency ratio ($f_R = f_e/f_o$).

4.2.1 Computational details

A highly non-uniform Cartesian grid $217 \times 181 \times 181$ (approximately seven million computing cells) is used for the calculations, within which the sphere is bounded by a cube of side $3D$ having uniform grid spacing of $0.02D$. Normalized transverse oscillation of the sphere ($y_s = A\sin(2\pi St_e t)$) is prescribed with an amplitude $A = 0.5$ and frequency ratio $0.16 \leq f_R \leq 1.3$. Simulations are carried out for $Re = 300$ at which $St_o = 0.137$ is computed. The second-order semi-implicit time marching algorithm uses a time increment $\Delta t = 0.01, 0.005$ and 0.004 for the f_R ranges $\{0.16, 0.2\}$, $\{0.45, 0.5\}$ and $[0.8, 1.3]$, respectively. Average Courant numbers achieved at $f_R = 0.2$ and $f_R = 1.3$ are 0.346 and 0.139, respectively.

4.3 Time evolution of force coefficients

Extensive analyses were performed on time evolution of coefficients of drag (C_D), lift (C_L) and vertical force (C_H) along the stream-wise (x), transverse (y) and vertical (z) directions, respectively.

4.3.1 Wake synchronization regime and Mode III

Synchronization or “lock-in" is a state where the structure oscillates with the same frequency (f_e) as the wake (f_s), obtained by carrying out DFT of the C_L signals. Figure 4.2(a) depicts synchronization ($f_e/f_s = 1$) in the range $0.45 \leq f_R \leq 1.3$

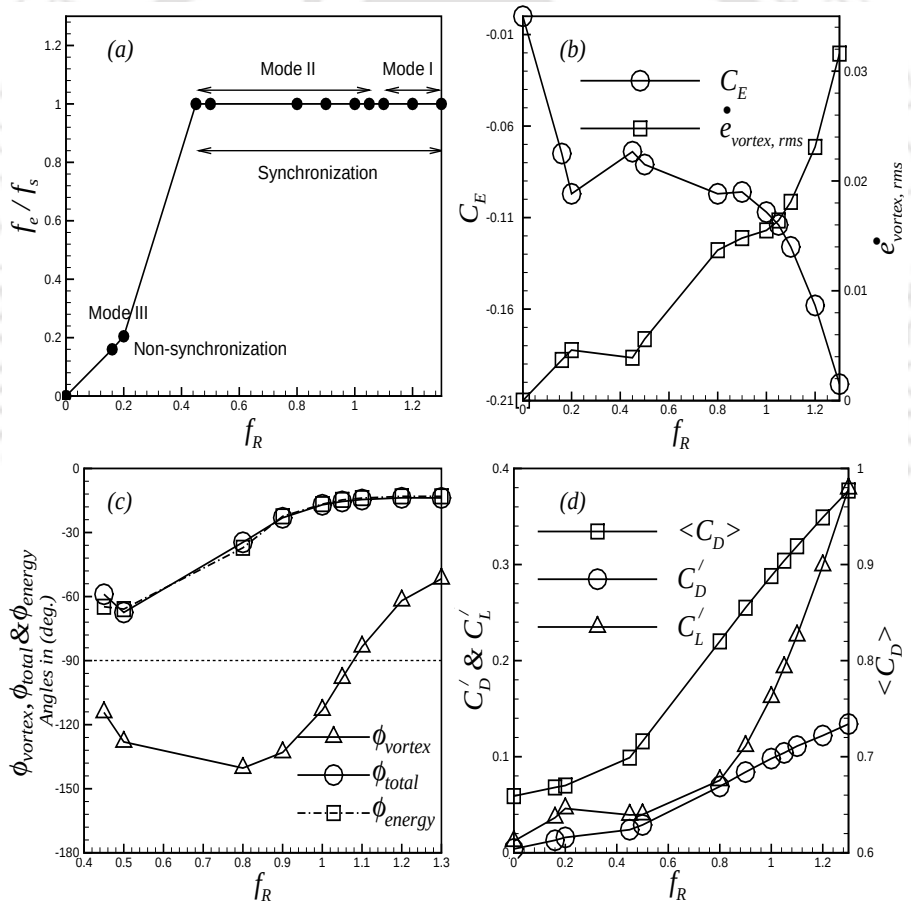

Figure 4.2: (a) Ratio of the sphere oscillation to the vortex shedding frequency, (b) Coefficient of energy and rms of the vortex energy (c) Vortex and total phase and (d) Global parameters as functions of f_R

and departure from it at $f_R = 0.16, 0.2$. Non-synchronization (wake and structure loosely connected) is attributed to the existence of both the forcing and natural

shedding frequencies of the stationary structure; also reported by Bishop & Hassan [10] for the forced transverse oscillation of a circular cylinder. Synchronization and non-synchronization were associated with Modes I,II and III, respectively in VIV of a sphere by G-W. Jauvtis *et al.* [67] observed that the wake oscillates 3 to 8 times faster than the sphere in Mode III, in analogy to which $f_s/f_e = 6.25$ and 5 at $f_R = 0.16$ and 0.2 in the present study suggest occurrences of similar instabilities in the wake for forced oscillation as that of VIV.

4.3.2 Energy transfer and decomposition of transverse force

Energy transfer (E) in fluid-structure interaction systems is defined as work done by the fluid force (F_x, F_y, F_z) to displace (x, y, z) the structure over an oscillation cycle (T) i.e., $E = \int_0^T (F_x\dot{x} + F_y\dot{y} + F_z\dot{z})dt$. Normalized energy transfer is called the coefficient of energy given by

$$C_E = \frac{E}{\frac{1}{2}\rho U^2 \pi \frac{D^2}{4} D} = \int_0^T \left(\frac{F_y}{\frac{1}{2}\rho U^2 \pi \frac{D^2}{4}} \right) \frac{\dot{y}dt}{D} = \int_0^T C_L \dot{y}^* dt^* \tag{4.1}$$

If sinusoidal functions are used to approximate the motion $y = A_o \sin(\omega t)$ and transverse fluid force $F_y = F_o \sin(\omega t + \phi)$ in the synchronization regime, where ϕ is the phase difference between y and F_y then upon simplification $E = \pi A_o F_o \sin\phi$, and thereby

$$C_E = \pi \left(\frac{A_o}{D} \right) \left(\frac{F_o}{\frac{1}{2}\rho U^2 \pi \frac{D^2}{4}} \right) \sin\phi = \pi A^* C_{Lo} \sin\phi \tag{4.2}$$

where C_{Lo} is the amplitude of the lift signal.

VIV or free vibration is defined at $C_E > 0$ requiring $0^\circ < \phi < 180^\circ$ according to Eq. (4.2). Carberry *et al.* [71], Leontini *et al.* [72], Baranyi & Daroczy [73] reported $C_E \leq 0$ in addition to $C_E > 0$ for the forced oscillation of a circular cylinder. We reveal two forcing mechanisms to explain the change in sign of C_E. The fluid force tries to displace the sphere by a force F_F. The external forcing mechanism applies a force F_E on the fluid through the sphere to maintain its oscillation, and

as a reaction fluid applies a force $-F_E$ on the sphere. It is easy to see that the sign of C_E is determined by the dominant mechanism of force exerted by the fluid.

A decomposition of the transverse force (C_L) into a potential ($C_{potential}$) and a vortex (C_{vortex}) force is in practice [3, 15, 17, 68] based on the concept of added mass. It is helpful to recognize the mechanisms of the forces $C_{vortex} = C_L - C_{potential}$ and $C_{potential} = (8/3)(\pi St_e)^2 A^* \sin(2\pi St_e t^*)$ as F_F and F_E, respectively.

Total phase (ϕ_{total}) and vortex phase (ϕ_{vortex}) which are angles between C_{total} and C_{vortex} with the displacement of the sphere (y_s), respectively are analyzed to characterize the Modes I and II. We have also computed the normalized rate of energy transfer (or 'power in'), $\dot{e}_{vortex} = C_{vortex}\dot{y}_s$ as defined by G-W.

4.3.3 Synchronized Modes I and II

Negative C_E in Fig. 4.2(b) indicates greater inertia of the sphere than the fluid ($C_{vortex} < C_{potential}$) at a relatively low Re. Signals of y_s lead C_{total} and C_{vortex} resulting in negative ϕ_{total} and ϕ_{vortex} for all the cases which is in agreement with $C_E < 0$. A transition of $|\phi_{vortex}|$ through 90° seen in Fig. 4.2(c) identifies Modes I and II for $1.1 \leq f_R \leq 1.3$ and $0.45 \leq f_R \leq 1.05$, respectively, as suggested by G-W. We found $|\phi_{vortex}| = 51.6^\circ, 140.3^\circ$ at $f_R = 1.3, 0.8$ to be in close agreement with G-W's prediction of $\phi_{vortex} \approx 50^\circ$ and 140° for Modes I and II, respectively. If the numerical (Eq. (4.1)) and the analytical (Eq. (4.2)) expressions for C_E are equated we get ϕ. To distinguish such obtained ϕ from the values of DFT we simply label it as ϕ_{energy} in Fig. 4.2(c).

The near wake oscillations continue to grow with f_R causing wider low pressure region downstream of the sphere, revealed by increased drag coefficient and rms fluctuations in Fig. 4.2(d). An increase of 100% in the average coefficient of drag ($< C_D >$) was observed by Williamson & Govardhan [48] from that of the stationary sphere values.

Govardhan & Williamson [66] observed a local peak in the normalized rms response of a tethered sphere, which Jauvtis *et al.* [67] termed as Mode I. In case

of a circular cylinder Bishop & Hassan [10] found jumps in phase, lift amplitude and the mean drag coefficient within the synchronization regime which Williamson & Roshko [12] associated with the change of vortex shedding modes. C_E and rms of $\dot{e}_{vortex}$ in Fig. 4.2(b) demonstrate transition from Mode III to Mode II at $f_R = 0.2$, and from Mode II to Mode I at $f_R = 1.05$. Appearance of the VIV modes in forced oscillation is supported by the observation of Leontini *et al.* [72] for forced oscillation of a circular cylinder where wake modes remain same whether $C_E > 0$ or $C_E < 0$.

4.3.4 Characterization of VIV Modes

Phase portraits shown in Figs. 4.3 and 4.4 at $f_R = 1.3$ and 0.8 reveal the state

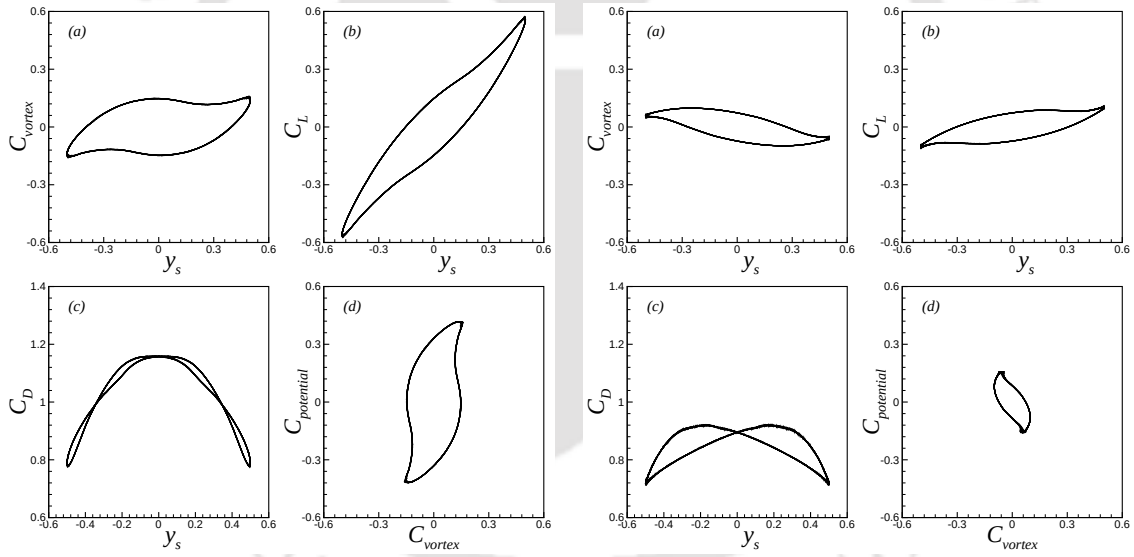

Figure 4.3: Phase-portraits at $f_R = 1.3$

Figure 4.4: Phase-portraits at $f_R = 0.8$

of the wake and its dynamic response to the sphere's oscillation. The maximum amplitudes attained by C_D, C_L and C_{vortex} grow with f_R, which supports the energy transfer by the sphere to the fluid. While the one-lobe closed orbits indicate a periodic synchronized state, two lobes in the $C_D - y_s$ diagram indicates a 2:1 ratio between the stream-wise and transverse oscillations which is analogous to the alternate shedding for a circular cylinder. Williamson & Govardhan [48] explained this ratio as the conditions affecting in-line vibrations were the same at ei-

ther transverse positions of the sphere's displacement. A larger change in ϕ_{vortex} compared to ϕ_{total}, seen in frames (a) and (b) supports the observed Modes I and II as suggested by G-W.

The frequency spectra of C_L in the synchronized regime contains odd harmonics of the fundamental dominant frequency. As the f_R increases the amplitude of these odd harmonics grow. Figure 4.3(c) has two lobes which are slightly twisted in comparison to that in Fig. 4.4(c); an effect of non-linearity enhancement owing to the growth of odd harmonics.

Outside the synchronized regime, the frequency spectra of C_L shows peaks at f_o and all the harmonics of f_e, so the signals are modulated both in frequency and amplitude. Consequently, in Fig. 4.5 (phase portraits at $f_R = 0.2$) the lobes

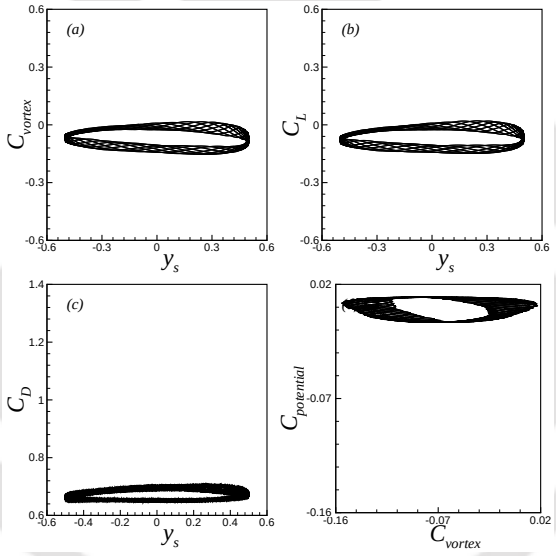

Figure 4.5: Phase-portraits at $f_R = 0.2$

are not easily identifiable as in the synchronized regime. Similar patterns are also observed at $f_R = 0.16$ which suggests a different wake instability mode than Modes I and II.

In Fig. 4.5(d) the width of the pattern is larger than its height implying that the fluid force (C_{vortex}) tends to dominate the external forcing agency ($C_{potential}$) owing to the reduced inertia of the sphere (low f_R). On the other hand, Fig. 4.3(d) shows a reverse order, i.e, height larger than the width of the pattern implying dominance of the external forcing over the fluid force.

4.3.5 VIV Modes and time traces

Time signals at $f_R = 1.3$ and 0.8 for one oscillation cycle of the sphere are shown in Figs. 4.6(a) and 4.6(b) where one complete cycle of C_{total} confirms the synchro-

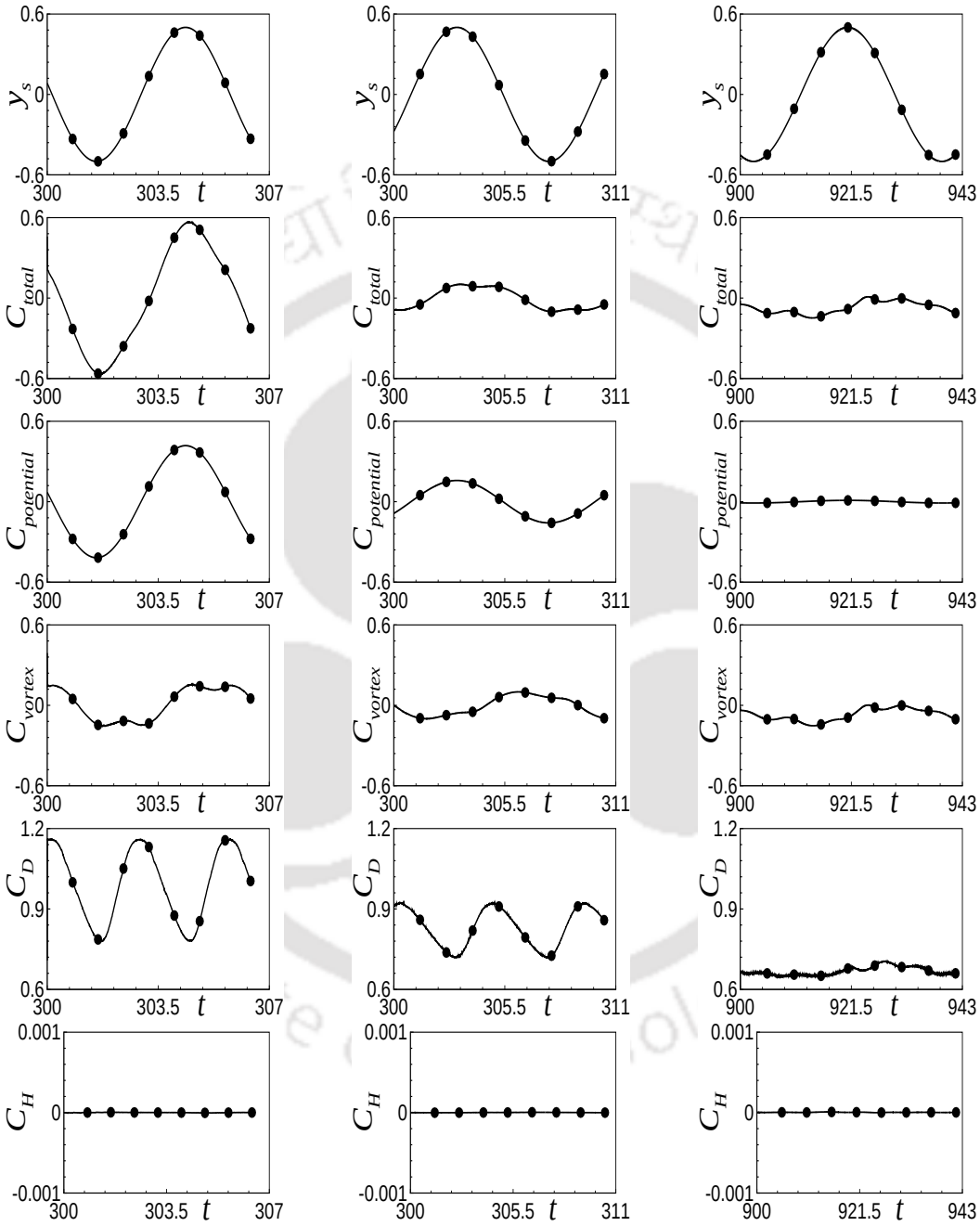

(a) $f_R = 1.3$ (b) $f_R = 0.8$ (c) $f_R = 0.2$

Figure 4.6: Time traces for one oscillation cycle

nized regime. While C_{total}, $C_{potential}$ and C_{vortex} complete one cycle, two full cycles in C_D supports the earlier observation of same state of the wake for stream-wise

oscillations as that of $\pm$ transverse direction of sphere's displacement. The in and out of phases of C_{vortex} with y_s, shown in Figs. 4.6(a) and 4.6(b), clearly point out two different Modes I and II within the synchronized regime as suggested by G-W. On the other hand, Fig. 4.6(c) shows different periodicity of C_{total} and C_{vortex} than the sphere's oscillation at $f_R = 0.2$ which suggests loss of the wake organization attained in the synchronous regime, a feature of Mode III.

4.4 Vortical motion

Three components of vorticity and wake structure which is a measure of rotational motion over shear given by $Q = (R_{ij}R_{ij} - S_{ij}S_{ij})/2 = 0.07$ are used to explain the vortical motions in the wake. The indicated points in Fig. 4.6 correspond to eight equi-spaced frames within a sphere's oscillation cycle.

4.4.1 Periodic vortex shedding

Occurrence of same planar vertical vorticity contours (ω_z) at the mid horizontal plane $z = 0$ for $f_R = 1.3$ and 0.8 in frames (i) and (viii) of Figs. 4.7(b) and 4.8(b) reveal the same oscillation periods of the flow and sphere. This is in agreement with the repeating photographs of the wake behind an oscillated circular cylinder observed by Den Hartog [9]. On the other hand, departure from sphere's oscillation is observed through the non-repetitive sequence of Fig. 4.9(b) at $f_R = 0.2$. As f_R increases the fluttering shear layers are brought closer to each other causing reduced vortex formation length, $4.5D$ at $f_R = 0.8$ (Fig. 4.8(b)(v)) to $4D$ at $f_R = 1.3$ (Fig. 4.7(b)(iii)), thereby increasing the vortex shedding frequency (f_s).

The flapping shear layers are seen to shed a pair of clockwise (dashed) and counterclockwise (solid) vortices in one cycle of sphere oscillation. This can be verified from the frames (iv) and (vii) in Fig. 4.7(b) and frames (vi) and (iii) in Fig. 4.8(b), respectively at $f_R = 1.3$ and 0.8. This shedding pattern is in agreement with the "2R" mode (two vortex rings per sphere's cycle) of G-W in the

synchronized regime. On the other hand, outside this regime, no specific pattern of shedding is observed in Fig. 4.9(b) owing to a lack of synchronization.

We observe that the clockwise vortex is shed when the sphere is near the positive and negative extrema for $1.1 \leq f_R \leq 1.3$ and $0.45 \leq f_R \leq 1.05$, respectively. Zdravkovich [11] for a circular cylinder in the synchronization regime remarked that the oscillating cylinder also imposes the timing of vortex shedding along with the frequency on the wake. Therefore, the existence of Modes I and II for $1.1 \leq f_R \leq 1.3$ and $0.45 \leq f_R \leq 1.05$, respectively can be suggested. While vortex shedding is found to be symmetric about $y = 0$ ($< C_L > \approx 10^{-5}$) for $0.45 \leq f_R \leq 1.3$, a non-zero estimate $< C_L > \approx -0.07$ suggests asymmetric shedding at $f_R = 0.16, 0.2$ similar to that found by Johnson & Patel [18] for a stationary sphere.

4.4.2 Wake structures and planar symmetry

Figures 4.7(c), 4.8(c) and 4.9(c) depict vortex loops oscillating in y direction in the form of chains. These chains oscillate such that a planar symmetry is maintained about the horizontal plane. Three-dimensional iso-surfaces of the transverse vorticity are also symmetric about the same plane for all the cases. This planar symmetry may be attributed to the zero coefficient of vertical force ($C_H \approx 10^{-6}$).

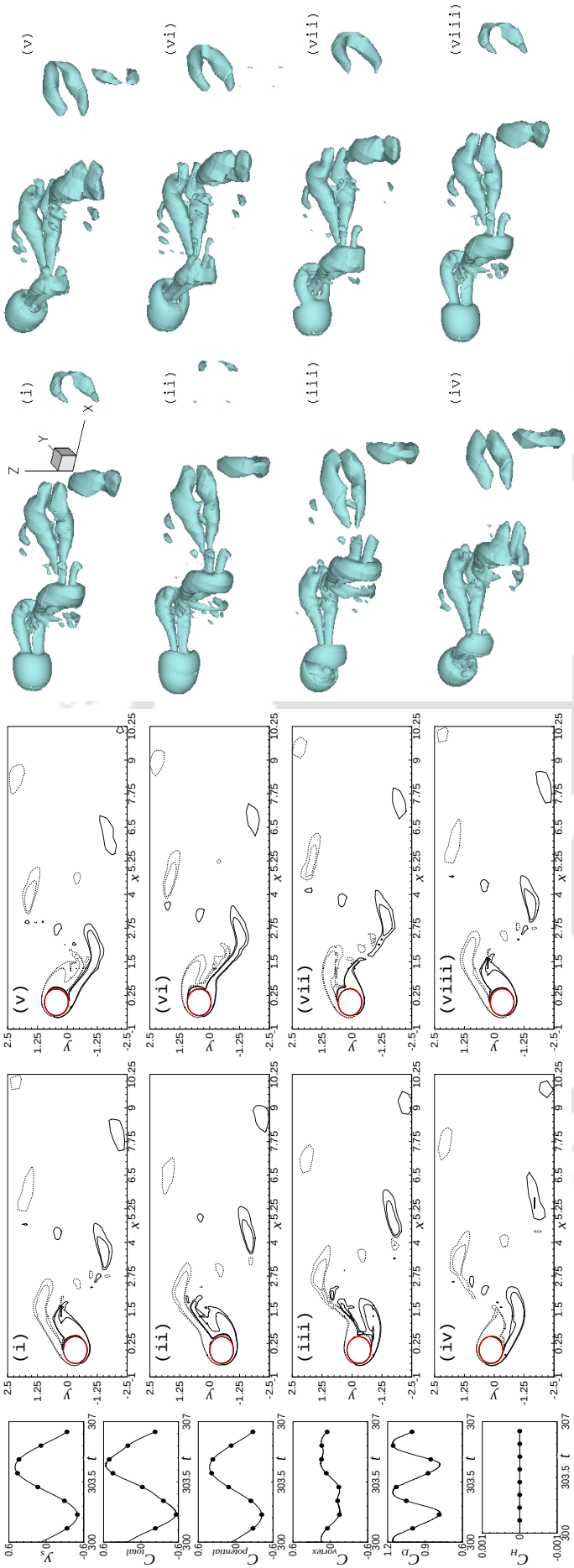

(a) Signals (b) Vertical vorticity (c) Wake structures

Figure 4.7: Instantaneous signals, planar vertical vorticity contours and wake structure at $f_R = 1.3$

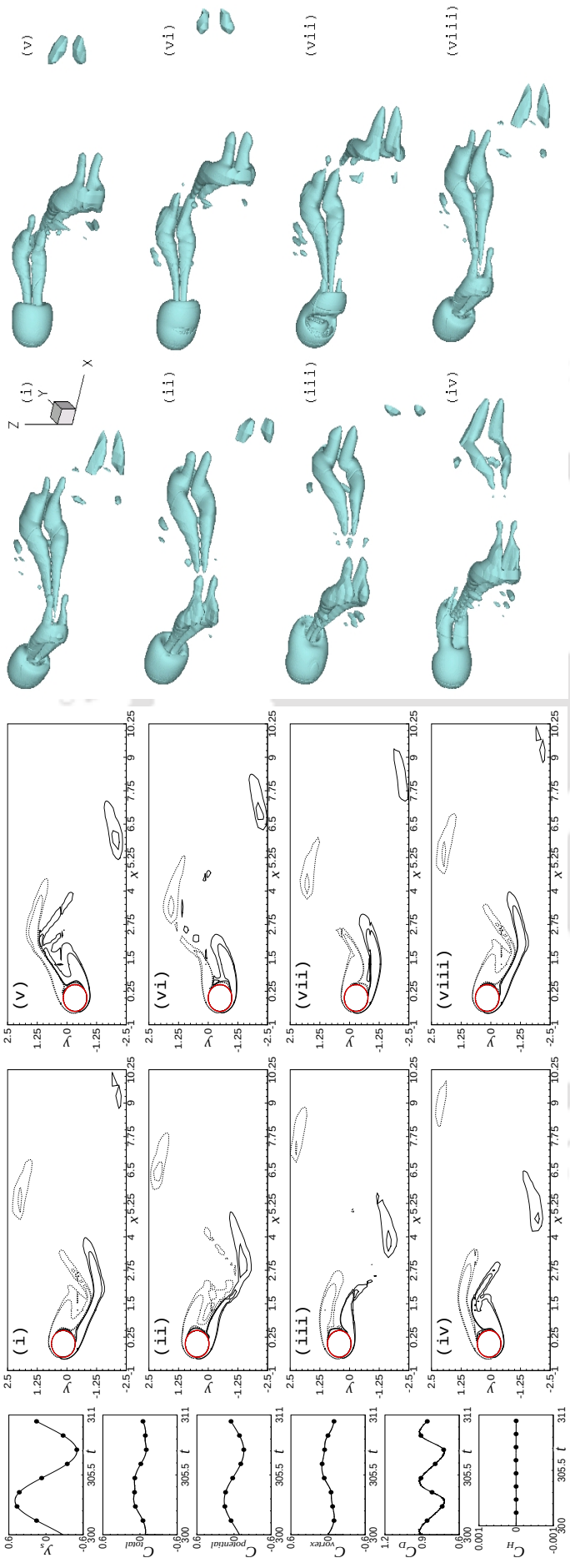

Figure 4.8: Instantaneous signals, planar vertical vorticity contours and wake structure at $f_R = 0.8$

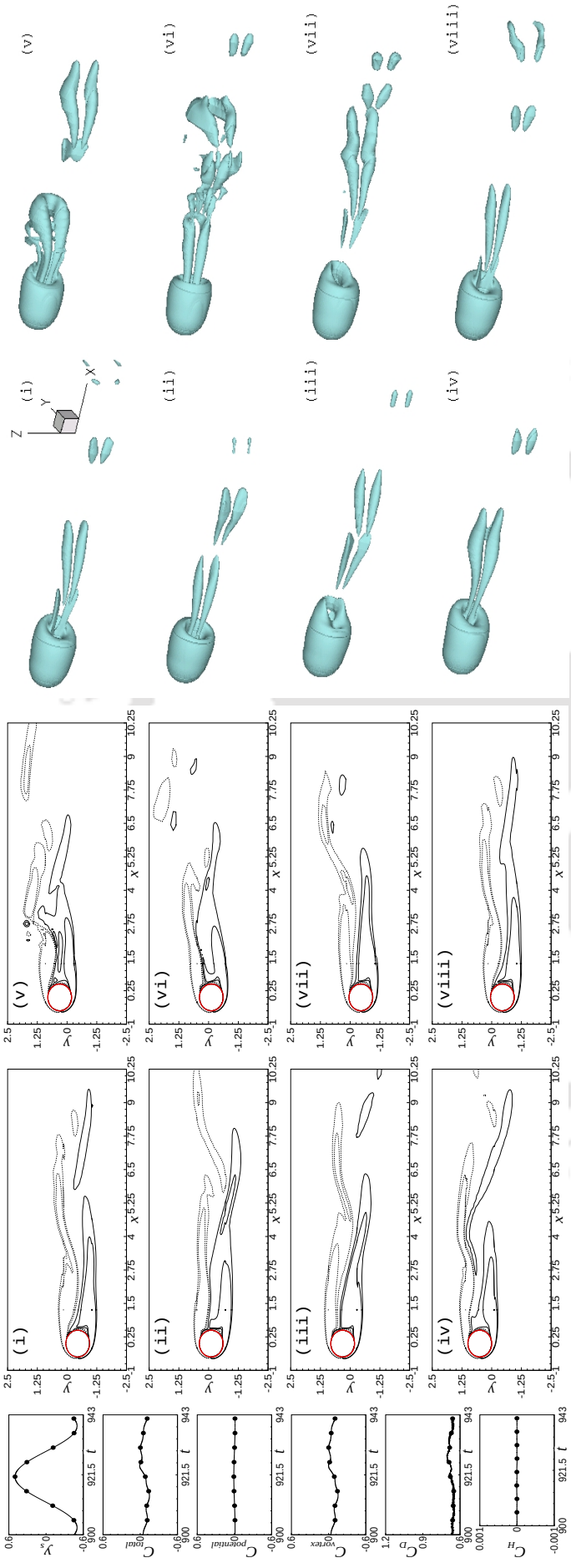

(a) Signals (b) Vertical vorticity (c) Wake structures

Figure 4.9: Instantaneous signals, planar vertical vorticity contours and wake structure at $f_R = 0.2$

In the synchronization regime (Figs. 4.7(c), 4.8(c)), the vortex loops from either side merge and are carried away downstream as vortex rings. The vortex loops at $f_R = 1.3$ are shorter because of the shorter vortex formation length discussed in Section 4.4.1. In the same field of view (FOV) or the observing window, more structures are seen at $f_R = 1.3$. The vortex ring formation at $f_R = 1.3$ starts closer to the sphere. The spacing between the vortex loops is larger at $f_R = 0.8$ in Fig. 4.8(c). A similar observation for the forced transverse oscillation of a circular cylinder were made by Koopmann [59]. He reported that at the lower frequency limit of the "lock-in" regime, the vortex street expands as the longitudinal spacing between the vortex filaments increases.

At $f_R = 0.2$ the vortex loops are highly elongated making a longitudinal thread-like wake in Fig. 4.9(c). The vortex rings are not seen because the frequency is so low that the merging of loops hardly occur. Though the flow is periodic but its period is not same as that of the sphere's oscillation ($f_e/f_s \neq 1$ discussed in Section 4.3.1), therefore, the structures in frames (i) and (viii) are non-repetitive.

4.4.3 Instantaneous vorticity field

Stream-wise vorticity at $x = 1.5$ for $f_R = 1.3$ and 0.8 shown in Figs. 4.10(a) and 4.10(b) confirms the planar symmetry about $z = 0$. Because the positive (solid) and negative (dashed) vorticities are aligned vertically one above the other. Relative timing of the symmetric shedding is observed through the shift in sign of ω_x in frame (iii) near the negative and positive peak of y_s for $f_R = 1.3$ and 0.8 in Figs. 4.10(a) and 4.10(b), respectively. This distinction in the shedding pattern clearly identifies Modes I and II in the synchronized regime.

4.5 Summary

Energy transfer by the fluid to the sphere is found to be negative owing to a larger inertia of the sphere compared to fluid forces at relatively lower Reynolds number

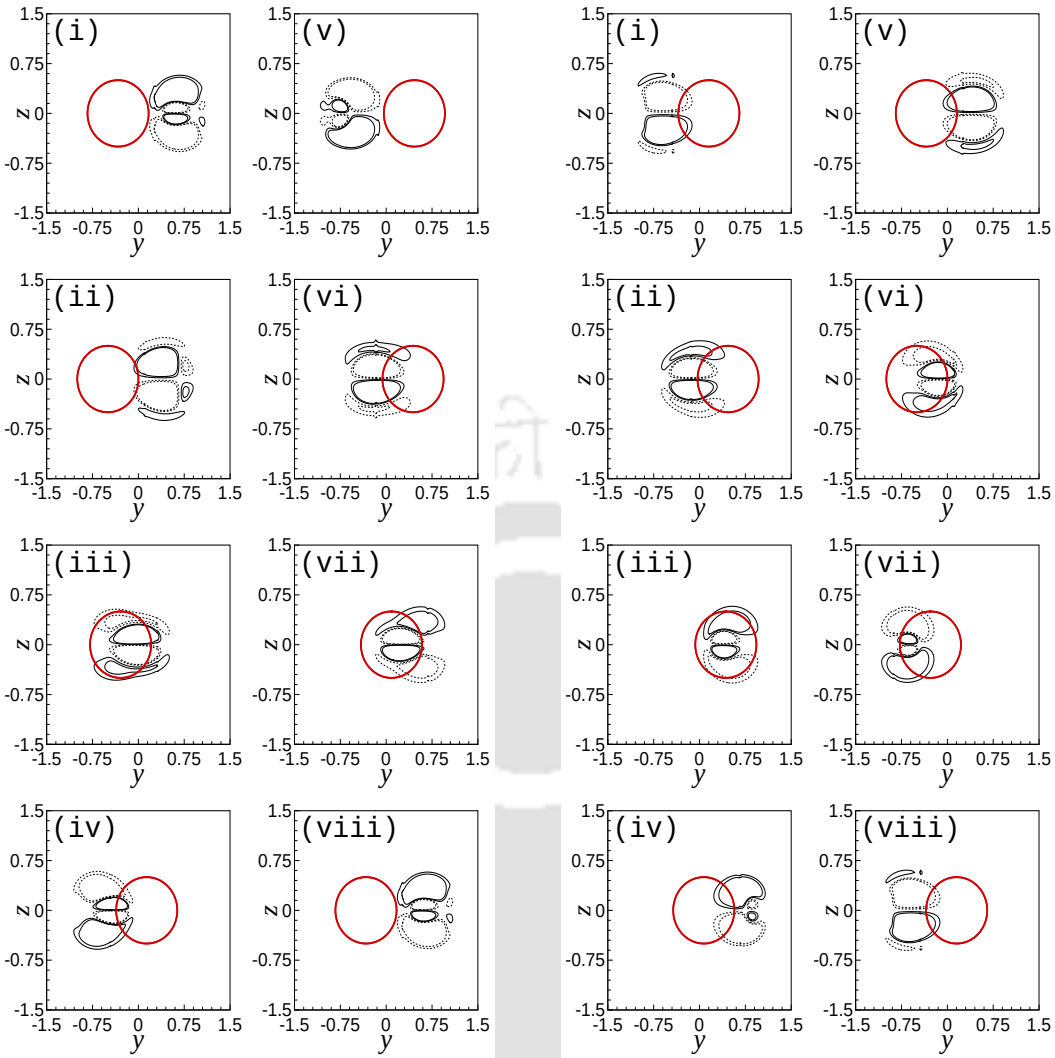

(a) $f_R = 1.3$ (b) $f_R = 0.8$

Figure 4.10: Instantaneous planar stream-wise vorticity contours

($Re = 300$). The instantaneous vertical vorticity component indicates symmetric vortex shedding in the synchronous regime ($0.45 \leq f_R \leq 1.3$) supported by a trivial $< C_L >$ and lack of it outside the regime at $f_R = 0.16, 0.2$ where $< C_L > \approx -0.07$. In the “lock-in" regime the different timing of the symmetric shedding with respect to the sphere motion clearly identifies the Modes I and II for $1.1 \leq f_R \leq 1.3$ and $0.45 \leq f_R \leq 1.05$, respectively. The different shedding timing is also reflected in the opposite phases of the coefficient of vortex (C_{vortex}), a measure of fluid inertia, with sphere motion. Hairpin wake structures in the synchronized regime is supplemented by overlaid stream-wise vorticity, while elongated thread like structures are seen to align in the flow direction outside the “lock-in" regime.

Chapter 5

Uniform flow past a simultaneously oscillating and rotating sphere

The effect of simultaneous transverse oscillation and rotation of the sphere on the resulting wake is studied in details. This chapter reports the results thus obtained and based on the observations made state of the wake has been categorized. Four orientations of the rotational axes with two different oscillating frequencies are considered. The governing equations, computational details and solution strategy are same as in the previous chapter. Additionally, velocity on the surface of the sphere is imposed according to the angular velocity.

5.1 Introduction

Rotation of spherical particles or objects has importance in applications such as conveying particles in gas or liquid flow, fuel droplets in combustors, saltation, meteorology and dynamics of sports ball. In these applications rotation occurs mainly because of velocity gradients and collisions or impulse between particles or boundaries. Typically, rotation occurs about an arbitrary axis in space. Garstang [74] referred rotations about axes along and perpendicular to the direction of flow as side spin (or screw motion) and top spin, respectively. Torobin & Gauvin [75] remarked that pure screw motion will rarely exist in solid-gas systems,

but must be studied as a part of the generalized rotation.

Swerve (an abrupt change of direction) in sports ball or particle motion due to rotation is commonly recognized as Magnus (1853) effect. Barkla & Auchterlonie [76] renamed it as the Robins (1742) effect as Magnus was successful only with rotating cylinders. On account of the Magnus effect, a rotating circular cylinder experiences a large lift force which is usually explained through the Bernoulli's equation.

Due to rotation surface of the cylinder moving along the flow attains higher speed, while the other a lower speed. This asymmetry in the velocity field creates high pressure on lower velocity side. Consequently, fluid moves from high to low pressure region resulting in an opposite reaction force on the cylinder. Magnus effect has significance in many engineering applications such as spinning bullets, trajectory of missiles, design of rotor ships and flettner aeroplanes. Players of all the ball games exploit Robins effect to deceive the opponents.

5.1.1 Rotation about stream-wise axis

Two parameters that govern flow past a rotating sphere are the Reynolds number (Re) and normalized rotational velocity (α). Schlitchting [77], by analysing the previously reported experimental data, noted that the average drag coefficient increases with α as the line of laminar separation on the surface of the sphere moves upstream. These two observations were attributed to generation of extra centrifugal force due to rotation. It was stated that this extra centrifugal force have the same effect as the additional adverse pressure gradient.

Numerical study of Kim & Choi [26] confirmed upstream movement of the separation line and increase in average C_D with increase in α. They discovered a "frozen flow" phenomenon where the vortical structure simply rotates at a constant speed without temporal variation in its shape and strength. Frozen flow was characterized by sinusoidal variation of two components of lift (C_y and C_z) with zero time-averages, but constant magnitudes of the drag and net lift force

$C_l = \sqrt{{C_y}^2 + {C_z}^2}$. The flow was frozen at $Re = 250$ and 300 for $\boldsymbol{\alpha} = 0.1, 0.3$ and $\boldsymbol{\alpha} = 0.5, 0.6$, respectively. The higher rotational speed required at $Re = 300$ was reasoned [26] “to match the shorter time scales of the vortices in the wake".

Three different wake modes were identified by Pier [27] on the basis of time evolution of the force coefficients. First, “Low-frequency helical" wake mode characterised by constant drag and lateral force in the range $225 \leq Re \leq 250$ was reported. In the second, a “Quasi-periodic vortex shedding" mode where lift coefficients displayed quasi-periodic oscillations, was reported. Lastly, a “High-frequency helical" mode was characterised by rotational speed of the flow close to the sphere rotation.

The only experimental study by Skarysz *et al.* [78] was carried out for $Re = 250$ and $0 \leq \boldsymbol{\alpha} \leq 1$. A symmetric influence on vortical structure was observed with respect to sign of rotation. They found that counter-clockwise rotation of the sphere induces a positive stream-wise vorticity in the wake rendering the flow to be periodic and helical.

5.1.2 Rotation about transverse axes

A transversely rotating sphere has been described as consists of two hemispheres [28, 30–33]. The one where the surface velocity assists the flow is called retreating side, while the one that opposes the free stream is known as advancing side. These studies found deflection of the wake towards the advancing side. Moreover, negative transverse vorticity always accumulates towards advancing side with average lift force directed opposite to the wake deflection i.e, towards the retreating side.

The reverse directions of wake deflection and lift force is similar to a rocket propulsion where the exhaust emits downward but the rocket moves upward. Terminology of advancing and retreating side was absent in the work by Kim [29], though wake deflection was reported towards advancing side. A planar-symmetry in the flow was reported [28–33] about a plane normal to the transverse axis.

When the sphere rotates about the transverse axis, Giacobello *et al.* [28] and Kim [29] independently observed suppression of vortex shedding in the range $0.5 \leq \alpha < 0.8$ and $0.4 \leq \alpha \leq 0.6$, respectively, at $Re = 300$. On increasing α further, vortex shedding resumed and was attributed to shear layer instability. Focussing on higher rotational speeds, Dobson *et al.* [32] found a new “separatrix" regime for $\alpha \geq 2.25$ at $Re = 300$. The separatrix divides the free stream flow and the surface driven boundary layer. Poon *et al.* [33] coined a “shear layer–stable foci" regime at $Re = 500, \alpha = 1$ and $640 \leq Re \leq 1000, \alpha \geq 0.8$ where rms of force coefficients increase significantly.

5.1.3 Rotation about an inclined axis

Particles or droplets in engine combustion and chemical processing are required to follow a specified path, but collisions among particles and wall deviate their trajectories. This deviation may result in rotation of the particles about an arbitrary direction. Poon *et al.* [30, 31] observed the effects of inclination of the rotational axis from stream-wise to transverse direction with two intermediate inclinations $\pi/6$ and $\pi/3$ were also considered. The effect of inclining the axis was most evident for $Re = 300, \boldsymbol{\alpha} = 0.5$. At these parameters the flow was found to be frozen [26] and steady [28, 29] for stream-wise and transverse rotations, respectively. However, the two intermediate inclinations lead to an unsteady flow.

5.1.4 Need of the present work

Structures in a flow can acquire motions along any of the six degrees of freedom. However, only a few studies [49–52] exist on combined rotational and translational motions for a circular cylinder. Vortex-induced vibration (VIV) studies exist mainly on three translational *dof* neglecting the rotational ones. Moreover, in many chemical processing industries the particle migration depends on the collision with walls providing simultaneous oscillation and rotation to the particles. To

get an insight of the physics involved in generalized VIV (*dof* greater than one), uniform flow past a sphere undergoing transverse oscillation and rotation simultaneously has been explored.

5.2 Computational details

A sphere of diameter D simultaneously rotates with a constant angular velocity $\mathbf{\Omega}$ and oscillates transversely (as in the previous chapter) in uniform incompressible flow (U). Figure 5.1 shows the computational domain and boundary conditions

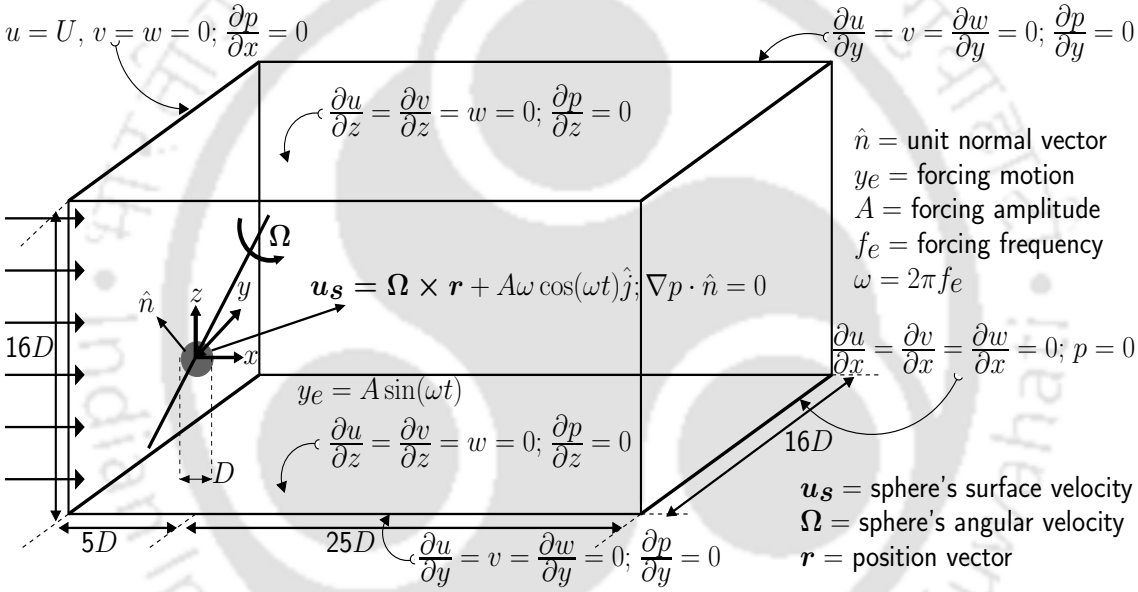

Figure 5.1: Schematic diagram of the oscillating and rotating sphere

in the inertial frame of reference. Four orientations of the rotational axes are considered. First three cases correspond to rotational axis aligned to the primary (x, y or z) axes while in the last case rotational vector has equal components along all three primary axes.

In addition to the transverse motion, if the non-inertial frame of reference is allowed to have rotation, extra pseudo force term [53] arises on the right hand side of the momentum equation. To avoid computations of such an extra force term, only the translating non-inertial frame, same as in the previous chapter, is considered. It should be noted that retaining the same translating non-inertial

frame for the simultaneously oscillating and rotating sphere is possible because the present problem considers only constant angular velocity of the sphere.

The governing equations, computational details and solution strategy remain the same as in the previous chapter. Rotation of the sphere is accounted by additionally imposing velocity on the surface of the sphere. If (x_b, y_b, z_b) represents cartesian coordinates of a point on the surface, then the imposed velocities are

$$\text{Rotation about } x: \quad -2\alpha_x z_b \hat{j} + 2\alpha_x y_b \hat{k} \quad (5.1a)$$

$$\text{Rotation about } y: \quad 2\alpha_y z_b \hat{i} - 2\alpha_y x_b \hat{k} \quad (5.1b)$$

$$\text{Rotation about } z: \quad -2\alpha_z y_b \hat{i} + 2\alpha_z x_b \hat{j} \quad (5.1c)$$

$$\text{Rotation about } xyz: \quad 2(\alpha_y z_b - \alpha_z y_b)\hat{i} - 2(\alpha_x z_b - \alpha_z x_b)\hat{j} + 2(\alpha_x y_b - \alpha_y x_b)\hat{k} \quad (5.1d)$$

where $\boldsymbol{\alpha}(\alpha_x, \alpha_y, \alpha_z) = D\boldsymbol{\Omega}/2U$ is the normalized angular velocity. Simulations are performed for $f_R = 1.3, 0.8$ and $\alpha_x = \alpha_y = \alpha_z = 1.2$ with $\Delta t = 0.001$ at $Re = 300$.

5.3 Time signals

Uniform flow past a stationary sphere is unsteady at $Re = 300$. In general, additional oscillation (or rotation) of the sphere enhances (or suppresses) the unsteadiness in the flow. Time evolution of the force coefficients in conjunction with the sphere's motion reveal time dependency in uniform flow past a simultaneously oscillating and rotating sphere.

Rotation of a sphere about an axis generates non-zero components of surface velocity and force along the remaining two axes (the "Robins effect"). Resultant of these force components accounts for net lift generated on the sphere due to rotation. Inclination of this resultant force with any of the two axes is called lift angle β.

Kim & Choi [26] originally introduced β for a stream-wise rotating sphere. They suggested that the time period of rotation of vortical structures and lift angle are

same. Moreover, rotational speed of the vortical structures was determined by the slope in the time evolution of β. Furthermore, for the cases where time evolution of β did not provide a fixed slope, the speed was estimated in a time-average sense. To identify rotational aspect of the wake β is associated with a subscript which refers to the axis of rotation in the present study.

5.3.1 Larger forcing frequency ($f_R = 1.3$)

Figure 5.2 shows time signals of C_D, C_L, C_H and β at $f_R = 1.3$. Since non-

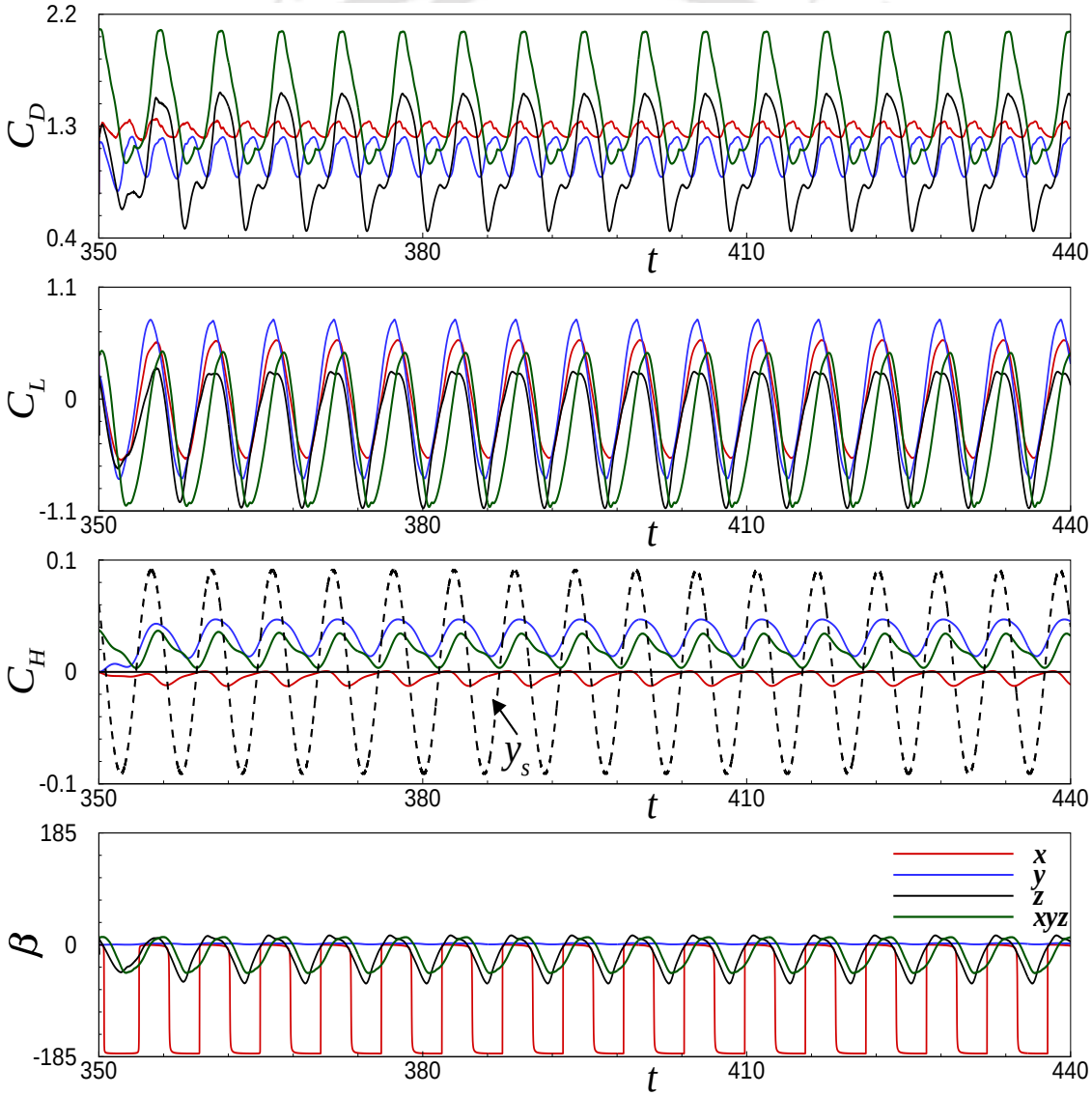

Figure 5.2: Time signals of force coefficients (C_D, C_L, C_H) and lift angle (β) at $f_R = 1.3$. Red, blue, black and green colours correspond to rotations about x, y, z and xyz, respectively

dimensional time period of sphere's oscillation is $T_e = 1/St_e = 1/(f_R St_0) = 1/(1.3 \times 0.137) = 5.61$, the shown time interval of 90 units cover approximately $90/5.61 \approx 16$ oscillation cycles.

Peak-to-peak amplitude of C_D signal for x rotation is least ($C'_D = 0.04$); and point out that this signal is heading towards steadyness. Completion of 32 periodic cycles in C_D for rotation about x and y (blue) over 16 oscillation cycles of the sphere suggests symmetric vortex shedding. On the other hand, completion of 16 cycles for rotation about z (black) and xyz (green) suggests asymmetric vortex shedding. The C_D signal for rotation about xyz attains higher amplitude and fluctuations as now the rotational speed has become $\sqrt{3}$ times the other cases.

Completion of 16 periodic cycles in C_L indicates lock-in for each orientation of the rotational axis. Zero C_H signal for rotation about z demonstrates the preservation of planar-symmetry observed for purely oscillating sphere (previous chapter). In contrast, non-zero C_H signals reveal breaking of this planar-symmetry in the flow for all the other orientations of the rotational axis.

The lift angle β determines the rotational capability of the wake, and has different expressions as given by Eq. (5.2)

$$\beta_x = \tan^{-1}\left(\frac{C_H}{C_L}\right), \beta_y = \tan^{-1}\left(\frac{C_H}{C_D}\right), \beta_z = \tan^{-1}\left(\frac{C_L}{C_D}\right) \tag{5.2}$$

for x, y and z rotations. Subscripts of β in Fig. 5.2 are removed as different colours are assigned for rotation about each axis. For rotation about xyz axis only β_z is plotted as fluid rotation about z axis (measured by ω_z) is observed to be significantly close to the wake structure. Largest and smallest range of β for rotation about x and y, respectively, reveal extreme rotation in the wake.

Phase-portraits

Figures 5.3–5.6 show phase-portraits of force parameters with respect to sphere's oscillation for all the cases. One closed lobe in these portraits demonstrate the lock-in condition for all the cases. Lock-in observed now is different from the pre-

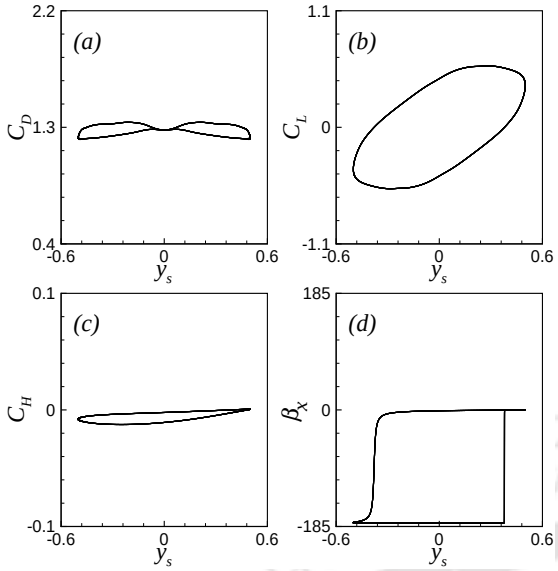

Figure 5.3: Phase-portraits at $f_R = 1.3$ for rotation about x

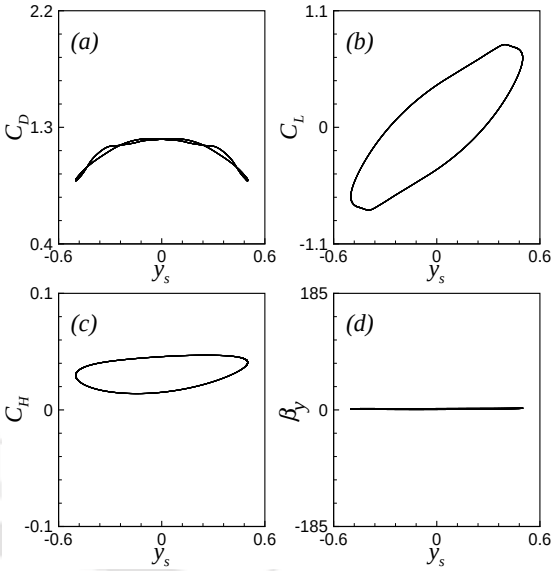

Figure 5.4: Phase-portraits at $f_R = 1.3$ for rotation about y

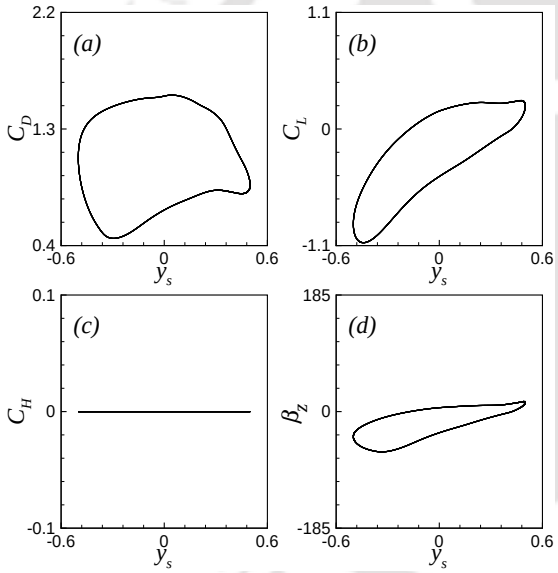

Figure 5.5: Phase-portraits at $f_R = 1.3$ for rotation about z

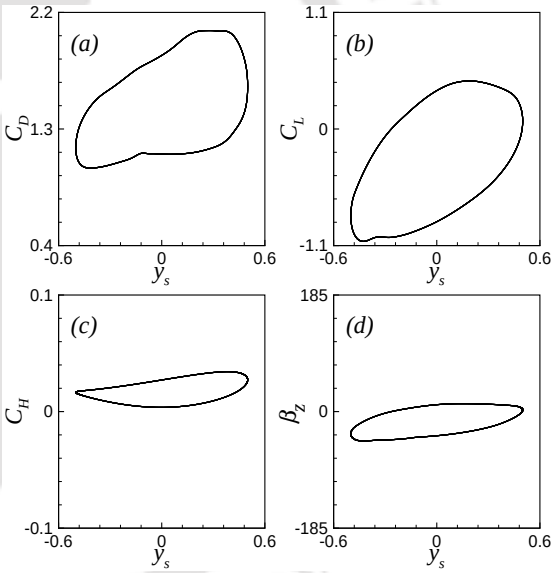

Figure 5.6: Phase-portraits at $f_R = 1.3$ for rotation about xyz

vious chapter. Here the wake is observed to be locked from both oscillation and rotational aspects. Preservation of lock-in implies that the imposing character of the oscillating motion can survive even if the sphere rotates.

Two closed lobes in $C_D - y_s$ plot for rotation about x and y confirm the symmetric vortex shedding. Non-linearity was judged by the frequency spectra. For rotation about y, the amplitude of the higher harmonics is more implying growth of non-linearity resulting in jagged lobes in Fig. 5.4(a). Location of the lobe in

$C_H - y_s$ curve above or below the $C_H = 0$ axis determines breaking of the planar-symmetry observed for a purely oscillating sphere.

For a purely rotating sphere β_x, β_y and β_z must lie in the range $\pm 180°$. Phase-plots for β show departure from this ideal range which implies that oscillation of the sphere hinders full rotation of the wake. Largest enclosed area for β_x highlights greater rotational tendency of the wake for rotation about x axis. On the other hand, smallest enclosed area for β_y points out least rotation in the wake as the axis of rotation coincides with the direction of oscillation.

5.3.2 Smaller forcing frequency ($f_R = 0.8$)

Time signals for $f_R = 0.8$ are shown in Fig. 5.7. Since time period of sphere's oscillation is now 9.12, time span shown covers $90/9.12 \approx 10$ oscillation cycles. As only the red signals (C_L) complete 10 periodic cycles, lock-in observed at $f_R = 1.3$ is absent at $f_R = 0.8$ except for rotation about the x axis.

A closer look at C_L signals show repetition in patterns after every 2 cycles of sphere oscillation for rotation about z. However, for rotation about y and xyz axes no fixed pattern is observed. This loss of fixed pattern can be attributed to the presence of multiple frequencies in the C_L frequency spectrum. Thus, at a lower frequency of oscillation, unlike higher f_R, transverse motion interacts strongly with the rotating motion which transforms the periodic wake into a quasi-periodic or chaotic one.

Similar to $f_R = 1.3$, planar-symmetry is preserved and broken for rotation about z and other axes, respectively. The trend in β is similar to that at $f_R = 1.3$. However, the larger range of β for x rotation, as compared to Fig. 5.2, reveals higher tendency of the wake to rotate in absence of high frequency lateral movement.

Phase-portraits

Occurrence of single closed lobe in Fig. 5.8 confirms the locked state of the wake for rotation about x. On the other hand, absence of it in Figs. 5.9, 5.10 and

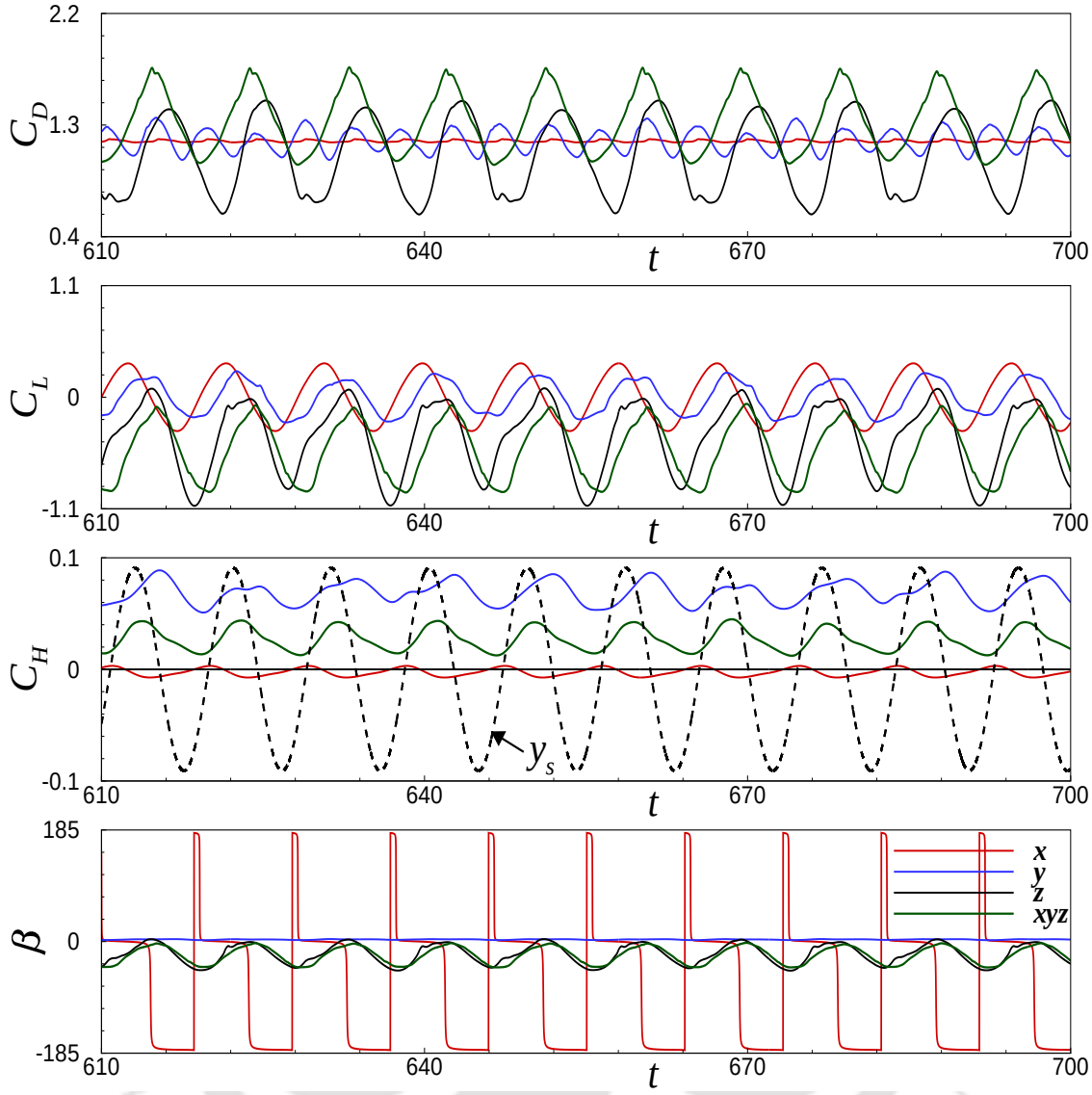

Figure 5.7: Time signals of force coefficients (C_D, C_L, C_H) and lift angle (β) at $f_R = 0.8$. Red, blue, black and green colours correspond to rotations about x, y, z and xyz, respectively

5.11 confirms the departure. The lack of synchronization of the wake at $f_R = 0.8$ implies that the imposing character of the transverse oscillation is over powered by the rotational motion. Larger enclosed area in $\beta - y_s$ curve for x-rotation at $f_R = 0.8$ as compared to $f_R = 1.3$ signifies higher rotation of the wake.

Change of trajectories in Figs. 5.9 and 5.11 is a consequence of no fixed pattern in the time signals, and reflect the chaotic nature of the flow (or highly irregular). Two distinct lobes are observed in Fig. 5.10 as period of the flow is twice the sphere's motion which indicates a quasi-periodic nature of the wake.

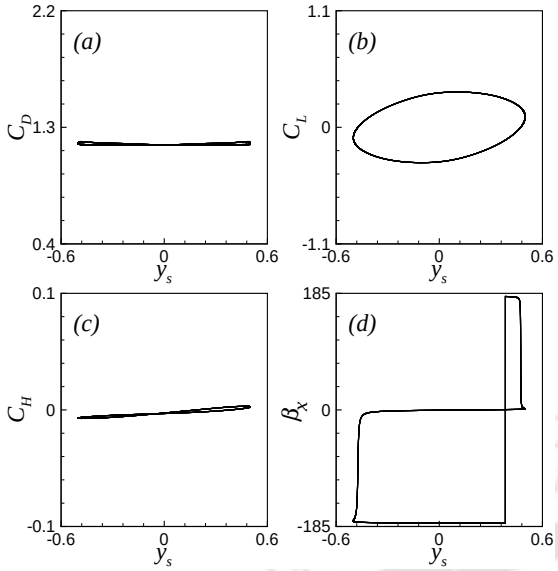

Figure 5.8: Phase-portraits at $f_R = 0.8$ for rotation about x

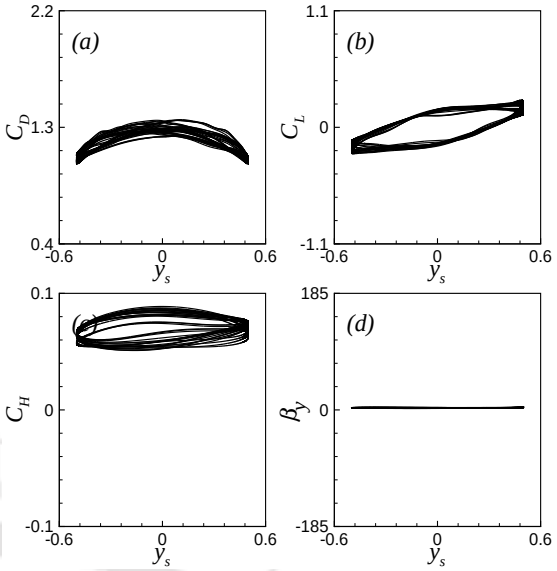

Figure 5.9: Phase-portraits at $f_R = 0.8$ for rotation about y

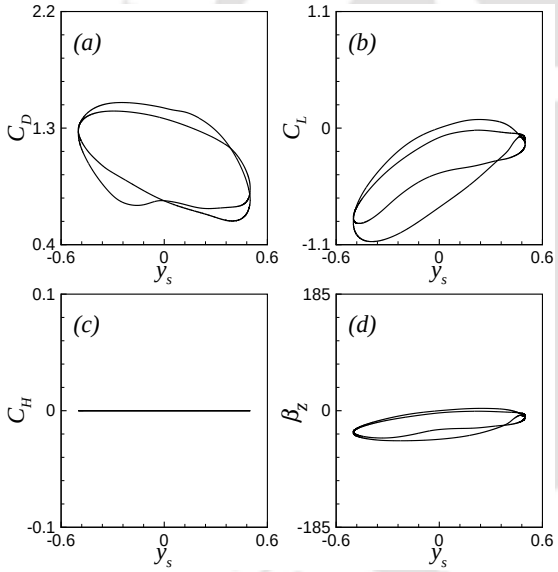

Figure 5.10: Phase-portraits at $f_R = 0.8$ for rotation about z

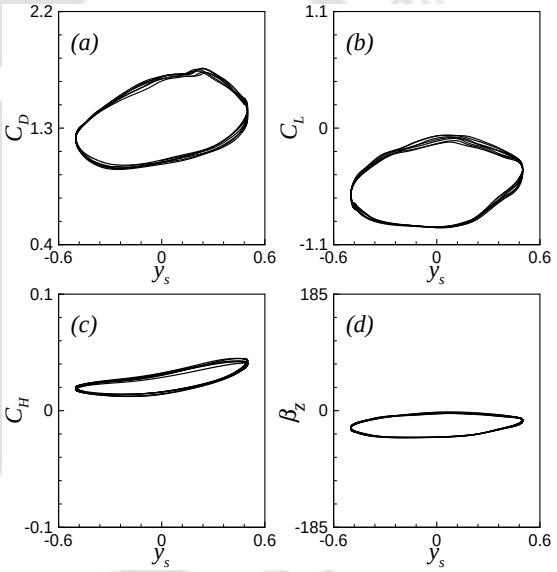

Figure 5.11: Phase-portraits at $f_R = 0.8$ for rotation about xyz

5.3.3 Global flow parameters

Table 5.1 compares the average global flow parameters obtained from the time signals shown in Figs. 5.2 and 5.7. Higher values of rms quantities (C'_D, C'_L) at $f_R = 1.3$ over $f_R = 0.8$ implies greater fluctuations in the near wake. Source of these higher fluctuations can be attributed to lower vortex formation length and higher vortex shedding frequency at $f_R = 1.3$ (as observed in the previous

Axis	f_R	$< C_D >$	$< C_L >$	$< C_H >$	C'_D	C'_L	C'_H	$< \beta >$
x	1.3	1.27	-7×10^{-5}	-5×10^{-3}	0.04	0.42	4×10^{-3}	-1.57
	0.8	1.17	3×10^{-4}	-3×10^{-3}	9×10^{-3}	0.23	3×10^{-3}	-1.19
y	1.3	1.07	-8×10^{-5}	0.03	0.12	0.54	0.01	0.03
	0.8	1.18	-2×10^{-3}	0.07	0.09	0.16	0.01	0.06
z	1.3	1.03	-0.26	1×10^{-6}	0.35	0.46	5×10^{-7}	-0.27
	0.8	1.05	-0.41	-4×10^{-8}	0.30	0.35	1×10^{-6}	-0.36
xyz	1.3	1.45	-0.32	0.02	0.37	0.53	0.01	-0.27
	0.8	1.33	-0.52	0.03	0.25	0.29	0.01	-0.39

Table 5.1: Comparison of the global flow parameters

chapter). Based on this reasoning average drag coefficient ($< C_D >$) should follow a similar trend. However, it violates this behaviour at $f_R = 1.3$ for rotation about y and z, and thus $< C_D >$ at $f_R = 0.8$ exceed that at $f_R = 1.3$ for these rotations.

In the present problem, the flow is influenced by the oscillation as well as rotational motion of the sphere. In another words, there is a competition between the oscillation and rotational motion. The increased $< C_D >$ at $f_R = 0.8$ can be explained from the perspective of rotational motion. For a transversely rotating sphere Giacobello *et al.* [28] observed that the shear layer over the retreating side retracts upstream with increasing rotation rate which results in increase in $< C_D >$ with $\boldsymbol{\alpha}$. At a lower oscillation inertia, $f_R = 0.8$, the flow is governed more by the rotation than oscillation which causes increase in $< C_D >$.

Rotation about y generates a velocity component in the flow along the negative z direction in accordance with Eqs. (5.1b) and (5.1d). This velocity generates a centrifugal force in the flow towards the negative z direction. In reaction to this centrifugal force, the sphere experiences a force along positive z direction which

is the source of increased $< C_H >$ and C'_H for y and xyz rotations. The higher magnitudes of $< C_H >$ and C'_H at $f_R = 0.8$ clearly points out dominance of rotational motion at smaller transverse velocity.

Last column in the Table 5.1 shows average values of β in radians. At each f_R the average value shows a decreasing trend (in magnitude) as the axis of rotation aligns from x to z and then to y. Higher values of β at $f_R = 0.8$ over $f_R = 1.3$ confirms domination of rotational effects at lower f_R because of the lower oscillation inertia. Though $< \beta >$ is lower for x rotation at $f_R = 0.8$ than at $f_R = 1.3$, the rotational tendency is found to be higher.

5.4 Vortical motions

A fluid element can undergo four different types of motion or deformation: translation, rotation, extensional strain and shear strain. The rotational motion in the flow is generally measured in terms of vorticity which is defined in the direction of angular velocity of the fluid element having twice its magnitude.

In the present study vortical motion in the wake is observed at eight equi-spaced instances over an oscillation cycle of the sphere. Planar contours of three components of vorticity i.e., stream-wise (ω_x), transverse (ω_y) and vertical (ω_z) at $x = 1.5$, $y = 0$ and $z = 0$ planes, respectively, are analysed. Solid and dashed lines (levels $\pm 1, \pm 0.5$) are used to represent positive (anti-clockwise) and negative (clockwise) vorticities, respectively. It should be noted that the sense of rotation depends upon the viewing direction. For example, y-z plane can be looked from positive and negative x axis. A clockwise rotation from the positive x axis appears to be anti-clockwise if viewed from negative x direction. Therefore, the orientation of the axes in the planar plots of vorticity contours is oriented in such a way that solid contour rotates in anti-clockwise direction while negative in the clockwise. Three-dimensional iso-surfaces of wake structure ($Q = 0.07$) are overlayed by the vorticity component along the axis of rotation (levels ± 0.5) in order to relate the

significance of Q criterion with vorticity for visualizing the topology of the wake. Green, blue and red colours represent wake structure, negative and positive vorticity components along the rotational axis, respectively.

5.4.1 Larger forcing frequency ($f_R = 1.3$)

Existing literature on transversely rotating sphere [28–33] suggests no difference between the transverse and vertical axes. However, studies on a stationary sphere [18, 21] have reported different values of force coefficients along these two directions which suggests lack of similarity in them. In the present problem due to the transverse oscillation flow behaviour is expected to exhibit difference along these two axes. Moreover, the stream-wise rotation [26, 27, 78] causes different flow features. To develop a clear understanding of the flow, the rotation about each of the four axes is presented separately.

Case I: Stream-wise (x) rotation

Figure 5.12(a)-(c) shows time evolution of force coefficients, planar stream-wise vorticity contours and three dimensional wake structure at eights instances (marked by black dots in the signals) over an oscillation cycle of the sphere. Two cycles in the C_D signal are seen due to symmetric vortex shedding. For a purely rotating sphere at $Re = 300$ and $\alpha_x = 1.2$ wake was characterised [27] by same frequencies and amplitudes of C_L and C_H. Though the frequencies of C_L and C_H are same here, their amplitudes differ significantly ($C'_L = 0.42$, $C'_H = 0.004$ in Table 5.1). High amplitude of C_L is obtained because of additional oscillating motion of the sphere.

Figure 5.12(b) and (c) display the locked state of the wake by same flow patterns in frames (i) and (viii). The solid line contours representing positive stream-wise vorticity are more stronger than the dashed lines contours. This observation is similar to the previous studies [26, 78] that stream-wise rotation strengthens the positive vorticity and weakens the negative ones.

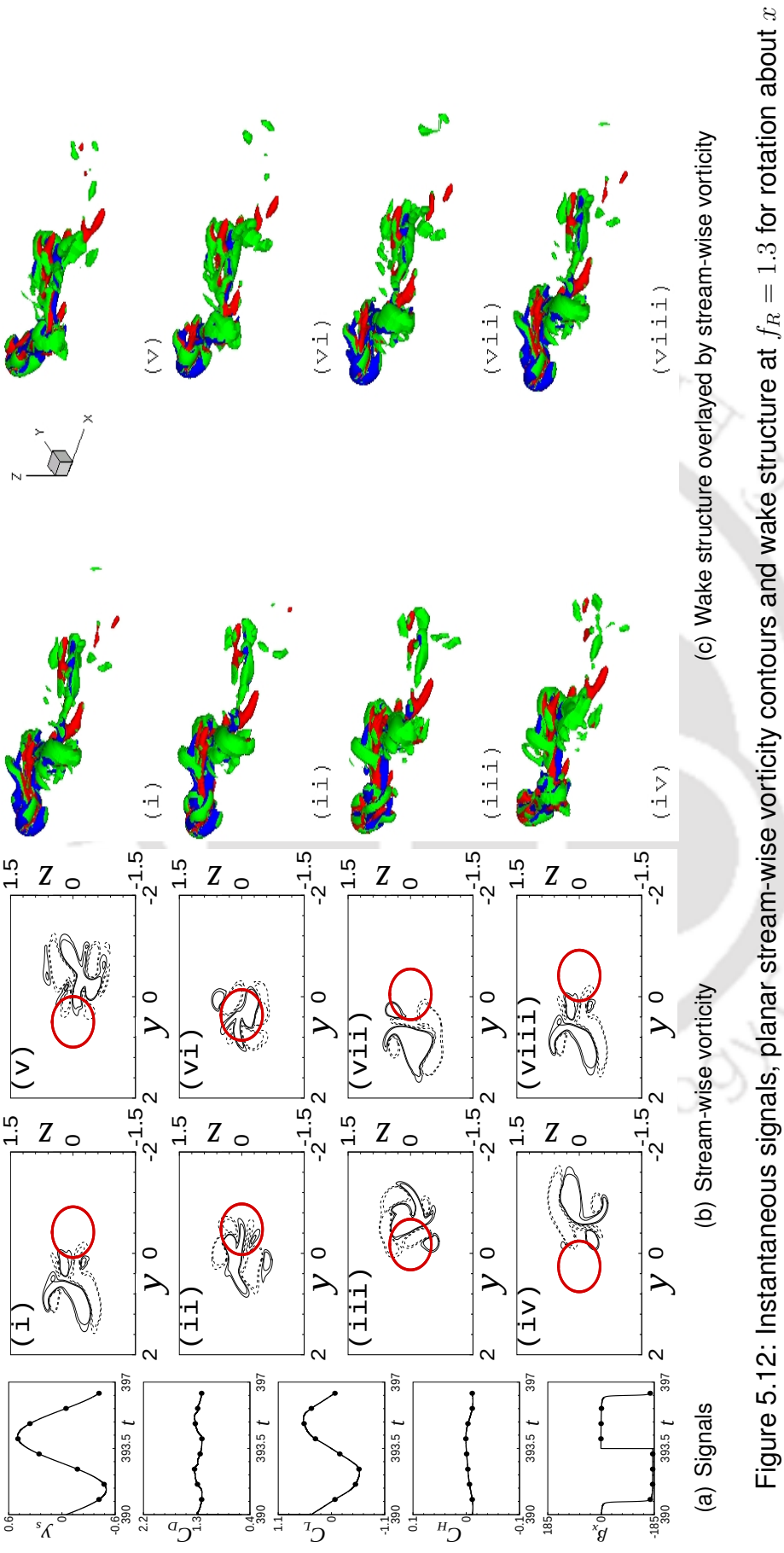

(a) Signals (b) Stream-wise vorticity (c) Wake structure overlayed by stream-wise vorticity

Figure 5.12: Instantaneous signals, planar stream-wise vorticity contours and wake structure at $f_R = 1.3$ for rotation about x

Appearance of stream-wise vorticity contours in Fig. 5.12(b) along $\pm y$ directions are same over an oscillation cycle of the sphere. Consequently, averageC_L is approximately zero as seen in Table 5.1 which is the result of symmetric vortex shedding.

Figure 5.12(c) shows the wake structure (green) overlayed by stream-wise vorticity (red-positive and blue-negative). Absence of negative ω_x (blue) in far downstream immediately confirms higher intensity of positive ω_x. This observation supports the strengthening of positive vorticity as seen in the planar contours.

The Q structure indicates the wake as a chain of vortex loops oscillating in alternating sides of the sphere as seen in the previous chapter. Additionally, the chain has anti-clockwise rotation about the x axis. This rotation drives the boundary layer around the sphere's surface and twists the shear layers from top and bottom surfaces of the sphere. Consequently, an interwinding pattern between negative and positive ω_x is seen. The twisting nature of the chain suggests a helical wake which was previously reported [26, 27, 78].

Appearance of the contours helps in determining the location of the chain. Figure 5.12(b) shows that contours are on negative y from frames (iii) to (v) whereas they are towards positive y in the other frames. To see how the appearance of these contours determines the location of the chain, consider frame (v). The contours are on negative y and the chain sweeps in the negative y direction. Moreover, the fifth instance corresponding to frame (v) shows a positive C_L implying that the C_L is exerted in an opposite direction of the chain movement.

Case II: Transverse (y) rotation

Symmetric vortex shedding is seen to occurs for y-rotation also which is evident from the two C_D cycles in Fig. 5.13(a). Table 5.1 shows that C'_D (wake oscillation) shoots from 0.04 to 0.12 for x to y rotation. Fluctuations have a strong connection with increase in oscillation of stream-wise velocity and pressure which leads to fragmented ω_x seen in Fig. 5.13(b).

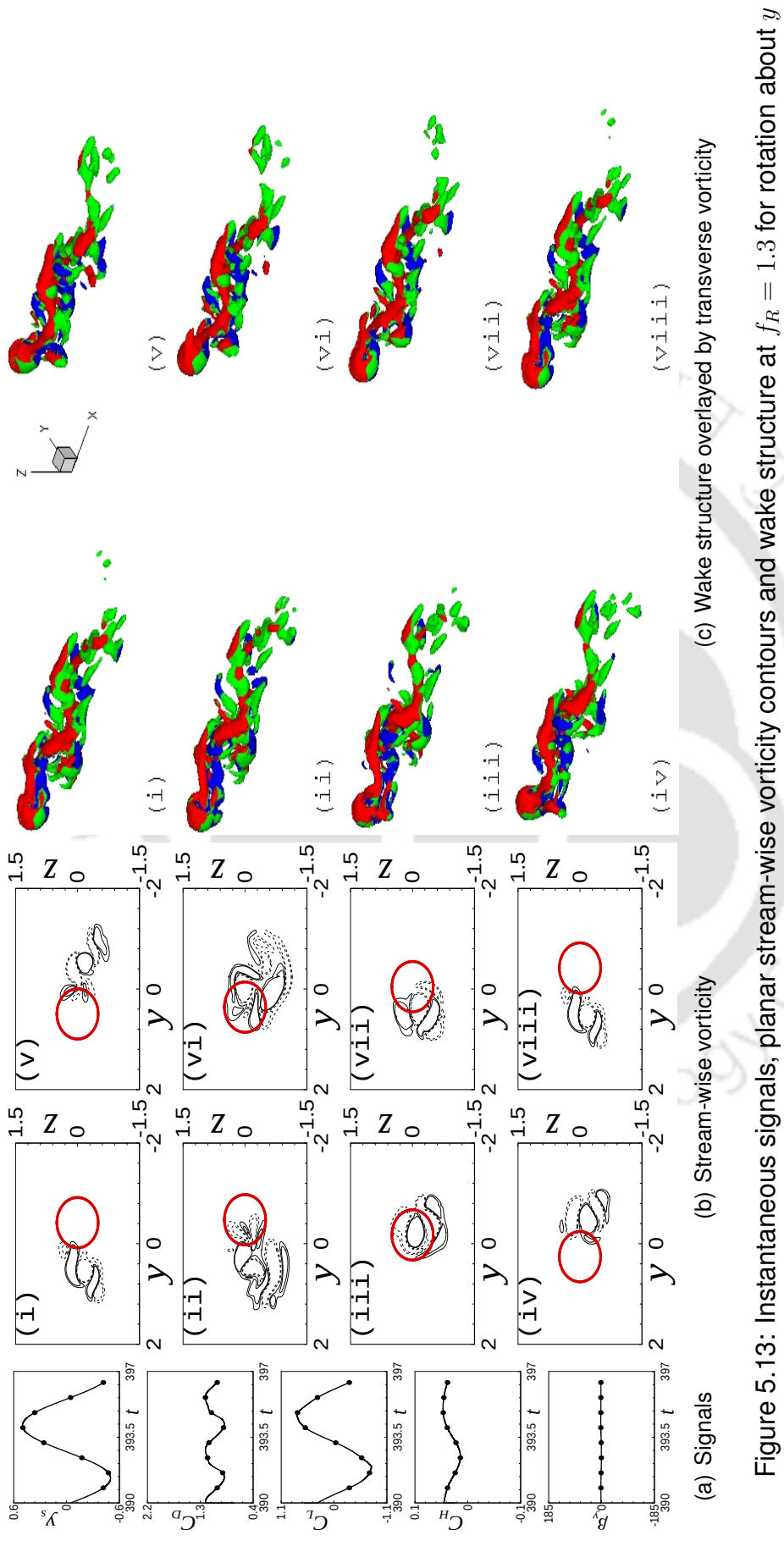

Figure 5.13: Instantaneous signals, planar stream-wise vorticity contours and wake structure at $f_R = 1.3$ for rotation about y

Giacobello *et al.* [28] found that the introduction of sphere rotation increases the surface-to-free stream velocity gradient on the advancing side of the sphere and decreases it on the retreating side. This leads to a progressive intensification and thinning of the shear layer released from the advancing side. On the other hand, shear layer on the retreating side is weakened and pulled towards the advancing side.

Poon *et al.* [33] stated that “most of the vortices are released from the shear layer on the advancing side". This observation suggests that the vorticity dynamics in the wake is dictated by the generation, diffusion and convection of vorticity on the advancing side.

The observations made by Giacobello *et al.* [28] and Poon *et al.* [33] combinedly implies a deflection in the wake towards the advancing side of the sphere along with narrowing of the wake. Comparing the contours in Figs. 5.12(b) and 5.13(b), it is observed that now the contours are not symmetrically placed about $z = 0$, but tilted along negative z direction (downward) which is the advancing side. Consequently, the sphere in reaction to the downward deflection experiences an upward force evident by $C_H > 0$ signal in Fig. 5.13(a).

Figure 5.13(c) shows the Q structure (green) overlayed by the iso-surfaces of transverse vorticity (red-positive and blue-negative). The wake is a chain oscillating on both the sides with an additional anti-clockwise rotation about the y axis. Appearance of clockwise transverse vorticity (blue) on advancing side ($-z$) of the sphere is in agreement to the literature [28, 30–33].

A closer look at the blue and red coloured iso-surfaces display an anti-clockwise and clockwise sense of rotation, respectively, which is contrary to what they must be. The reason for this contradiction is the viewing direction explained in the second paragraph of section 5.4. Therefore, to see the true sense of rotation we must see these iso-surfaces from the positive y axis. Only then blue and red coloured iso-surfaces will display clockwise and anti-clockwise rotations, respectively.

A comparison of the wakes in Figs. 5.12(c) and 5.13(c) demonstrate a narrower wake for y-rotation. This narrowing of the wake is expected based on the observations of Giacobello *et al.* [28] and Poon *et al.* [33]. A planar-symmetry reported [28–33] for a transversely rotating sphere is absent here because of the simultaneous oscillating motion of the sphere, which generates high fluctuating force along the y axis.

Case III: Vertical (z) rotation

One cycle of C_D in Fig. 5.14(a), unlike the two previous cases, suggests asymmetric vortex shedding. In contrast x, y rotations, now the ω_x contours accumulate on positive y side. This observation suggests deflection of the wake towards positive y (advancing side of the sphere). In reaction to this the sphere experiences a lift along the negative y direction which is evident by a non-zero $< C_L >= -0.26$ in Table 5.1.

The stream-wise vorticity is found to be symmetric about $z = 0$ in such a way that negative and positive contours are aligned vertically over each other. The wake also shows a planar symmetry in the flow about the horizontal midplane, $z = 0$. This symmetry is attributed to $C_H = 0$ as also observed for a purely oscillating sphere in the previous chapter.

Kim [29] reported upward deflection of the wake with $C_L < 0$ while Poon *et al.* [33] and others [28, 30–32] found it to be downward with $C_L > 0$ for a transversely rotating sphere. This difference in deflection of the wake is owing to the selection of transverse axis (y or z). A remarkable finding [28–33] for a transversely rotating sphere is that the deflection of the wake and appearance of the clockwise vorticity is always on the advancing side, whichever axis (y or z) is selected.

In the present work, the advancing sides are $-z$ and $+y$ for rotations about y and z, respectively. Therefore, the deflection of the wake and appearance of clockwise vorticity (along the direction of rotation i.e., ω_y and ω_z for y and z rotations, respectively) represented by blue coloured iso-surfaces are on the advancing side of the sphere. Similar to x and y rotations, the wake is a chain on

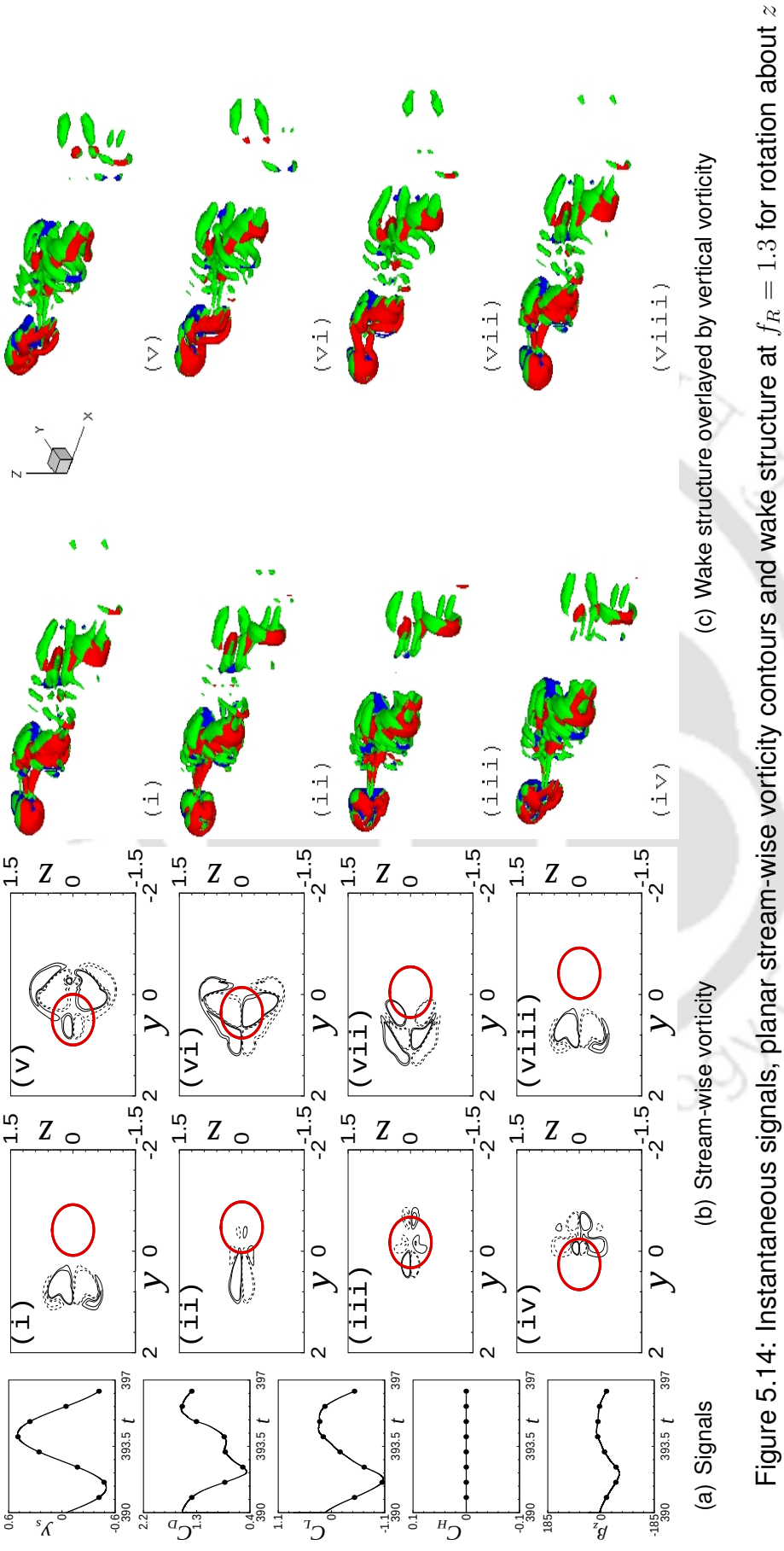

(a) Signals (b) Stream-wise vorticity (c) Wake structure overlayed by vertical vorticity

Figure 5.14: Instantaneous signals, planar stream-wise vorticity contours and wake structure at $f_R = 1.3$ for rotation about z

alternating sides, but now the chain has an anti-clockwise rotation about the z axis.

Case IV: All-axes (xyz) rotation

This case corresponds to four *dof* (one transverse oscillation and three rotations about the primary axes) of the sphere which makes it relevant with practical situations. The rotational velocity is composed of equal components along x, y, z axis i.e., $\alpha_x = \alpha_y = \alpha_z = 1.2$ making resultant speed as $\sqrt{3}$ times the other cases. This case is expected to demonstrate a combination of flow features observed for three primary rotations. Additionally, this case serves to reveal the flow physics at a higher rotating speed i.e., $\sqrt{3} \times 1.2$.

Table 5.1 for rotation about y axis shows that $< C_L >$ is zero, but $< C_H >$ is non-zero. On the other hand, for z rotation $< C_L >$ is non-zero, but $< C_H >$ is zero. As stated above the present case must reflect the features of both y and z rotations which is supported by non-zero $< C_L >$ and $< C_H >$. Moreover, to mark a higher rotation speed, $< C_D >= 1.45$ and $C'_D = 0.37$ are the highest among all the cases. An increase in average C_D, C_L with $\boldsymbol{\alpha}$ was previously reported [28–30] for a transversely rotating sphere. Kim & Choi [26] accounted the increase in average C_D with $\boldsymbol{\alpha}$ to increasing pressure coefficient for a stream-wise rotating sphere.

Contours of stream-wise vorticity in Fig. 5.15(b) are seen to shift towards positive y direction the most among all the cases. Consequently, the sphere experiences largest negative reaction force along y direction which is evident from maximum magnitude of $< C_L >$ (-0.32) in this case. Twisting motion of the wake is observed to change the position of positive and negative ω_x in Fig. 5.15(b) which can be attributed to the non-zero component of surface velocity along x.

Transverse and vertical vorticity contours in Fig. 5.16 indicate deflection of the wake towards negative z and positive y directions, respectively. The sphere in reaction experiences forces along $-y$ and $+z$ directions leading to asymmetric vortex shedding and breaking of planar symmetry in the flow. The wake is seen

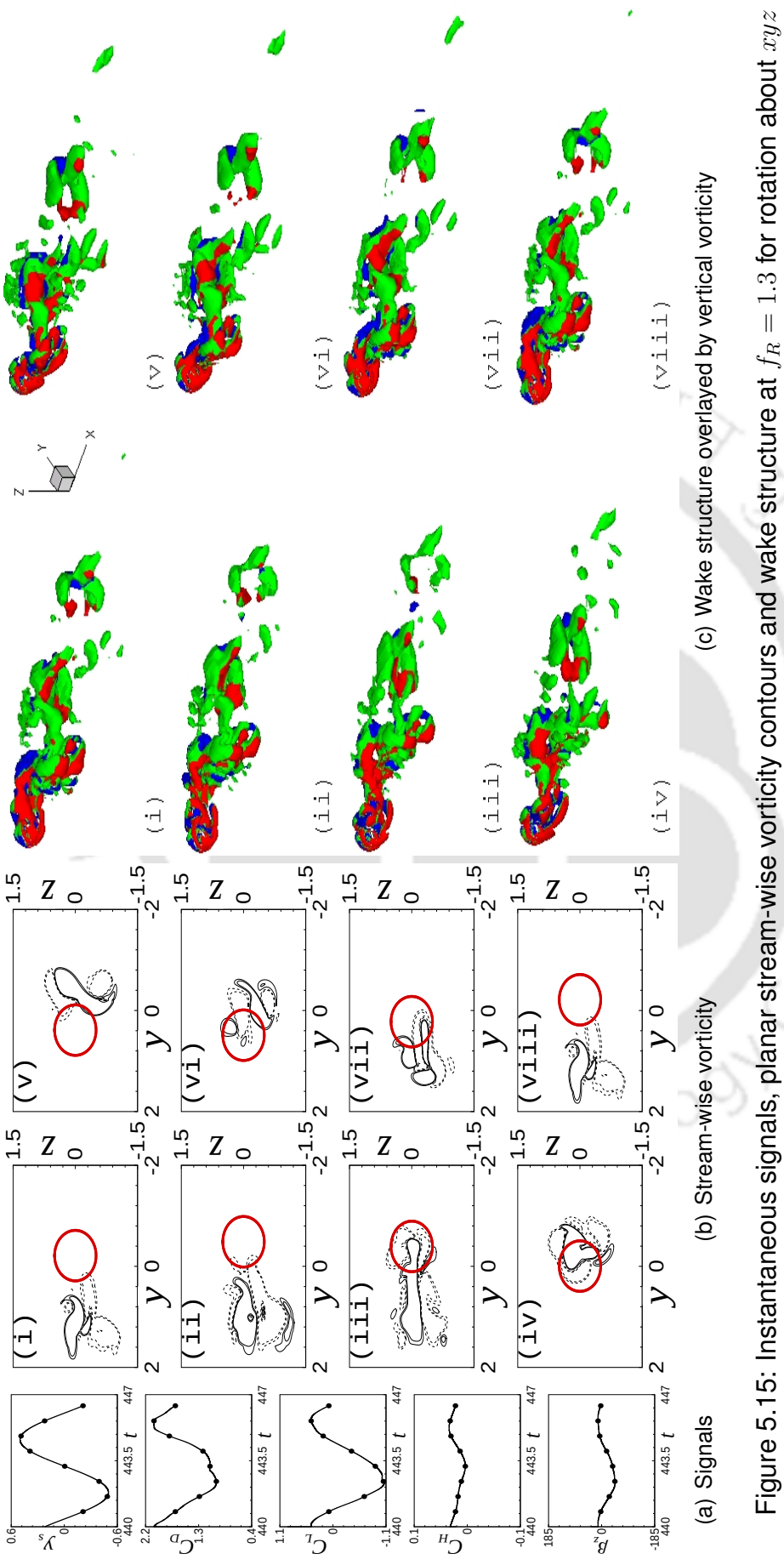

(a) Signals (b) Stream-wise vorticity (c) Wake structure overlayed by vertical vorticity

Figure 5.15: Instantaneous signals, planar stream-wise vorticity contours and wake structure at $f_R = 1.3$ for rotation about xyz

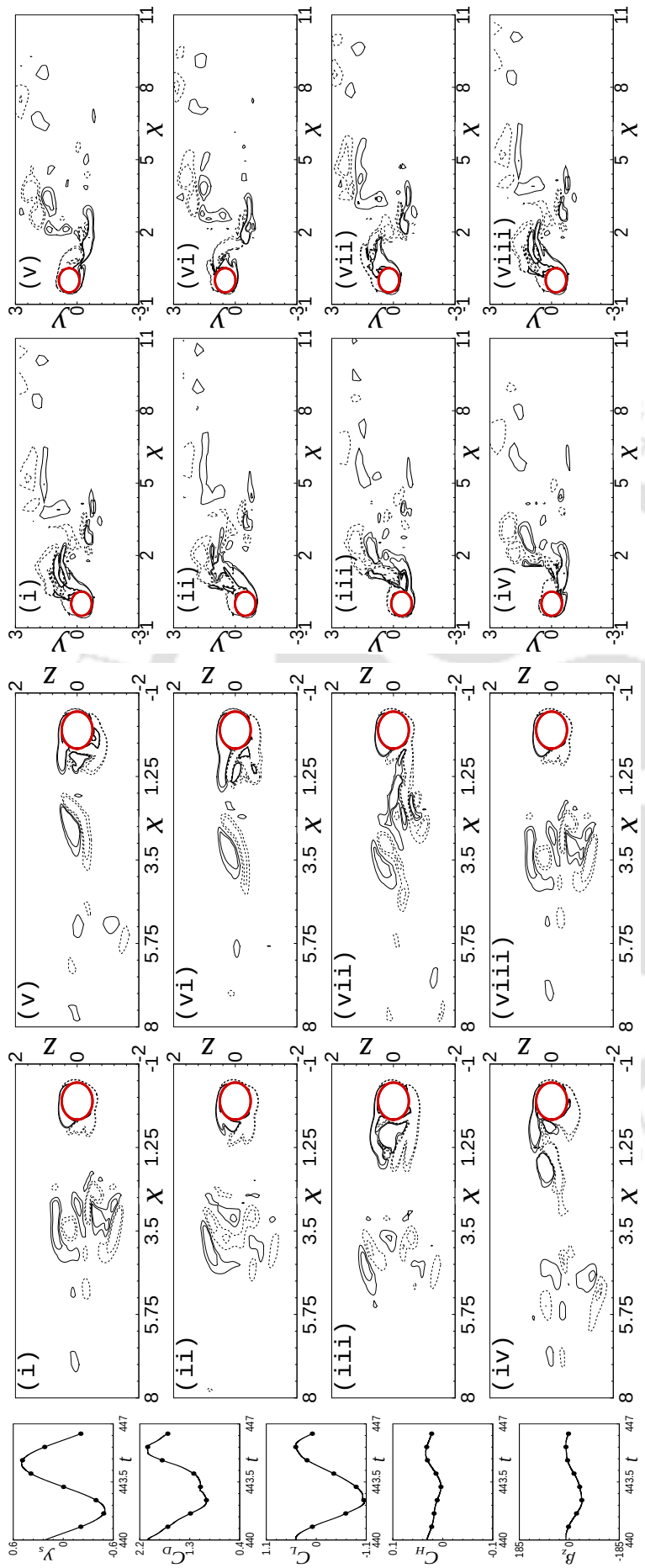

Figure 5.16: Instantaneous signals, transverse and vertical vorticity at $f_R = 1.3$ for rotation about xyz

to reveal the locked sate even though the flow does not exhibit planar symmetry or symmetric vortex shedding. The vortical structures, shown in Fig. 5.15(c), are overlayed by iso-surfaces of ω_z as vertical component of vorticity is found to be prominent. In addition to oscillation along y, the wake exhibits anti-clockwise rotation about all the three primary axes. The wake seems to shed Ω-shaped loops with a nose in the middle of the loops as seen in Fig. 5.15(c). For a rotating sphere Poon *et al.* [30] observed distorted Ω-shaped structures. Moreover, in case of a stationary sphere at very high Re, Taneda [79] experimentally and Jindal *et al.* [80] numerically found these structures with an offset from stream-wise axis causing non-zero lateral forces.

5.4.2 Smaller forcing frequency ($f_R = 0.8$)

Simultaneous oscillation and rotation of the sphere in uniform flow offers two different perspectives. In one study the focus can be on the rotational motion by changing the speed and orientation of the axis while fixing the oscillation motion. On the other hand, the focus can be on the oscillation motion by changing the amplitude and frequency ratio while keeping the rotational motion unchanged.

The previous section 5.4.1 focussed mainly on the effects of change in orientations of the rotational axis at a fixed $f_R = 1.3$. In this section, the same rotational speed and axis of orientations are considered at lower $f_R = 0.8$. Therefore, the gross flow features are expected to be similar to the previous section from rotational point of view. However, the change in f_R is expected to modify the flow from oscillation point of view.

Case I: Stream-wise (x) rotation

Figure 5.17 confirms the locked state of the wake similar to that at $f_R = 1.3$, but positive extension of β_x as compared to Fig. 5.12 signifies rotational motion begins to overpower translation at a lower f_R. Among all the eight cases considered, the C_D signal in Fig. 5.17(a) demonstrates the least fluctuations. Accordingly,

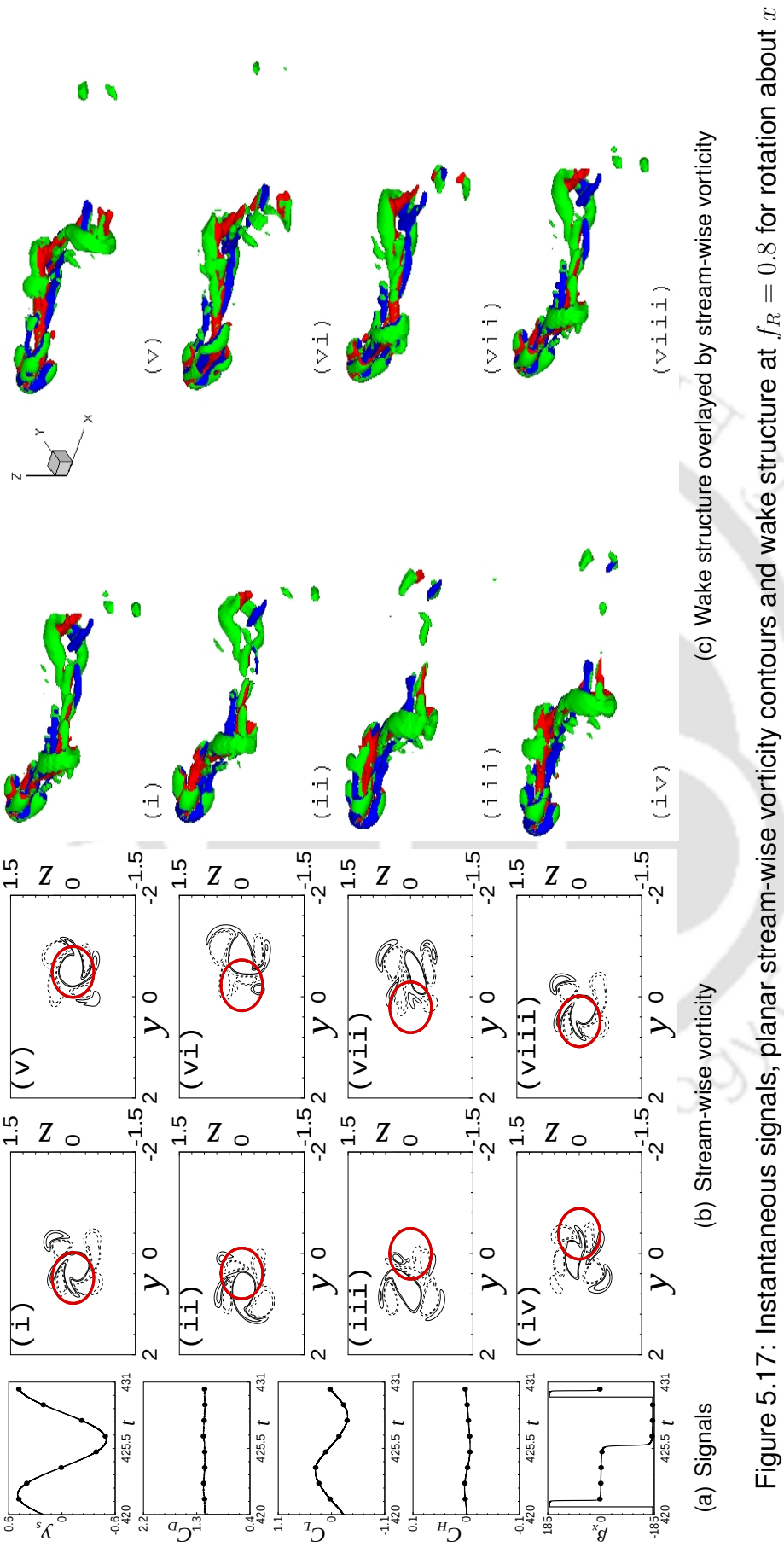

(a) Signals (b) Stream-wise vorticity (c) Wake structure overlayed by stream-wise vorticity

Figure 5.17: Instantaneous signals, planar stream-wise vorticity contours and wake structure at $f_R = 0.8$ for rotation about x

Table 5.1 shows the smallest rms value $C'_D = 9 \times 10^{-3}$. The least fluctuations marked by the smallest rms value imply damping of the unsteady nature in the flow. In other words, the unsteadiness in the flow which is primarily caused by the oscillation of the sphere is suppressed by the simultaneous stream-wise rotation. Pier [27] reported a steady C_D signal for a stream-wise rotating sphere at $Re = 300$ and $\alpha_x = 1.2$. Thus, one can argue that at a smaller oscillating frequency, the oscillating character is replaced by the rotational one.

Symmetric distribution of ω_x contours along $\pm y$ results in $< C_L >= 0$ over a period of y_s and two cycles of C_D again suggest symmetric vortex shedding similar to that at $f_R = 1.3$. A higher fluctuation at $f_R = 1.3$ is seen by comparing the C_L signals in Figs. 5.12 and 5.17. In accordance to higher fluctuations, the contours of ω_x at $f_R = 1.3$ spread to a larger extent than at $f_R = 0.8$.

Vortical structures shown in Fig. 5.17(c) indicate the wake sheds distorted horse shoe loops with two legs on each arm of the shoe. These legs appear due to stream-wise vorticity generated owing to the rotation. Vortex loops are seen to be more elongated than in Fig. 5.12 because of increased vortex formation length at $f_R = 0.8$.

Case II: Transverse (y) rotation

All the cases so far have demonstrated lock-in which is a phenomenon associated with an oscillating structure. For a stream-wise rotating sphere Kim & Choi [26] reported a Frozen regime at $Re = 300$ where ratio of the revolution time of the vortical structure to that of the sphere becomes nearly one. This implies that the vortical structure rotate nearly in phase with the rotating sphere similar to the solid-body rotation. They preferred calling this regime as frozen instead of lock-in (or phase-locked) because lock-in occurs from oscillation having a certain frequency, but this phenomenon is an outcome of steady rotation.

The values of C_L, C_H, β_y signals in Fig. 5.18(a) do not repeat over an oscillation cycle of the sphere. This non-repeating pattern reflects departure from the lock-in condition. Deviation from lock-in is also evident from different topologies

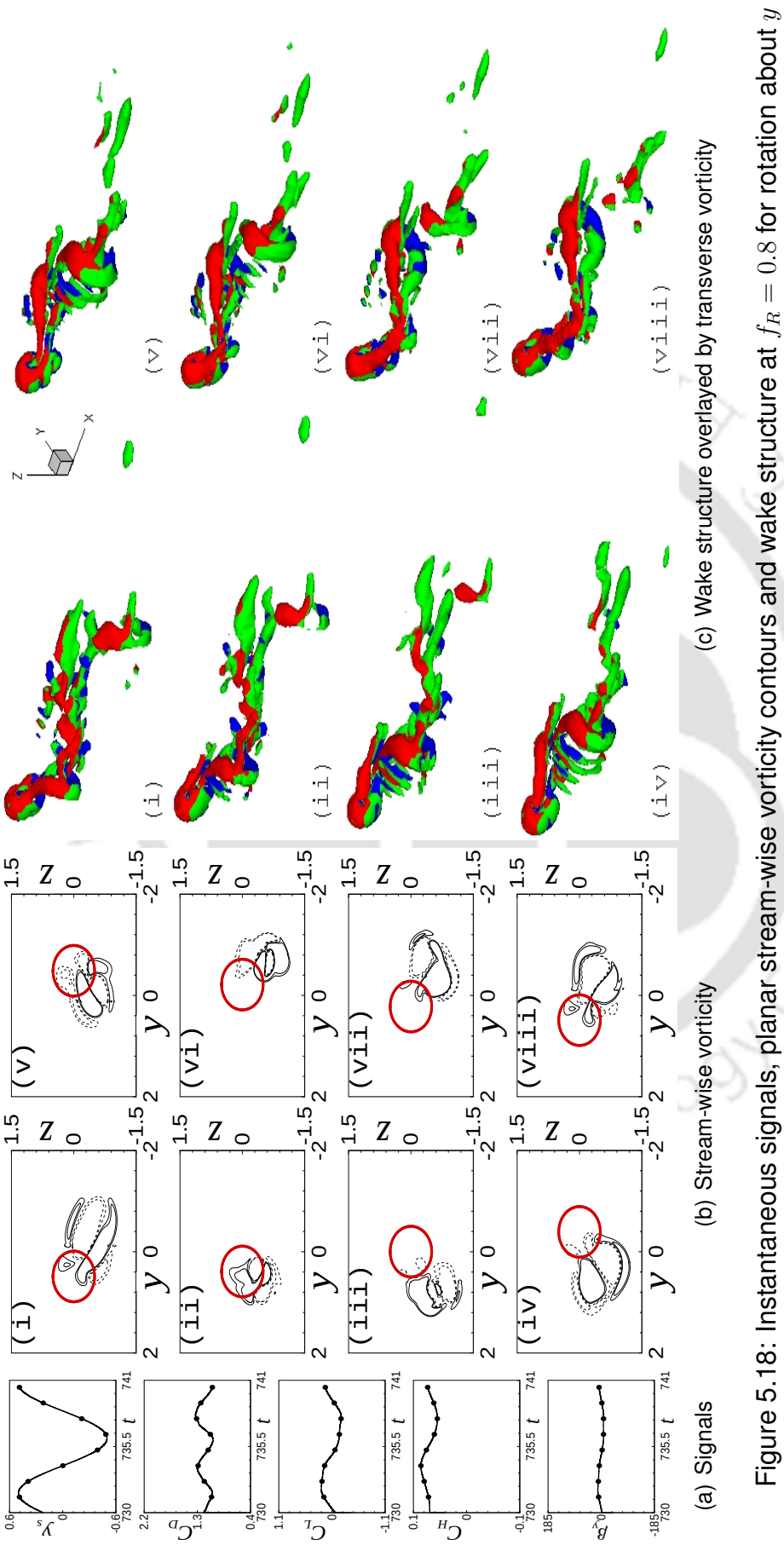

Figure 5.18: Instantaneous signals, planar stream-wise vorticity contours and wake structure at $f_R = 0.8$ for rotation about y

of ω_x and Q structure shown in frames (i) and (viii) of Fig. 5.18(b) and (c).

Among all the orientations of the rotational axis, rotation about y generates maximum vertical force C_H. A large vertical force results in significant departure from the planar-symmetry acquired in case of a purely oscillating sphere in the previous chapter. Table 5.1 shows increase in $< C_H >$ from 0.03 to 0.07 as f_R drops from 1.3 to 0.8. This increase also confirms dominance of rotational effects over transverse oscillation at lower f_R where transverse movement of the wake is small. The ω_x contours in Fig. 5.18(b) are more deflected towards negative z direction than in Fig. 5.13(b). Similarly, the vortical structure in Fig. 5.18(c) shows more rotational tendency than in Fig. 5.13(c). Both these observations further prove the dominance of rotational effects at a lower f_R.

Case III: Vertical (z) rotation

Non repeating behaviour of the flow patterns (ω_x contours and Q) in Fig. 5.19 (b),(c) (i)-(viii) suggests lack of wake synchronization as found for the previous case. Among the three cases, rotation about z generates the maximum (in magnitude) lift force C_L. Table 5.1 shows increase in $< C_L >$ from -0.26 to -0.41 as f_R changes from 1.3 to 0.8. This again confirms the domination of rotational effects at a lower f_R which was also observed for x and y rotations.

The contours and wake display the existence of planar-symmetry at $f_R = 0.8$ for rotation about z as was observed at $f_R = 1.3$. Retaining the planar-symmetry in absence of lock-in is rather surprising as departure from it indicates over powering of the rotational effects while planar-symmetry is an attribute of the oscillating motion.

Case IV: All-axes (xyz) rotation

A higher $< C_L >= -0.52$ is found for this case as rotational effect is largest in this case among all the cases studied. The largest average C_L is in agreement with Poon *et al.* [30] where $< C_L >$ is seen to increase with α and inclination of the rotational axis from the stream-wise direction.

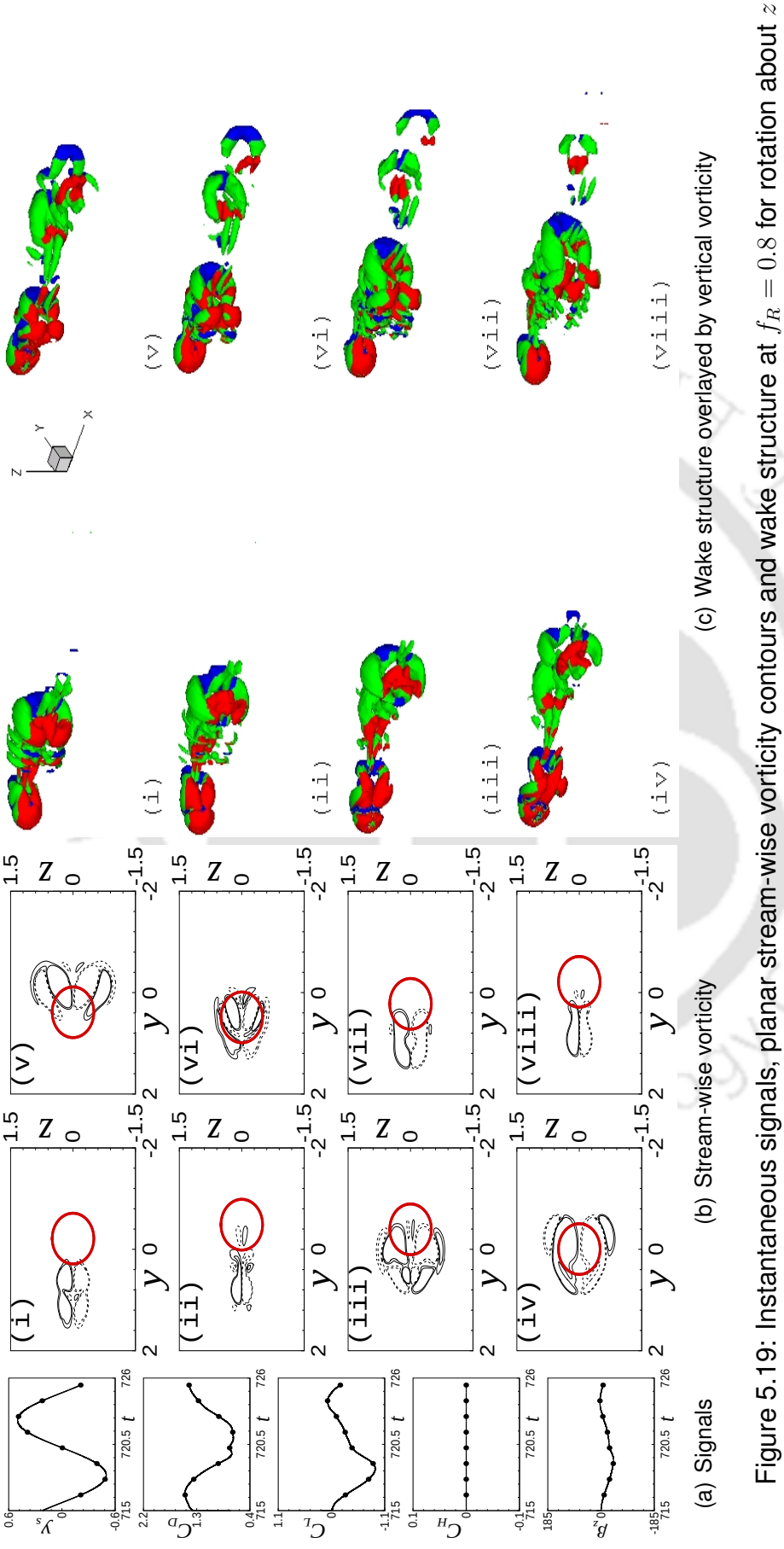

(a) Signals (b) Stream-wise vorticity (c) Wake structure overlayed by vertical vorticity

Figure 5.19: Instantaneous signals, planar stream-wise vorticity contours and wake structure at $f_R = 0.8$ for rotation about z

Figures 5.16(a) and 5.20(a) show attainment of maximum C_D at the seventh and sixth instances, respectively. Corresponding to these two instances the transverse and vertical vorticities convect downstream to distances 7.85, 7.55 and 10.4, 8.6. This observation clearly indicates that the downstream movement of the transverse and vertical vorticities is higher at $f_R = 1.3$.

Solid walls act as a source of vorticity which eventually diffuses within a thin shear layer due to the viscosity of the fluid. The diffused vorticity is convected in the downstream direction by the oncoming uniform flow. As the vorticity convects downstream, the solid wall in reaction to the detachment of vortices experiences a drag force. Higher the rate of detachment greater is the travelling distance of the vortices leading to a greater drag force. This explains the highest $< C_D >= 1.45$ at $f_R = 1.3$.

For a rotating circular cylinder in uniform flow Mittal & Kumar [64] reported an asymmetry in strength and location of positive and negative vortices. Additionally, some of the vorticity generated on the rotating cylinder appeared to be wrapped around it. A similar observation of wrapping of the vorticity was also observed by Dobson *et al.* [32]. Third and sixth instances in Fig. 5.20(a) correspond to a minimum and maximum of C_L, respectively. A closer look at Fig. 5.20(b) reveals that the transverse vorticity contours exhibit wrapping of the positive and negative ω_y at third and sixth instances. This partial covering of the vorticity also occurs on the sphere surface. These two observations further reveal that more positive vorticity in reaction, will exert more negative force on a structure.

Among all the cases the ω_x contours in Fig. 5.21 are seen to shift most towards positive y to mark the most negative $< C_L >$. The vortex chain in comparison to Fig. 5.15 is more thinner and straighter. Mittal & Kumar [64] for a rotating circular cylinder observed the thinning (or narrowing) of the wake at high rotational speeds. The highest rotational effects (due to highest speed and lowest f_R) for this case renders thinning of the wake. Furthermore, the rotational effects become so high that the side-to-side movement of the chain is lost, and the wake

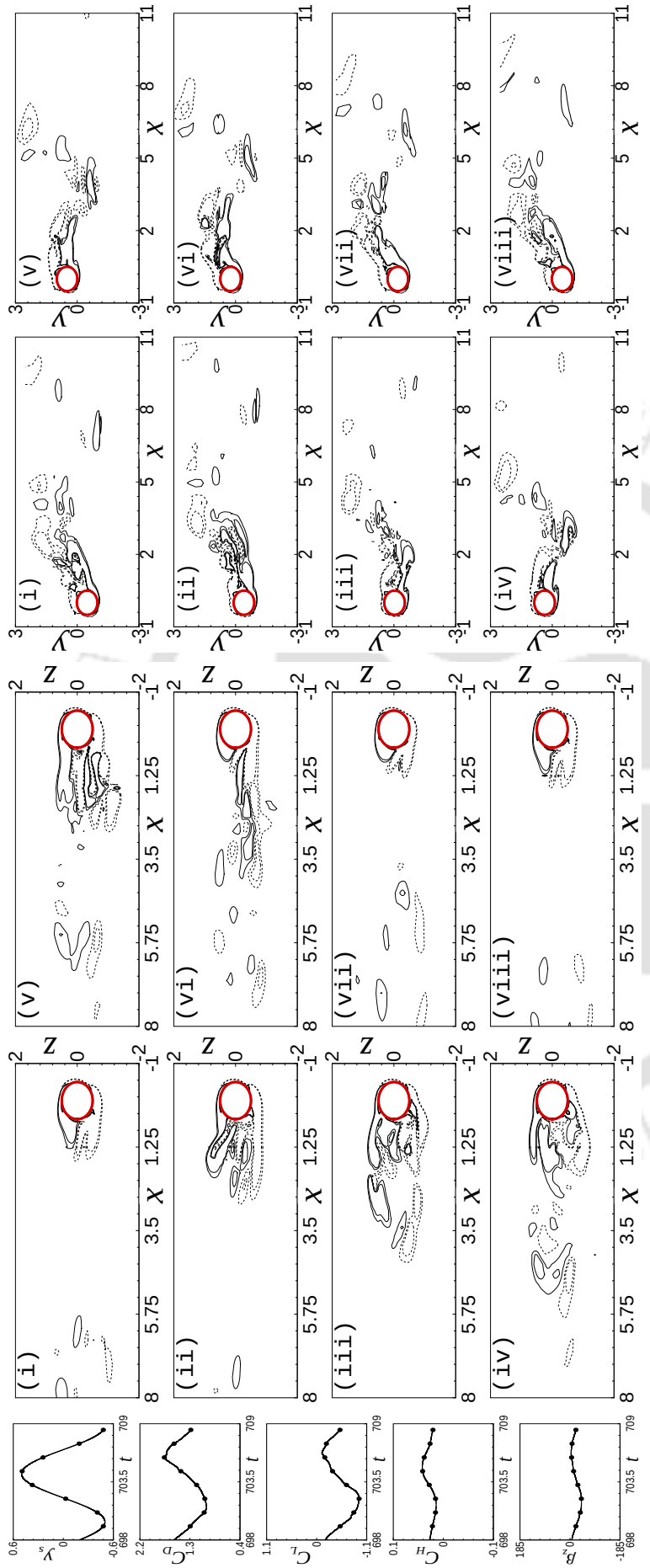

Figure 5.20: Instantaneous signals, transverse and vertical vorticity at $f_R = 0.8$ for rotation about xyz

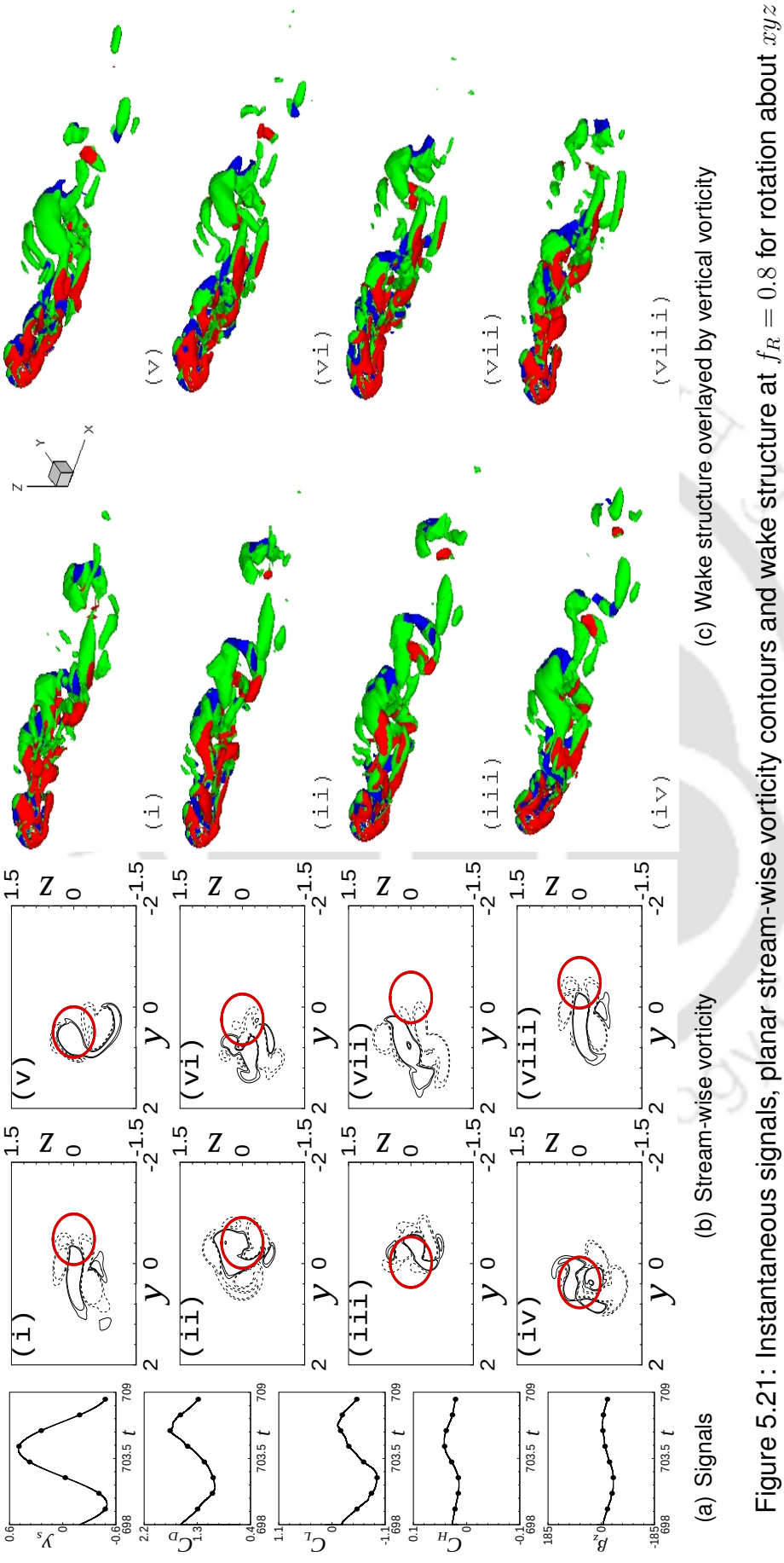

(a) Signals (b) Stream-wise vorticity (c) Wake structure overlayed by vertical vorticity

Figure 5.21: Instantaneous signals, planar stream-wise vorticity contours and wake structure at $f_R = 0.8$ for rotation about xyz

appears to follow a straight path.

5.5 Summary of features in the flow

Based on time evolution of the flow, state of the wake and vortical structures, different flow regimes are identified and they are tabulated in this section.

5.5.1 State of the wake

A complex relation between the lock-in (due to transverse oscillation) and sphere rotation has been found to be the key to categorize the state of the wake. It is observed that at $f_R = 1.3$ lock-in occurs for all the orientations of the rotational axis. Though, the rotational speed is high ($\boldsymbol{\alpha} = 1.2$), a synchronized wake implies that the oscillating character of the flow still prevails. On the other hand, at $f_R = 0.8$, lock-in is only observed for rotation about x axis. This fact clearly indicates that the rotation hinders and even overpowers the oscillation as the sphere loses its transverse inertia. Locked or unlocked state of the wake is represented by L or U, respectively, in the third column in Table 5.2.

5.5.2 Nature of vortex shedding

For a purely oscillating sphere, vortex shedding was found to be symmetric, characterized by zero-mean-lift for locked state. However, as rotational motion is added, vortex shedding for most of the cases is found to be asymmetric. This asymmetric shedding can be attributed to dissimilar strength and location of the attached shear layers created by the rotation of the sphere. At $f_R = 1.3$ with rotation about z the state of the wake is locked, but shedding is seen to be asymmetric which is contrary to what is expected. The fourth column in Table 5.2 summarizes the nature of vortex shedding.

Axis	f_R	State	Shedding	Nature	Rotation	Wake
x	1.3	L	Symmetric	FP	Assisted	HX
	0.8	L	Symmetric	FP	Strongly assisted	HE
y	1.3	L	Symmetric	FP	Strongly opposed	NW
	0.8	U	Weakly asymmetric	CH	Opposed	PR
z	1.3	L	Asymmetric	FP	Weakly assisted	PL
	0.8	U	Strongly asymmetric	QP	Weakly assisted	PL
xyz	1.3	L	Asymmetric	FP	Weakly assisted	TL
	0.8	U	Very strongly asymmetric	CH	Weakly assisted	HN

Table 5.2: Summary of features in the flow

5.5.3 Nature of flow

As the imposed oscillation is sinusoidal, the cases where lock-in is observed the flow is fully-periodic (FP). In asynchronous state, the flow demonstrates two types of time evolution: quasi-periodic (QP) and chaotic (CH). The quasi-periodic nature is assigned if the flow is periodic but with a different periodicity than that of the sphere. At $f_R = 0.8$, the periodicity in the flow for rotation about z is twice the imposed oscillation. However, no specific pattern of time evolution is observed for rotations about y and xyz at $f_R = 0.8$, and the flow is referred to as chaotic. Nature of time evolution of the flow for all the cases is listed in the fifth column of Table 5.2.

5.5.4 Response of the wake to rotation

Response of the wake to the imposed rotation, characterized by the lift angle β, can be an assisting or opposing. Largest and smallest enclosed areas in the $\beta - y_s$ curve are found for rotation about the x and y axis, respectively. This observation suggests that rotation about x assists while that about y opposes (or

resists) the wake's rotation. On the other hand, an intermediate area for rotation about z implies a weak assistance to the rotation of the wake.

5.5.5 Visualization of the wake

For direct comparison of vortical structures, iso-surfaces of Q are plotted in Fig. 5.22 at the instances when C_L is minimum. Structures at $f_R = 0.8$ are more

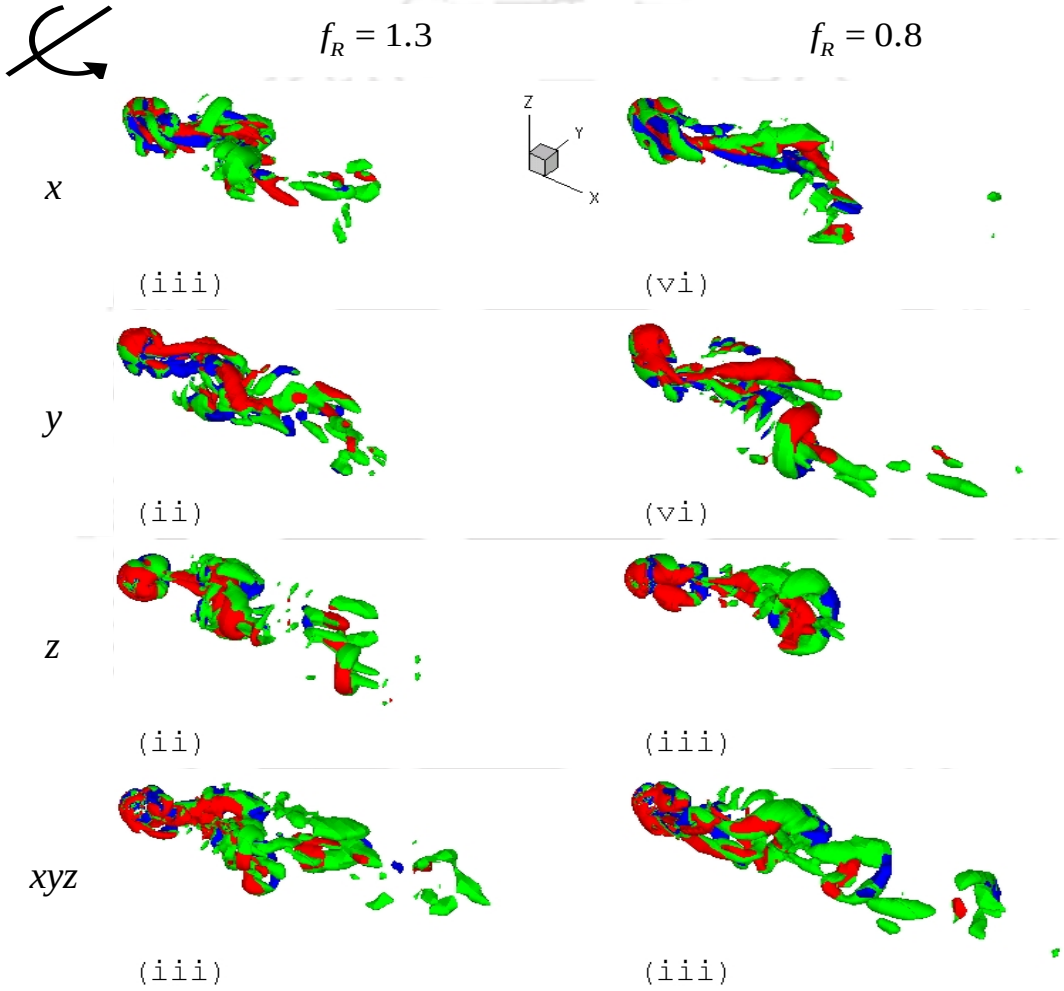

Figure 5.22: Representative wake structure of each flow regime

elongated because of lower vortex shedding frequency than at $f_R = 1.3$ which promotes larger residence time in the near wake. Higher intensity of the anti-clockwise vorticity (shown in red colour) than the clockwise (shown in blue colour) one along the direction of rotation is evident in all the cases. This higher intensity is in agreement with earlier reported studies where the anti-clockwise rotation of

the sphere strengthens and weakens the anti-clockwise and clockwise vorticity, respectively.

For rotation about x the wake resembles a helix (HX) and horseshoe (HE) at $f_R = 1.3$ and 0.8, respectively. However, for rotation about y the wake becomes narrower (NW) at $f_R = 1.3$ and appears as a propeller (PR) at $f_R = 0.8$. As in case of purely oscillating sphere in the previous chapter, the wake displays a planar-symmetry about the horizontal midplane characterized by $< C_H >= C'_H = 0$ which is denoted by PL for rotation about z. Lastly for rotation about all axes, systematic chain like (HN) structures at $f_R = 0.8$ become tangled (TL) at higher frequency ratio ($f_R = 1.3$). Last column in Table 5.2 tabulates shape of the vortical structures.

Chapter 6

Conclusions

This chapter consolidates the contributions made by the present work and their implications in the concerned research field. Also, suggestions for further research are provided accordingly.

Contributions of the work

Principle contributions and findings of the present work can be summarized as

1. Limitations of the previously reported IBM technique [40] has been addressed and removed.

2. Speed-up and efficiency of the developed parallel algorithm is found to deviate from theoretical estimates as communication among processors increases with number of processors.

3. To achieve higher error diminishing rate, BiCGSTAB (Krylov-space based linear solver) is preconditioned by the SIP method which reasonably speed up the calculation.

4. A mechanism of forces is proposed which illuminates the nature and direction of mechanical energy transfer for forced oscillation of a structure.

5. Phase angle (ϕ) between motion (y_s) and transverse force (C_L) is estimated using both analytical and numerical expressions for coefficient of energy (C_E).

6. An insightful correlation between the wake modes for forced and free oscillation of a sphere is put forward.

7. The tendency of the wake to rotate in response to a varying rotational motion of the sphere is explored and documented.

8. The lift force generated on the sphere on account of rotation in addition to the oscillation is opposite to the direction of wake deflection.

9. Different flow features are observed for rotation about y and z axes, though studies on purely rotating sphere treat them as same (transverse axis).

10. The departure from a possible 'lock-in' condition at lower oscillating frequency for a simultaneously oscillating and rotating sphere is explained.

11. In the absence of 'lock-in' the flow is observed as either quasi-periodic or chaotic.

12. The maximum drag force obtained at $f_R = 1.3$ for rotation about all axes (xyz) is associated with the increased downstream movement of the transverse (ω_y) and vertical (ω_z) vorticities.

13. In reaction to detachment of positive vorticities (ω_y and ω_z), negative forces (C_L and C_H) on the sphere are observed.

Answers to the questions raised in the Thesis statement

Based on the accumulated evidences from the present work, the answer to the questions framed in section 1.4.1 are

1. **Questions for the first problem**

   (a) *Can forced transverse oscillation of a sphere in uniform flow predict the VIV modes as in the case of a circular cylinder?*

   The present work was carried out for a range of frequencies ratio ($0.16 \leq f_R \leq 1.3$) at fixed Reynolds number ($Re = 300$) and amplitude ($A =$

0.5). Remarkably, for these parameters three different instabilities similar to the first three periodic VIV modes [68] of a sphere are observed. Occurrence of the VIV modes in forced oscillation suggests that prediction of the former by the later is possible even for a sphere.

(b) *When and why, the coefficient of energy (C_E) is negative?*

To explain the sign of C_E, two forcing mechanisms attributed to the flow (F_F) and external (F_E) agent and measured by C_{vortex} and $C_{potential}$, respectively, are revealed. The sign of C_E is determined by the dominating mechanism out of the two.

(c) *Within the synchronization, what ensures equality between the forcing (f_e) and shedding (f_s) frequencies?*

The vertical vorticity (ω_z) contours have showed that the vortex formation length reduced from $4.5D$ at $f_R = 0.8$ to $4D$ at $f_R = 1.3$. This reduction in length suggests increase in f_s with f_R. In the synchronization band $f_e/f_s = 1$, as $f_R = f_e/f_o$ and f_o remains constant, increase in f_R corresponds to increase in f_e. The increase in f_e and f_s is such that unity ratio is always maintained.

(d) *Within the synchronization for a circular cylinder, two different vortex formation mechanism occur, what happens for a sphere?*

For the oscillating sphere, a chain of vortex loops forms along the sweeping direction. Downstream of the sphere, the two-sided chain merges and vortex rings are formed. Within the synchronization period formation of two vortex rings over an oscillation cycle has been observed.

2. Questions for the second problem

(a) *Can synchronization persist if the oscillating sphere also rotates?*

At $f_R = 1.3$ the wake is in locked state for all the orientations of the rotational axis considered. However, at $f_R = 0.8$ lock-in occurred only for

rotation about the stream-wise (x) axis. These observations suggest that the lock-in state will appear at higher oscillating inertia, but may fail at a lower.

(b) *Is there a symmetry in the flow for a simultaneously oscillating and rotating sphere?*

At $Re = 300$ stream-wise rotation of a sphere [26] disturbs the planar-symmetry present for a stationary sphere. On the other hand, a transversely rotating sphere possesses [29] a planar-symmetry about a plane normal to the axis of rotation. In the present problem, planar-symmetry is absent for all the cases (orientations and frequency ratio) except when the sphere rotates about the vertical (z) axis. Moreover, this observation confirms that rotation does not generate any force component along the axis of rotation.

(c) *Does orientation of the rotational axis change the flow features?*

Literature on a purely rotating sphere have considered rotation about y or z as same and treated them as transverse axis. However, the present work finds different flow features for rotations about y and z. Moreover, in line with the literature, rotation about x manifests features different from y and z axes.

(d) *Will the flow physics alter at a different frequency ratio?*

Under simultaneous oscillation and rotation, a competition between the two has been observed, so the physics is dictated by the dominating motion. The present study finds different flow features for changed oscillating frequency ratio f_R.

Implications of the work

Modifications of the ghost-cell immersed boundary method (GCIBM) in chapter 2 has enhanced its capabilities. Greater values of the hydrodynamic forces for an oscillating sphere (chapter 4) than a stationary one imply that oscillations must

be considered in predicting fluid forces, otherwise they can be catastrophic to the structure. Observation of the VIV modes in forced vibration for a sphere is in line with the finding for a circular cylinder, therefore we can assert that the forced vibration can be employed to predict the free vibration. Figure 6(b) in Govardhan & Williamson [68] shows that $A_y{}^* = 0.5$ which corresponds to a mass-damping parameter $(m^* + C_A)\zeta = 0.181$. Since the present results are consistent with them, we may suggest that the present study is applicable to the VIV of a sphere where such mass-damping parameter prevails.

Different response of the wake to rotate about the three primary axes (x, y and z) suggests that under combined transverse oscillation and rotation (chapter 5), a sphere will first rotate about x then z and lastly y axis. Under dynamic conditions (oscillations of the sphere), rotation about transverse (y) and vertical (z) axes revealed different flow features in chapter 5, so both cannot be considered same as is usually done for a purely rotating sphere.

Strengths

Adoption of GCIBM in an inertial frame of reference suffers from the following difficulties: 1) to maintain an adequate spatial refinement near the solid surface re-meshing is required at every time instant, 2) this re-meshing task puts an extra burden for tagging of the computing cells and associated complexity of communications in parallel environment, 3) spurious force oscillations [44] for moving boundaries are common in IBM simulation. Therefore, incorporation of the non-inertial frame of reference alleviates these difficulties with some limitations.

A non-inertial frame of reference is used for a simultaneously oscillating and rotating sphere, but pseudo forces on account of rotation are not computed, instead velocity on the sphere's surface is imposed. This treatment can be followed for any such problem, provided the angular velocity is kept constant.

The imposition of Neumann boundary condition on the immersed surface, not handled by Gao *et al.* [40], is discussed and demonstrated. It is a well known fact that only such a boundary condition consistently enforces impermeability condi-

tion on the solid surface. Moreover, Gao *et al.* [40] applied GCIBM on uniform grids which is a severe limitation. Present work has extended it on highly non-uniform 3D meshes with parallel implementation.

Limitations

Some of the limitations of the present work are

1. If an object is considered whose surface cannot be expressed as an explicit analytical function, surface triangulation will need to be carried out. This has not been explored in the present work.

2. The domain decomposition method causes the ghost-cells (G) and the immediate fluid neighbours (i.e., the supporting points F) to fall in different processors. This difficult is dealt by restricting the search of F to the processors where G lies. This approach may lead to stall or even blowing up of the computations.

3. As non-inertial frame of reference is chosen, to deal with more than one oscillating geometry selection of the frame will be a great difficulty.

4. Though the present three-dimensional simulations has revealed insightful physics, the study is performed on a narrow parametric range with single value of the oscillation amplitude ($A = 0.5$), Reynolds number ($Re = 300$) and rotational speed ($\boldsymbol{\alpha} = 1.2$).

5. Discarding the pseudo forces due to rotation while constructing the non-inertial frame makes it unable to handle cases with varying angular velocity. This limitation is crucial as practically a structure can undergo rotation with either a pure sinusoidal motion or even time varying angular velocity.

Suggestions for further research

The present GCIBM development can be further improved, especially if its limitations are removed. To overcome the limitations of steady rotation, an oscillating

as well as rotating non-inertial frame is suggested. The non-uniformity in distribution of the ghost-cells among different processors can be effectively handled by communicating the missing information of the neighbouring fluid cells to the host processors, instead of restricting the search. To increase the theoretical accuracy higher order schemes for time integration and spatial discretization can be examined.

The effects of oscillation of the sphere along x and z axes also can be considered. It is important to observe the flow at high Reynolds number and different oscillation amplitudes. Moreover, extensive studies need to be carried out to understand the exact vortex formation mechanisms in the three different modes.

For a simultaneously oscillating and rotating sphere, the obvious extension of the work is to introduce time varying angular velocity. The vortex force (C_{vortex}) helps to recognize different VIV modes for structures when considering only translation motion. In presence of rotational motion, a similar decomposition must be sought to identify new flow features. While attempting such a decomposition, the potential force ($C_{potential}$) must also incorporate the angular force generated due to rotation or a new parameter ($C_{potential}^{Torque}$) may be defined. As for an oscillating structures, computation of coefficient of energy (C_E) for a rotating structure may reveal whether rotation about a particular axis is feasible or not. Again for computing C_E, both work done due to translation and rotation must be considered.

Final remark

This thesis attempts to reveal the physics involved in following two problems: 1) Uniform flow past a transversely oscillating sphere and 2) Uniform flow past a simultaneously oscillating and rotating sphere. Three-dimensional computations have been performed in a parallel environment using Message Passing Interface (MPI). To solve the above problems, a previously reported ghost-cell immersed boundary method is modified. The obtained numerical data is analysed through the time evolutions of 1) fluid forces, 2) three components of vorticity and 3) wake structure. It is believed that the present thesis advances the understanding in

these problems, and will help even a beginner to carry out further research. Therefore, it may be fair to draw the line and leave the above mentioned possibilities for extensions as future assignments.

Appendix

Finite differences for the partial derivatives in non-uniform grid at a point (x_i, y_j, z_k)

First derivatives

$$\frac{\partial \phi_i}{\partial x} = \frac{\phi_{i+1}(\Delta x_{i-1})^2 - \phi_{i-1}(\Delta x_{i+1})^2 - \phi_i\left((\Delta x_{i-1})^2 - (\Delta x_{i+1})^2\right)}{\Delta x_{i+1}\Delta x_{i-1}(\Delta x_{i+1} + \Delta x_{i-1})} + O[(\Delta x)^2]$$
$$\frac{\partial \phi_j}{\partial y} = \frac{\phi_{j+1}(\Delta y_{j-1})^2 - \phi_{j-1}(\Delta y_{j+1})^2 - \phi_j\left((\Delta y_{j-1})^2 - (\Delta y_{j+1})^2\right)}{\Delta y_{j+1}\Delta y_{j-1}(\Delta y_{j+1} + \Delta y_{j-1})} + O[(\Delta y)^2]$$
$$\frac{\partial \phi_k}{\partial z} = \frac{\phi_{k+1}(\Delta z_{k-1})^2 - \phi_{k-1}(\Delta z_{k+1})^2 - \phi_k\left((\Delta z_{k-1})^2 - (\Delta z_{k+1})^2\right)}{\Delta z_{k+1}\Delta z_{k-1}(\Delta z_{k+1} + \Delta z_{k-1})} + O[(\Delta z)^2]$$

Second derivatives

$$\frac{\partial^2 \phi_i}{\partial x^2} = 2\left(\frac{\phi_{i+1}\Delta x_{i-1} + \phi_{i-1}\Delta x_{i+1} - \phi_i(\Delta x_{i+1} + \Delta x_{i-1})}{\Delta x_{i+1}\Delta x_{i-1}(\Delta x_{i+1} + \Delta x_{i-1})}\right) + O[\Delta x]$$
$$\frac{\partial^2 \phi_j}{\partial y^2} = 2\left(\frac{\phi_{j+1}\Delta y_{j-1} + \phi_{j-1}\Delta y_{j+1} - \phi_j(\Delta y_{j+1} + \Delta y_{j-1})}{\Delta y_{j+1}\Delta y_{j-1}(\Delta y_{j+1} + \Delta y_{j-1})}\right) + O[\Delta y]$$
$$\frac{\partial^2 \phi_k}{\partial z^2} = 2\left(\frac{\phi_{k+1}\Delta z_{k-1} + \phi_{k-1}\Delta z_{k+1} - \phi_k(\Delta z_{k+1} + \Delta z_{k-1})}{\Delta z_{k+1}\Delta z_{k-1}(\Delta z_{k+1} + \Delta z_{k-1})}\right) + O[\Delta z]$$

Mixed derivatives

$$\frac{\partial^2 \phi_{i,j}}{\partial x \partial y} = \frac{\phi_{i+1,j+1} - \phi_{i+1,j-1} - \phi_{i-1,j+1} + \phi_{i-1,j-1}}{(\Delta x_{i+1} + \Delta x_{i-1})(\Delta y_{j+1} + \Delta y_{j-1})} + O[\Delta x, \Delta y]$$
$$\frac{\partial^2 \phi_{i,k}}{\partial x \partial z} = \frac{\phi_{i+1,k+1} - \phi_{i+1,k-1} - \phi_{i-1,k+1} + \phi_{i-1,k-1}}{(\Delta x_{i+1} + \Delta x_{i-1})(\Delta z_{k+1} + \Delta z_{k-1})} + O[\Delta x, \Delta z]$$
$$\frac{\partial^2 \phi_{j,k}}{\partial y \partial z} = \frac{\phi_{j+1,k+1} - \phi_{j+1,k-1} - \phi_{j-1,k+1} + \phi_{j-1,k-1}}{(\Delta y_{j+1} + \Delta y_{j-1})(\Delta z_{k+1} + \Delta z_{k-1})} + O[\Delta y, \Delta z]$$

$\Delta x_{i+1} = x_{i+1} - x_i\ ,\quad \Delta x_{i-1} = x_i - x_{i-1}\ ,\quad \Delta y_{j+1} = y_{j+1} - y_j$

$\Delta y_{j-1} = y_j - y_{j-1}\ ,\quad \Delta z_{k+1} = z_{k+1} - z_k\ ,\quad \Delta z_{k-1} = z_k - z_{k-1}$

References

[1] Blevins RD. *Flow-induced vibration*. Van Nostrand Reinhold, New york, 2nd edition, 1990. ISBN 0-69-697269-4.

[2] Sarpkaya T. Vortex-induced oscillations: A selective review. *ASME Journal of Applied Mechanics*, **46**:241–258, 1979.

[3] Sarpkaya T. A critical review of the intrinsic nature of vortex-induced vibrations. *Journal of Fluids and Structures*, **19**:389–447, 2004.

[4] Bearman PW. Vortex shedding from oscillating bluff bodies. *Annual Review of Fluid Mechanics*, **16**:195–222, 1984.

[5] Williamson CHK & Govardhan R. Vortex-induced vibrations. *Annual Review of Fluid Mechanics*, **36**:413–455, 2004.

[6] Feng CC. The measurement of vortex-induced effects in flow past a stationary and oscillating circular and d-section cylinders. *University of British Columbia*, **MASc thesis**:Vancouver, B.C., Canada, 1968.

[7] Khalak A & Williamson CHK. MOTIONS, FORCES AND MODE TRANSITIONS IN VORTEX-INDUCED VIBRATIONS AT LOW MASS-DAMPING. *Journal of Fluids and Structures*, **13**:813–851, 1999.

[8] Blevins RD. Models for Vortex-induced Vibration of Cylinders Based on Measured Forces. *ASME Journal of Fluids Engineering*, **131**:101203–1–101203–9, 2009.

[9] Den Hartog JP. The vibration problems in engineering. *Proc 4th Int Congr Appl Mech, Cambridge, England*, :pp. 34–53, 1934.

[10] Bishop RED & Hassan AY. The lift and drag forces on a circular cylinder oscillating in a flowing fluid. *Proceedings of the Royal Society of London A*, **277**:51–75, 1964.

[11] Zdravkovich MM. Modification of vortex shedding in the synchronization range. *ASME Journal of Fluids Engineering*, **104**:513–517, 1982.

[12] Williamson CHK & Roshko A. Vortex formation in the wake of an oscillating cylinder. *Journal of Fluids and Structures*, **2**:355–381, 1988.

[13] Meier-Windhorst A. Flatterschwingungen von Zylindern in gleichmassigen Flussigkeitsstrom (Flutter Oscillations of Cylinder in Uniform liquid Flow). *Mitteillungen des Hydraulischen Instituts der Technischen Hochschule*, **Munchen, Heft 9**:3–39, 1939.

[14] Morse TL & Williamson CHK. Employing controlled vibrations to predict fluid forces on a cylinder undergoing vortex-induced vibration. *Journal of Fluids and Structures*, **22**:877–884, 2006.

[15] Morse TL & Williamson CHK. Prediction of vortex-induced vibration response by employing controlled motion. *Journal of Fluid Mechanics*, **634**: 5–39, 2009.

[16] Morse TL & Williamson CHK. Steady, unsteady and transient vortex-induced vibration predicted using controlled motion data. *Journal of Fluid Mechanics*, **649**:429–451, 2010.

[17] Govardhan R. & Williamson C. H. K. Modes of vortex formation and frequency response of a freely vibrating cylinder. *Journal of Fluid Mechanics*, **420**:85–130, 2000.

[18] Johnson TA & Patel VC. Flow past a sphere up to a Reynolds number of 300. *Journal of Fluid Mechanics*, **378**:19–70, 1999.

[19] Mittal R. Planar Symmetry in the Unsteady Wake of a Sphere. *AIAA Journal*, **37**:388–390, 1999.

[20] Mittal R. A fourier-chebsyshev spectral collocation method for simulating flow past spheres and spheroids. *INTERNATIONAL JOURNAL FOR NUMERICAL METHODS IN FLUIDS*, **30**:921–937, 1999.

[21] Tomboulides AG & Orszag SA. Numerical investigation of transitional and weak turbulent flow past a sphere. *Journal of Fluid Mechanics*, **416**:45–73, 2000.

[22] Thompson MC, Leweke T, & Provansal M. Kinematics and dynamics of sphere wake transition. *Journal of Fluids and Structures*, **15**:575–585, 2001.

[23] Behara S, Borazjani I, & Sotiropoulos F. Vortex-induced vibrations of an elastically mounted sphere with three degrees of freedom at Re=300: hysteresis and vortex shedding modes. *Journal of Fluid Mechanics*, **686**:426–450, 2011.

[24] Lee H, Hourigan K, & Thompson MC. Vortex-induced vibration of a neutrally buoyant tethered sphere. *Journal of Fluid Mechanics*, **719**:97–128, 2013.

[25] Peter S & De AK. Wake instability modes for forced transverse oscillation of a sphere. *Ocean Engineering*, **115**:48–59, 2016.

[26] Kim D & Choi H. Laminar flow past a sphere rotating in the streamwise direction. *Journal of Fluids Mechanics*, **461**:365–386, 2002.

[27] Pier B. Periodic and qasiperiodic vortex shedding in the wake of a rotating sphere. *Journal of Fluids and Structures*, **41**:43–50, 2013.

[28] Giacobello M, Ooi A, & Balachandar S. Wake structure of a transversely rotating sphere at moderate Reynolds numbers. *Journal of Fluids Mechanics*, **621**:103–130, 2009.

[29] Kim D. Laminar flow past a sphere rotating in the transverse direction. *Journal of Mechanical Science and Technology*, **23**:578–589, 2009.

[30] Poon E, Ooi A, Giacobello M, & Cohen CZ Raymond. Laminar flow structures from a rotating sphere: Effect of rotating axis angle. *International Journal of Heat and Fluid Flow*, **31**:961–972, 2010.

[31] Poon E, Ooi A, Giacobello M, & Cohen CZ Raymond. Hydrodynamic forces on a rotating sphere. *International Journal of Heat and Fluid Flow*, **42**:278–288, 2013.

[32] Dobson J, Ooi A, & Poon E. The flow structures of a transversely rotating sphere at high rotation rates. *Computers & Fluids*, **102**:170–181, 2014.

[33] Poon E, Ooi A, Giacobello M, Iaccarino G, & Chung D. Flow past a transversely rotating sphere at Reynolds numbers above the laminar regime. *Journal of Fluids Mechanics*, **759**:751–781, 2014.

[34] Peskin CS. Flow patterns around heart valves:a numerical method. *Journal of Computational Physics*, **10**:252–271, 1972.

[35] Goldstein D, Handler R, & Sirovich L. Modelling a no-slip flow boundary with an external force field. *Journal of Computational Physics*, **105**:354–366, 1993.

[36] Mohd-Yosuf J. Combined immersed-boundary/b-spline methods for simulations of flow in complex geometries. *Center for Turbulence Research, Annual Research Briefs*, :317–327, 1997.

[37] Kim J, Kim D, & Choi H. An immersed-boundary finite-volume method for simulations of flow in complex geometries. *Journal of Computational Physics*, **171**:132–150, 2001.

[38] Majumdar S, Iaccarino G, & Durbin P. Rans solvers with adaptive structured boundary non-conforming grids. *Center for Turbulence Research, Annual Research Briefs*, :353–366, 2001.

[39] Iaccarino G & Verzicco R. Immersed boundary technique for turbulent flow simulations. *ASME Applied Mechanics Reviews*, **56**:331–347, 2003.

[40] Gao T, Tseng YH, & Lu XY. An improved hybrid Cartesian/immersed boundary method for fluid-solid flows. *INTERNATIONAL JOURNAL FOR NUMERICAL METHODS IN FLUIDS*, **55**:1189–1211, 2007.

[41] Tseng YH & Ferziger JH. A ghost-cell immersed boundary method for flow in complex geometry. *Journal of Computational Physics*, **192**:593–623, 2003.

[42] Mittal R, Dong H, Bozkurttas M, Najjar FM, Vargas A, & Loebbecke AV. A versatile sharp interface immersed boundary method for incompressible flows with complex boundaries. *Journal of Computational Physics*, **227**:4825–4852, 2008.

[43] De AK. An implicit non-staggered cartesian grid method for incompressible viscous flows in complex geometries. *Sadhana, Indian Academy of Sciences*, **39**:1071–1094, 2014.

[44] Lee J & You D. An implicit ghost-cell immersed boundary method for simulations of moving body problems with control of spurious force oscillations. *Journal of Computational Physics*, **233**:295–314, 2013.

[45] Peter S & De AK. A parallel implementation of the ghost-cell immersed boundary method with application to stationary and moving boundary problems. *Sadhana, Indian Academy of Sciences*, **41**:441–450, 2016.

[46] Kim D & Choi H. Immersed boundary method for flow around an arbitrarily moving body. *Journal of Computational Physics*, **212**:662–680, 2006.

[47] Mittal R & Iaccarino G. Immersed boundary methods. *Annual Review of Fluid Mechanics*, **37**:239–261, 2005.

[48] Williamson CHK & Govardhan R. Dynamics and forcing of a tethered sphere in a fluid flow. *Journal of Fluids and Structures*, **11**:293–305, 1997.

[49] Nobari MRH & Ghazanfarian J. A numerical investigation of fluid flow over a rotating cylinder with cross flow oscillation. *Computers & Fluids*, **38**:2026–2036, 2009.

[50] Nazarinia M, Jacono DL, Thompson MC, & Sheridan J. Flow behind a cylinder forced by a combination of oscillatory translational and rotational motions. *PHYSICS OF FLUIDS*, **21**:051701(1–4), 2009.

[51] Nazarinia M, Jacono DL, Thompson MC, & Sheridan J. Flow over a cylinder subjected to combined translational and rotational oscillations. *Journal of Fluids and Structures*, **32**:135–145, 2012.

[52] Bourguet R & Jacono DL. Flow-induced vibrations of a rotating cylinder. *Journal of Fluids Mechanics*, **740**:342–380, 2014.

[53] Pope SB. *Turbulent Flows*. Cambridge University Press. Cambridge, 2000.

[54] De AK & Dalal A. Numerical simulation of unconfined flow past a triangular cylinder. *INTERNATIONAL JOURNAL FOR NUMERICAL METHODS IN FLUIDS*, **52**:801–821, 2006.

[55] Rhie CM & Chow WL. Numerical Study of the Turbulent Flow Past an Airfoil with Trailing Edge Separation. *AIAA JOURNAL*, **21**:1525–1532, 1983.

[56] Stone HL. Iterative solution of implicit approximation of multidimensional partial differential equations. *SIAM Journal on Numerical Analysis*, **5**:530–558, 1968.

[57] Zhang Shao-Liang. Gpbi-cg: Generalized product-type methods based on bi-cg for solving nonsymmetric linear systems. *SIAM J. Sci. Comput.*, **18**(2): 537–551, 1997.

[58] Hunt JCR, Wray AA, & Moin P. Eddies, streams, and convergence zones in turbulent flows. *Center for Turbulence Research Report CTR-S88*, **2**: 193–208, 1988.

[59] Koopmann GH. The vortex wakes of vibrating cylinders at low reynolds number. *Journal of Fluid Mechanics*, **23**:501–512, 1967.

[60] Guilmineau E & Queutey P. A numerical simulation of vortex shedding from an oscillating circular cylinder. *Journal of Fluids and Structures*, **16**:773–794, 2002.

[61] Zhou CH & Shu C. A local domain-free discretization method for simulation of incompressible flows over moving bodies. *INTERNATIONAL JOURNAL FOR NUMERICAL METHODS IN FLUIDS*, **66**:162–182, 2011.

[62] Kang S, Choi H, & Lee S. Laminar flow past a rotating circular cylinder. *PHYSICS OF FLUIDS*, **11**:3312–3321, 1999.

[63] Stojkovic D, Breuer M, & Durst F. Effect of high rotation rates on the laminar flow around a circular cylinder. *PHYSICS OF FLUIDS*, **14**:3160–3178, 2002.

[64] Mittal S & Kumar B. Flow past a rotating cylinder. *Journal of Fluid Mechanics*, **476**:303–334, 2003.

[65] Kumar S, Cantu C, & Gonzalez B. Flow past a rotating cylinder at low and high rotation rates. *ASME Journal of Fluids Engineering*, **133**:041201–1–041201–9, 2011.

[66] Govardhan R & Williamson CHK. Vortex-induced motions of a tethered sphere. *Journal of Wind Engineering and Industrial Aerodynamics*, **69-71**: 375–385, 1997.

[67] Jauvtis N, Govardhan R, & Williamson CHK. Multiple modes of vortex-induced vibration of a sphere. *Journal of Fluids and Structures*, **15**:555–563, 2001.

[68] Govardhan R & Williamson CHK. Vortex-induced vibrations of a sphere. *Journal of Fluid Mechanics*, **531**:11–47, 2005.

[69] Hout RV, Krakovich A, & Gottlieb O. Time resolved measurements of vortex-induced vibrations of a tethered sphere in uniform flow. *PHYSICS OF FLUIDS*, **22**:087101(1–11), 2010.

[70] Eshbal L, Krakovich A, & Hout RV. Time resolved measurements of vortex-induced vibrations of a positively buoyant tethered sphere in uniform water flow. *Journal of Fluids and Structures*, **35**:185–199, 2012.

[71] Carberry J, Sheridan J, & Rockwell D. Controlled oscillations of a cylinder: forces and wake modes. *Journal of Fluid Mechanics*, **538**:31–69, 2005.

[72] Leontini JS, Stewart BE, Thompson MC, & Hourigan K. Wake state and energy transitions of an oscillating cylinders at low Reynolds number. *PHYSICS OF FLUIDS*, **18**:067101(1–9), 2006.

[73] Baranyi L & Daroczy L. Mechanical energy transfer and flow parameter effects for a cylinder in transverse oscillation. *International Journal of Heat and Fluid Flow*, **43**:251–258, 2013.

[74] Garstang TE. The Flow of Viscous Liquid Past Spinning Bodies. *Proceedings of the Royal Society of London A*, **142**:491–508, 1933.

[75] Torobin LB & Gauvin WH. Fundamental Aspects of Solids-Gas Flow: Part IV: The Effects of Particle Rotation, Roughness and Shape. *The Candian Journal of Chemical Engineering*, **38**:142–153, 1960.

[76] Barkla HM & Auchterlonie LJ. The Magnus or Robins effect on rotating spheres. *Journal of Fluids Mechanics*, **47**:437–447, 1971.

[77] Schlitchting H. *Boundary Layer Theory*. McGraw-Hill, 1979.

[78] Skarysz M, Prysko J, Goujon-Durand S, & Wesfreid JE. The wake behind a rotating sphere. *Journal of Physics*, **530**:1–7, 2014.

[79] Taneda S. Visual observations of the flow past a sphere at reynolds numbers between 10^4 and 10^6. *Journal of Fluids Mechanics*, **85**:187–192, 1978.

[80] Jindal S, Long LN, Plassmann PE, & Uzol NS. Large eddy simulations around a sphere using unstructured grids. *AIAA fluid dynamics Conference and exhibit, Portland, Oregon*, **AIAA-2004-2228**:1–16, 2004.

Publications and conferences

Publications

1. Peter S & De AK. A parallel implementation of the ghost-cell immersed boundary method with application to stationary and moving boundary problems. *Sadhana, Indian Academy of Sciences*, **41**:441-450, 2016.

2. Peter S & De AK. Wake instability modes for forced transverse oscillation of a sphere. *Ocean Engineering*, **115**:48-59, 2016.

3. Peter S & De AK. Energy transfer and associated forces in fluid-structure interactions. *Procedia Engineering*, **144**:1220-1225, 2016.

4. Peter S & De AK. Wake of a simultaneously oscillating and rotating sphere in uniform flow. (***under preparation***).

Conferences

1. Peter S & De AK. A parallelized collocated immersed boundary method. 4^{th} *International Congress on Computational Mechanics and Simulation*. IIT Hyderabad, India, 2012.

2. Peter S & De AK. Energy transfer and associated forces in fluid-structure interactions. 12^{th} *International Conference on Vibration Problems*. IIT Guwahati, India, 2015.

3. Peter S & De AK. Wake Behind a Rotating Sphere Oscillating in Uniform Flow. (***To appear***) *Proceedings of the* 6^{th} *International and* 43^{rd} *National Conference on Fluid Mechanics and Fluid Power*. MNNIT A, Allahabad, U.P., India, 2016.